Measurement and Characterization of Heat and Mass Diffusion in PEMFC Porous Media

by

Grant Unsworth

A thesis
presented to the University of Waterloo
in fulfillment of the
thesis requirement for the degree of
Master of Applied Science
in
Mechanical Engineering

Waterloo, Ontario, Canada, 2012

I hereby declare that I am the sole author of this thesis. This is a true copy of the thesis, including any required final revisions, as accepted by my examiners.

I understand that my thesis may be made electronically available to the public.

Grant Unsworth

Abstract

A single polymer electrolyte membrane fuel cell (PEMFC) is comprised of several sub-millimetre thick layers of varying porosity sandwiched together. The thickness of each layer, which typically ranges from 10 to $200\mu m$, is kept small in order to minimize the transport resistance of heat, mass, electrons, and protons, that limit reaction rate. However, the thickness of these materials presents a significant challenge to engineers characterizing the transport properties through them, which is of considerable importance to the development and optimization of fuel cells. The objective of this research is to address the challenges associated with measuring the heat conduction and gas diffusion transport properties of thin porous media used in PEMFCs. An improvement in the accuracy of the guarded heat flow technique for measuring thermal conductivity and the modified Loschmidt Cell technique for measuring gas diffusivity are presented for porous media with a sub-millimetre thickness. The marketable improvement in accuracy is achieved by analysing parameters in each apparatus that are sensitive to measurement error and have the largest contribution to measurement uncertainty, and then developing ways to minimize the error. The experimental apparatuses are used to investigate the transport properties of the gas diffusion layer (GDL) and the microporous layer (MPL), while the methods would also be useful in the study of the catalyst layer (CL).

Gas diffusion through porous media is critical for the high current density operation of a PEMFC, where the electrochemical reaction becomes rate-limited by the diffusive flux of reactants reaching reaction sites. However, geometric models that predict diffusivity of the GDL have been identified as inaccurate in current literature. Experimental results give a better estimate of diffusivity, but published works to date have been limited by high measurement uncertainty. In this thesis, the effective diffusivity of various GDLs are measured using a modified Loschmidt cell and the relative differences between GDLs are explained using scanning electron microscopy and the method of standard porosimetry. The experimental results from this study and others in current literature are used to develop a generalized correlation for predicting diffusivity as a function of porosity in the through-plane direction of a GDL.

The thermal conductivity and contact resistance of porous media are important for

accurate thermal analysis of a fuel cell, especially at high current densities where the heat flux becomes large. In this thesis, the effective through-plane thermal conductivity and contact resistance of the GDL and MPL are measured. GDL samples with and without a MPL and coated with 30%-wt. PTFE are measured using the guarded steady-state heat flow technique described in the ASTM standard E 1225-04. Thermal contact resistance of the MPL with the iron clamping surface was found to be negligible, owing to the high surface contact area. Thermal conductivity and thickness of the MPL remained constant for compression pressures up to $15 bar$ at $0.30 W/m^\circ K$ and $55 \mu m$, respectively. The thermal conductivity of the GDL substrate containing $30\% -$wt. PTFE varied from 0.30 to $0.56 W/m^\circ K$ as compression was increased from 4 to $15 bar$. As a result, the GDL containing MPL had a lower effective thermal conductivity at high compression than the GDL without MPL. At low compression, differences were negligible. The constant thickness of the MPL suggests that the porosity, as well as heat and mass transport properties, remain independent of the inhomogeneous compression by the bipolar plate. Despite the low effective thermal conductivity of the MPL, thermal performance of the GDL can be improved by exploiting the excellent surface contact resistance of the MPL while minimizing its thickness.

Acknowledgements

Dedication

Dedicated to my wife, without whose love and encouragement
this thesis would have been finished a lot sooner ;).

Table of Contents

List of Tables

List of Figures

Nomenclature

α Thermal Diffusivity (mm^2/s)

ΔH° Change in enthalpy (kJ)

ϵ Porosity

κ Lifetime (μsec)

λ_g Geometric Factor

∇ Difference

ϕ Phase Shift (rad)

ψ Capillary Potential (J)

ρ Density (kg/m^3)

σ Molecular Diameter (nm)

τ Tortuosity

θ Wetting Angle (rad)

$\vec{r}$ Position Vector (m)

A Area (mm^2)

b_i Klinkenberg Coefficient

C_i Concentration $(\% - mol)$

C_p Specific Heat Capacity $(J/kg°K)$

$D_{ij,\mathrm{K}}$ Knudsen Diffusion Coefficient (cm^2/s)

D_{ij} Gas Diffusion Coefficient (cm^2/s)

D_{ij}^{binary} Binary Gas Diffusion Coefficient (cm^2/s)

D_{ij}^{eff} Effective Gas Diffusion Coefficient (cm^2/s)

D_{ij}^{eq} Equivilant Gas Diffusion Coefficient (cm^2/s)

f Frequency (Hz)

$f(\epsilon, \tau)$ Diffusibility

$F(r)$ Pore Size Distribution (cm^3/g)

Fo Fourier Number

k Thermal Conductivity $(W/m°K)$

k_b Boltzmann Constant (m^2kg/s^2K)

k_g Gas Permeability (cm^2)

Kn Knudsen Number

L Characteristic Length (mm)

l Sample Thickness (μm)

p Pressure (kPa)

Q Heat Flow Rate (W)

R Thermal Resistance $(°K/W)$

R_c Thermal Contact Resistance $(°K/W)$

T Temperature $(°K)$

t Time (s)

V Volume (mm^3)

V_v Pore Volume (cm^3)

V_cell Cell potential (V)

x Position (mm)

x_p Probe Distance (mm)

$\Delta G_\mathrm{f}°$ Gibbs free energy (kJ)

Chapter 1

Introduction

For Western nations, three primary issues surround the use of crude oil to power automobiles: environmental impact, energy security, and the risk of demand outstripping supply. The Polymer Electrolyte Membrane Fuel Cell (PEMFC) and various battery technologies have emerged as commercially viable alternatives to the internal combustion engine that could dramatically reduce the dependence of crude oil on Western societies. These technologies act as energy carriers that enable domestically produced electricity to be stored on board a vehicle.

After several decades of development, most notably by Ballard Power Systems, the commercial viability of PEMFC powered vehicles has been established. Companies such as Daimler, Ford, General Motors, Honda, Hyundai, Nissan, and Toyota have publicly committed to selling a fuel cell vehicle by the year 2015 [5]. In 2011, Mercedes-Benz drove a fleet of fuel cell powered cars around the world (33,000 km) to demonstrate their commercial readiness [6]. Their B-class based fuel cell vehicle, called the F-cell, has a 380 km range, 11.4 second 0-60 km/hr acceleration, and comparable handling to the equivalent gasoline powered model. The F-cell's fuel cell durability has been demonstrated beyond 2500 hours of real world operation with less than 10% degradation in performance.

The current state of fuel cell technology is suitable for attracting early adopters looking to experience the latest technology. For example, Honda leases the FCX Clarity fuel cell vehicle to a select number of people in Japan, Europe, and California each year [7].

However, mass adoption will only occur once the technology has matured to be competitive with the internal combustion engine, and it is this benchmark that drives current research in the field.

1.1 PEMFC Working Principle

A fuel cell is an electrochemical device that converts chemical energy into electrical energy. Similar in principle to a battery, a fuel cell differs by storing its reactants externally to the cell rather than internally. This enables continuous operation of the cell as long as a supply of fuel and oxidant is available. The PEMFC is characterized by its ion transport medium, a solid polymer electrolyte. A solid electrolyte offers a number of advantages over fuel cells with liquid electrolytes, including a simple and compact cell structure that is easy to manufacture and insensitive to orientation. PEMFCs operate at low temperatures (usually less than $100\,^{\circ}$C), which enables a quick start-up time and makes them ideally suited for transportation applications.

Figure 1.1 presents a cross-sectional schematic of the primary components in a PEMFC. Hydrogen gas is delivered to the anode, passes through the gas diffusion layer, and is catalytically split into protons and electrons by the oxidation half cell reaction,

$$H_2 \rightarrow 2H^+ + 2e^- \tag{1.1}$$

The protons pass through the proton-conducting polymer electrolyte membrane, the characteristic feature of a PEMFC, to reach the cathode catalyst layer. An externally connected electrical load provides a path for the electrons to flow. At the cathode, atmospheric air is introduced into the cell and diffuses through the gas diffusion layer to reach the cathode catalyst layer. In the presence of a catalyst, oxygen in the air undergoes a reduction half cell reaction with the hydrogen ions to form water, such that,

$$\frac{1}{2}O_2 + 2H^+ + 2e^- \rightarrow H_2O_{(l)} \tag{1.2}$$

where the operating temperature of most PEMFCs is below the boiling point of water. This results in the formation of liquid water, rather than vapour, which presents a major challenge for removal from the cell [8–11]. Waste heat is produced as a result of irreversibilities in converting chemical energy into electrical energy. The overall reaction is therefore,

$$H_2 + \frac{1}{2}O_2 \rightarrow H_2O + \text{waste heat} + \text{electrical energy} \qquad (1.3)$$
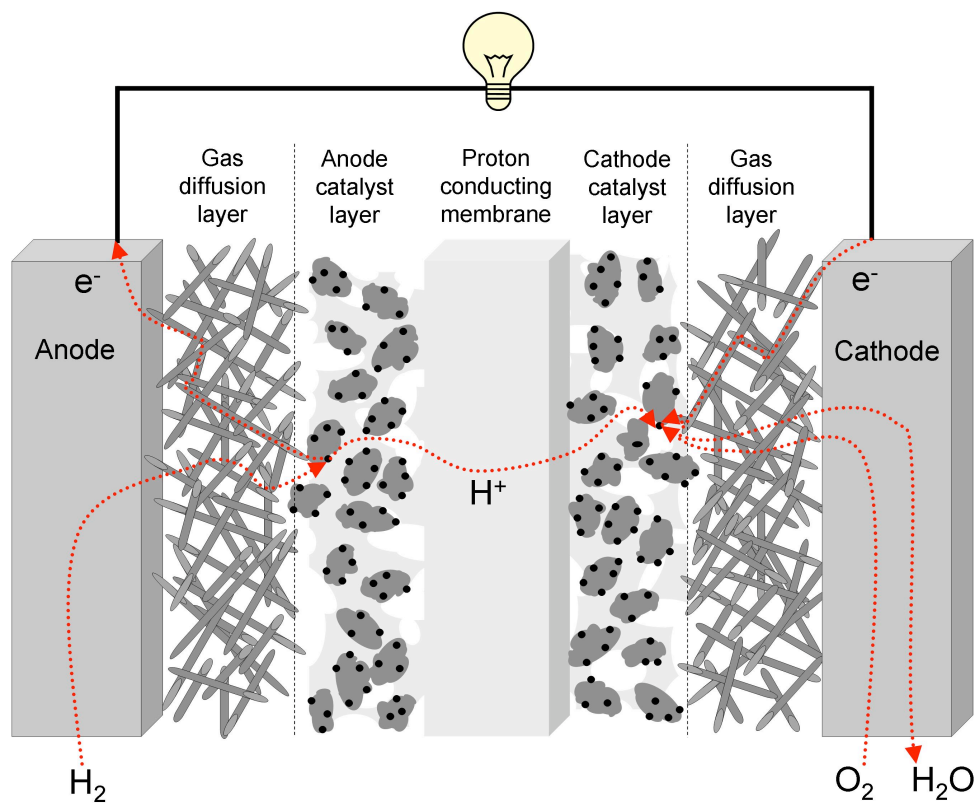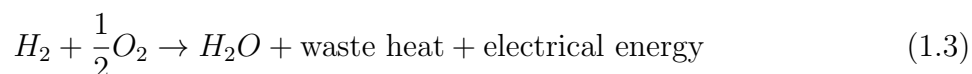
Figure 1.1: Cross sectional schematic of a polymer electrolyte membrane fuel cell [1].

The enthalpy change for the chemical reaction of hydrogen, the enthalpy of reaction,

provides a measure of energy input to the fuel cell. The electrical energy produced during the reaction represents the useful energy output. The waste heat produced in Eq. (1.3) is of low quality and not considered useful energy. Then, at standard conditions the thermodynamic fuel cell efficiency, η, is the ratio of the change in Gibbs free energy ($\Delta G_{\mathrm{f}}°$) to the change in enthalpy ($\Delta H°$), using the higher heating value (HHV) of hydrogen,

$$\eta = \frac{\Delta G_{\mathrm{f}}°}{\Delta H°} = \frac{237.1[kJ/mol]}{286.0[kJ/mol]} = 83\% \tag{1.4}$$

However, a fuel cell will never achieve the thermodynamic efficiency in Eq. (1.4), similar to the Carnot efficiency of a heat engine. The cell efficiency is the cell potential voltage, V_{cell}, divided by the thermodynamic potential voltage based on the HHV of hydrogen, or,

$$\text{Cell Efficiency} = \frac{V_{\mathrm{cell}}}{1.48} \text{ x } 100\% \tag{1.5}$$

1.2 PEMFC Performance

Neither the overall reaction described in Eq. (1.3) or the cell efficiency found in Eq. (1.5) can determine the actual electrical energy that can be extracted from an operating PEMFC. The study of electrochemical kinetics provides the missing information about how fast a reaction occurs, the actual reaction pathway, and energy losses for a specific cell configuration [12]. It is electrochemical kinetics that allows the influence of each component's design to be assessed in terms of actual fuel cell performance.

A polarization curve is commonly used to describe fuel cell performance. The shape of the curve, influenced by the electrochemical kinetics, relates cell voltage as a function of current density. Three primary regions of overpotential losses shown in Figure 1.2 help to characterize the curve, including activation polarization, ohmic polarization, and concentration polarization.

Activation polarization is caused by the slow rate of the electrochemical reactions and is dominant at low current density operation. In PEMFCs, a platinum catalyst is used to
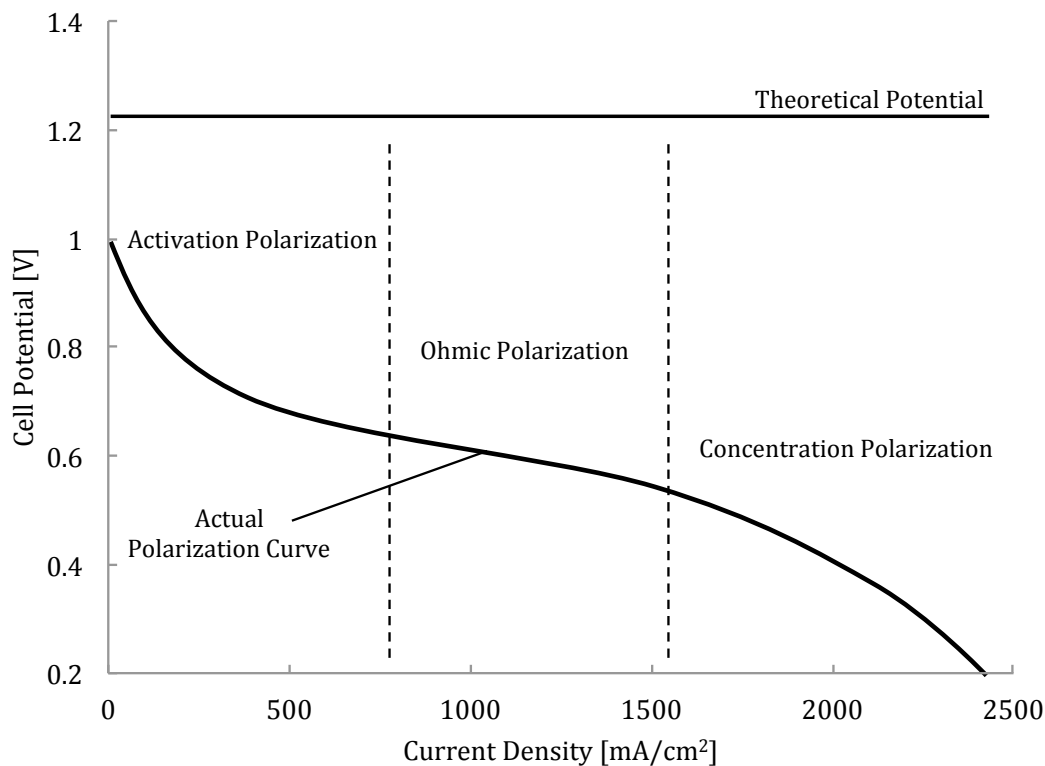
Figure 1.2: A polarization curve illustrating the actual cell potential-current relationship, which differs from the theoretical potential due to overpotential losses [2].

speed up reaction rate and minimize this resistance. However, operating a fuel cell in this region is not practical since power density, which is proportional to current density, is very low. Ohmic polarization arises from electrical resistance in the transfer of both ions in the electrolyte and electrons in the rest of cell components. At high current density operation, the rate of mass transfer of the reactants and products becomes reaction rate limiting and classified as concentration polarization. Liquid water produced by the reaction can further impede reactants from reaching reaction sites by flooding pores and reducing the effective area for mass transfer to occur.

Hydrogen gas fed to the anode of a PEMFC contains no inert gas species and no gaseous

byproducts of the half cell reaction are produced, as shown in Eq (1.1). As a result, mass transport is unlikely to limit reaction rate at the anode. Conversely, atmospheric air fed into the cathode has a low molar fraction of oxygen ($\approx 21\%$), and oxygen has a moderate diffusion coefficient in air [13]. Water produced at the cathode further retards the diffusion of oxygen by decreasing the effective area for transport to occur. Therefore, mass transport resistance arises primarily at the cathode due to the diminishing oxygen concentration at reaction sites, which impedes electrochemical performance.

Minimizing concentration polarization losses at the cathode is of particular interest for PEMFCs because it allows a smaller, lighter, and less expensive fuel cell to be used for a particular automotive application. Ultimately, the commercial success of PEMFCs and their competitiveness with the internal combustion engine for transportation applications lies in their ability to perform optimally at high current densities [12, 14].

1.3 The Gas Diffusion Layer

At the centre of a typical PEMFC, the membrane-electrode assembly (MEA) is comprised of a $50\mu m$ thick membrane coated with a platinum catalyst on either side. Surrounding this, $200\mu m$ thick gas diffusion layers (GDLs) connect the MEA to the bipolar plates at the anode and cathode, which contain channels for the distribution of reactants over the electrode surfaces.

The role of the GDL is best understood by imagining the PEMFC as a network of porous materials. The catalyst layer contains extremely small pores in order to achieve a large surface area that maximizes the number of reaction sites. Attempting to distribute gases over large distances within the catalyst layer would require enormous pressure gradients that would make a PEMFC uneconomical to operate. Instead, the bipolar plates, which can be envisioned as a material with large pores, are used to distribute gases efficiently over the electrode area with minimal pressure drop to a near region within $200 - 250\mu m$ of the catalyst layer. The link between the catalyst layer and the bipolar plates is the, appropriately named, gas diffusion layer (GDL). A through-plane porosity gradient in the cell is created by the GDL, which contains a pore size that is greater than the catalyst

layer but less than the bipolar plates.

Acting as a transitional material, the GDL has several functions due to its location between the catalyst layer and bipolar plates.

- Mechanically support the MEA while maintaining good contact with the bipolar plates and catalyst layer to minimize thermal and electrical contact resistance.

- Sufficiently porous to allow the passage of reactants from the flow channels to reach reaction sites, including those reactions sites under the flow channel lands.

- Enable the removal of water produced at the reaction site to reach the flow channels, without dramatically affecting the flow of reactants.

- Act as an electrical bridge between the membrane and bi-polar plates with minimal electrical resistance.

- Transfer heat produced by the MEA to the bipolar plates, where coolant channels are located.

The GDL used in a conventional PEMFC consists of graphitized carbon fibres that are either held together with a carbon binder as a paper, or woven as a cloth (Figure 1.3). The binder consists of a carbonized thermoset resin that is cured at high temperatures [15], visible in Figure 1.3. The result is a material that is anisotropic and highly porous ($\geq 70\%$). The GDL is commonly impregnated with a hydrophobic agent such as Polytetrafluoroethylene (PTFE) to aid in liquid water removal. Water accumulation in the cell can cause concentration polarization losses and in some cases reactant gas supply can be cut off, a phenomenon referred to as flooding.

The performance of the cell at high current densities is strongly dependent on the performance of the gas diffusion layer. The number of interdependent operating variables presents a particular challenge for optimally designing a GDL, and as a result, significant effort has been directed at determining the effective transport properties through GDLs [14].

(a) Carbon Paper   (b) Carbon Cloth [16]
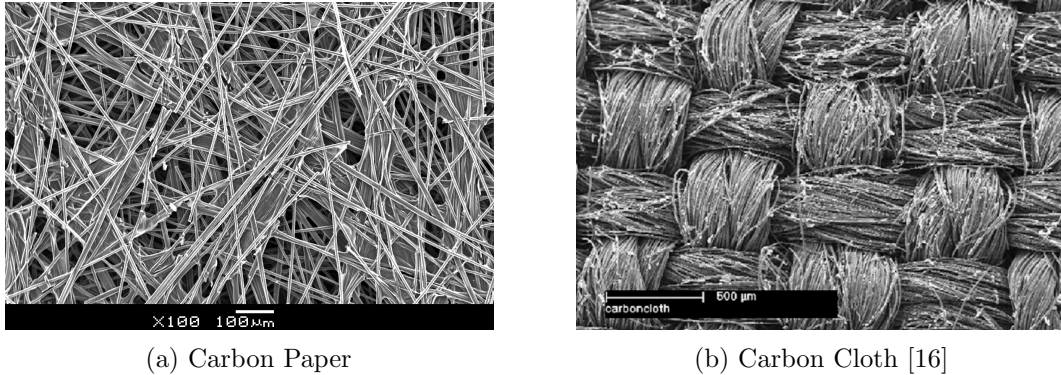
Figure 1.3: SEM micrographs of various gas diffusion layers at 100x magnification.

1.4 The Microporous Layer

At high current density operation (e.g. $2A/cm^2$ and above), both heat and water management become challenging within a PEMFC [8–10]. For example, heat flux can reach the order of $104W/m^2$, which borders the critical heat flux for water phase change.

Heat and water management requirements have led to the development of the microporous layer (MPL). It has been demonstrated that applying an MPL, consisting of carbon or graphite powder and a polymeric binder (typically PTFE), to the face of the GDL in contact with the catalyst layer (Figure 1.4) improves cell performance at high current densities [11]. The MPL has a pore size that is significantly smaller than the GDL, on the order of $100 - 500nm$ as compared to $10 - 30\mu m$ in the GDL.

The actual MPL mechanisms that improve cell performance at high current densities are still under debate due to the difficulties in observing transport phenomena in an operating fuel cell. However, it is believed that the MPL minimizes the electrical contact resistance, reduces the protrusion of the catalyst layer into the GDL, and mitigates water accumulation along the cathode catalyst layer so that gases can reach catalyst sites [17].

8
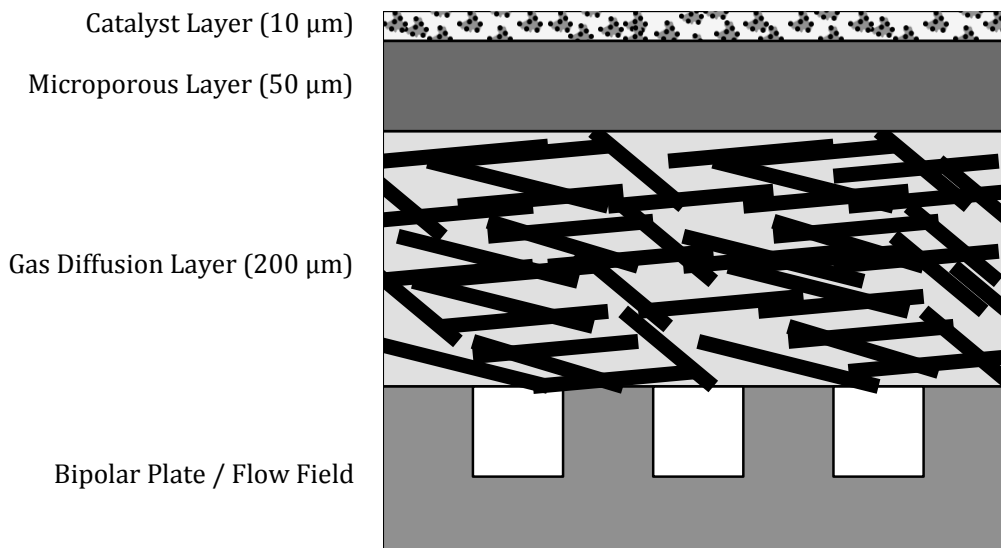
Figure 1.4: Cross section of a polymer electrolyte membrane fuel cell electrode [2].

1.5 Motivation For This Work

The measurement and correlation of heat and mass fluxes is of considerable importance to the polymer electrolyte membrane fuel cell (PEMFC). At high current densities the electrochemical reaction becomes rate-limited by the mass diffusive flux through the GDL and MPL, while through-plane temperature gradients dictate where water will condense impacting both gas reactant flow and the transport of heat out of the cell. A thorough understanding of how the microstructure and operating conditions of porous materials affect the diffusive flux of heat and mass can lead to improvements in fuel cell design. However, heat and mass transport through a PEMFC is a highly complex process and exceedingly difficult to model. Despite these challenges, the next generation of fuel cells will be the result of a concerted modelling effort to understand the intimate details of the transport mechanisms taking place in an operating fuel cell, and the accuracy of such models will depend on precise knowledge of transport properties such as gas diffusivity, gas and liquid

9

permeability, and electrical, ionic, and thermal conductivity. In lieu of mathematical models to predict these properties, whose accuracy will always be limited by a set of underlying assumptions, physical measurements must be conducted. For PEMFC porous media, physical measurements are particularly challenging due to their sub-millimetre thickness and the wide range of operating conditions, e.g., temperature, pressure, humidity, compression, that influence transport flux in an operating fuel cell.

1.6 Scope and Outline of Thesis

In this thesis, new experimental techniques are developed to measure the heat and mass transport in PEMFC porous media with a significantly higher degree of accuracy than has been previously achieved. These techniques are applied to measure the gas diffusivity, thermal conductivity, and thermal contact resistance of gas diffusion layers (GDL) and microporous layers (MPL) presently used in state-of-the-art fuel cells. Further, this thesis demonstrates the suitability of these techniques for measuring the catalyst layer of a PEMFC, for which there is significant research interest.

This thesis is divided into six chapters. In chapter one, the impact of heat and mass flux on the performance of polymer electrolyte membrane fuel cells is presented. The GDL and MPL are discussed in terms of their composition and function in a fuel cell. In chapter two, heat conduction and gas diffusion transport mechanisms are described, with a discussion on how the processes are fundamentally related. Modifications to the governing continuum equations are presented for flow through porous media such as the GDL and MPL. In chapter three, a literature review of experimental methods used to measure heat conduction and gas diffusion transport properties in porous media is presented, with a focus on the accuracy of each method. Mathematical models and correlations developed to predict such properties are also described. In chapter four, experimental apparatuses to measure the heat conduction and gas diffusion transport properties of PEMFC porous media are developed to exceed the accuracy of previous measurement techniques used in literature. The calculation and subsequent reduction of measurement uncertainty is emphasized in the experimental design. Chapter five discusses the results of the transport property measure-

ments of various GDLs and MPLs, making reference to how the microstructure influences these properties. Characteristics of the microstructure, too small for direct observation, are measured using standard contact porosimetry and observed using electron microscopy. Finally, chapter six gives a summary of major conclusions and presents recommendations for future work.

Chapter 2

Transport Mechanisms in PEMFC Porous Media

Porous media of interest in a PEMFC are the gas diffusion layer (GDL), microporous layer (MPL), and catalyst layer (CL). However, these materials present a challenge for the modelling of transport mechanisms due to their exceedingly complex microstructure. As a result, continuum equations are used to describe the transport of a conserved quantity such as mass, energy, momentum, and electric charge, in terms of the macroscopic properties of the medium. Microscopic material properties are, in effect, averaged into macroscopic effective transport properties based on the effective medium theory [18, 19].

The following chapter discusses the characteristic microscopic material properties of porous media and introduces the macroscopic transport mechanisms that are the focus of this thesis: gas diffusion and heat conduction. The governing equations are described to give context on how the effective transport properties may be used to estimate heat and mass transport through porous media.

2.1 Properties of Porous Media

2.1.1 Porosity

Porosity, ϵ, is a measure of the amount of void space in a solid material, expressed as a fraction of the total volume occupied by the pores, such that,

$$\epsilon = \frac{V_v}{(V_v + V_s)} \tag{2.1}$$

where V_v is the pore volume and V_s is the volume of the solid. There are three types of pores illustrated in Figure 2.1. Through pores, connecting pathways (1) and (2), are used for mass transport through the porous media. Dead-end pores typical of (3) and closed pores typical of (4) are accounted for in Eq. (2.1) but do not participate in the mass transport through the material. In general, macroscopic properties such as pore size distribution are easy to measure, as will be discussed in Section 4.1. However, none of the methods are able to determine the shape or effective length of the pores, or whether the pores are dead-ended or closed. Such methods would require direct observation of the pore network, which is made difficult by the minute length scale of the pores. Optical techniques such as micrography or tomography enable some of this information to be determined, but micrography is limited to surface characteristics and the resolution of tomography does not enable all pores to be estimated accurately.

The pore structure of a GDL is non-uniform with a broad range of pore sizes and shapes. In addition, the layered fibrous structure results in a geometric anisotropy between the in-plane and through-plane directions. Figure 2.1 shows a representative pore network of a GDL where the in-plane path length (1) is shorter than the through-plane path length (2).

2.1.2 Tortuosity

Tortuosity, τ, is commonly defined as the length of a 'tortuous' path, L, (such as (1) and (2) in Figure 2.1) divided by the straight-line distance through a porous solid, C, or

$$\tau = \frac{L}{C} \tag{2.2}$$
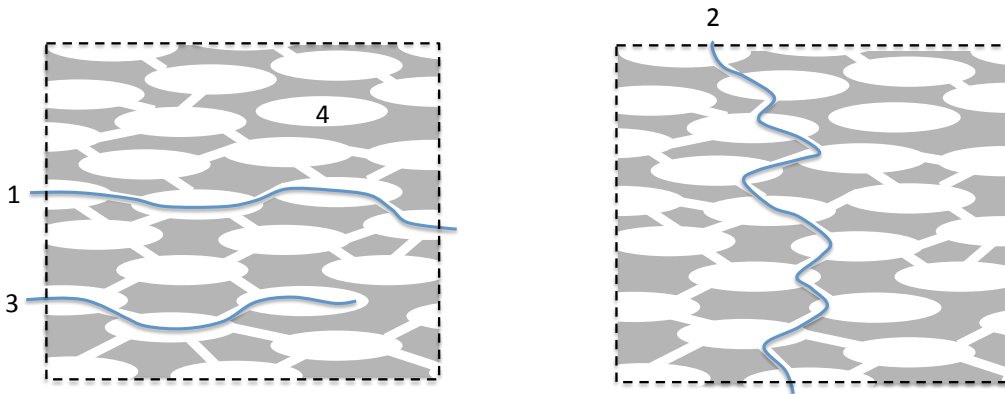
Figure 2.1: Representative pore network of a gas diffusion layer showing (1) an in-plane pathway of connected pores, (2) a through-plane pathway of connected pores, (3) a dead-end pore, and (4) a closed-off pore.

where τ equals 1 for a straight line and infinity for a circle. For anisotropic materials such as the GDL, τ is dependent on direction.

For bulk flow through a porous solid, tortuosity provides the deviation of the real flow from the idealized flow, predicted by the effective area using porosity, ϵ. Tortuosity quantifies aspects of the pore network that are not accounted for with porosity. For example, dead-ended and closed pores tend to increase the length of the tortuous path through a network of pores.

2.2 Gas Diffusion

The primary mode of mass transport for delivery of reactants [20] in a PEMFC is gas diffusion, governed by molecular, Knudsen, viscous, and nonequimolar diffusion theories [21]. Gas diffusion is dominated by molecular diffusion, the relative motion of different gas species along concentration gradients over time, and can be expressed using Fick's Laws. Fick's first law states that the mass flux, J_i, of a binary system is proportional to a diffusion coefficient and the gradient of mass concentration. For catalytic surface reactions, such

as those in a PEMFC, it is useful to define mass transport in terms of species flux rather than species concentration, at a surface. As such, the mass flux, F_i, of gaseous species, i, relative to stationary coordinates is,

$$F_i - \omega_i(F_i + F_j) = -\rho_g D_{ij} \nabla \omega_i \qquad (2.3)$$

where ω_i is the mass fraction of species i, ρ_g is the density of the gas ($M^1 L^{-3}$), and D_{ij} is the gas diffusion coefficient ($L^2 T^{-1}$) between species i and j. Fick's second law of diffusion expresses the concentration of a species as a function of time for a binary gas system, such that,

$$\frac{\partial C_i}{\partial t} = D_{ij} \nabla^2 C_i \qquad (2.4)$$

where C_i is the concentration of the gaseous species i, and t is time (T^1).

Flow through porous media are often described by modifying Fick's law with an effective diffusion coefficient, D_{ij}^{eff}, that takes into account the obstruction that the non-participating material has on the flow, such that,

$$D_{ij}^{\text{eff}} = f(\epsilon, \tau) D_{ij} \qquad (2.5)$$

where $f(\epsilon, \tau)$ is the diffusibility, ϵ is the porosity, and τ is the tortuosity. The adjustable parameter tortuosity is included to account for the shape, orientation, and effective length of the pores. The binary gas diffusion coefficient is inversely proportional to the absolute pressure and molar masses, and directly proportional to the temperature. The effect of temperature has been extensively measured in literature [13, 22]. Classical kinetic theory predicts that the binary gas diffusion coefficient, D_{ij}, varies with absolute temperature raised to the power of 1.5, while experimental measurements have shown this value to be around 1.75 [13, 23] in the temperature range that is applicable to PEMFCs.

For molecular diffusion, molecule-to-molecule collisions are the primary resistance to flow, which implies a system without walls. In a porous media where the mean free path of the diffusing molecule is much smaller than the characteristic length, or size, of the pore, this definition is sufficient. However, Knudsen diffusion must be considered when the pore size is the same order of magnitude as the mean free path, or when the Knudsen number

is near or greater than one. The Knudsen number, Kn, is defined as the ratio of the mean free path of a molecule to the pore diameter,

$$Kn = \frac{k_b T}{\sqrt{2}\pi\sigma^2 PL} \tag{2.6}$$

where k_b is the Boltzmann constant ($M^1 L^2 T^{-2}\theta^{-1}$), T is the temperature (θ^1), σ is the molecular diameter (L^1), P is the pressure ($M^1 L^{-1} T^{-2}$), and L is the characteristic length or pore diameter (L^1). The Knudsen diffusion coefficient can be estimated as a function of pore radius for well defined capillaries [24]. However, the complex microstructures present in PEMFC porous media negate the use of such methods. Instead, the Knudsen diffusion coefficient $D_{ij,\mathrm{K}}$ can be related to the Klinkenberg factor [25] by,

$$D_{ij,\mathrm{K}} = \frac{k_g b_i}{\mu_i} \tag{2.7}$$

where k_g is the gas permeability and b_i is the Klinkenberg coefficient, which is a function of the porous medium, fluid, and temperature. The complex microstructure of the porous medium is accounted for in the gas permeability, k_g.

2.3 Heat Conduction

Heat conduction is the primary mode of removing the heat generated by the electrochemical reaction in a PEMFC. Analogous to Fick's law for gas diffusion, Fourier's law for heat conduction describes the rate of heat transfer through a material along temperature gradients over time, such that,

$$\frac{1}{\alpha}\frac{\partial T}{\partial t} = \nabla^2 T \tag{2.8}$$

where $\alpha = k/\rho c_p$ is the thermal diffusivity of the conductor ($L^2 T^{-1}$), T is the temperature (θ^1), and t is time (T^1). Thermal diffusivity represents an important thermophysical property that encompasses the thermal conductivity, k, and the thermal capacity, ρc_p of a material. High thermal conductivity is associated with a high rate of heat transfer, while low thermal capacity is associated with large temperature changes during transient conduction.

For PEMFCs, the thermal conductivity of the various cell components is the most pertinent material property since the cell will spend most of its time operating at a steady or quasi-steady state. For the anisotropic structure of the GDL,

$$k = k(\vec{r}, T) \tag{2.9}$$

where $\vec{r}$ is the position vector and T is the temperature of a point in the solid. However, k is typically regarded as constant in Eq. (2.8) for a given direction and average temperature in a homogeneous solid, otherwise the equation becomes significantly more complex due to the non-linearity. Further, when the temperature field is steady in time, Eq. (2.8) becomes Laplace's equation, or

$$\nabla^2 T = 0 \tag{2.10}$$

The solution to Laplace's equation is a temperature distribution that is only dependent on the geometry of the conductor and the boundary conditions, not the thermophysical properties (k, ρ, c_p) of the conductor. The steady-state temperature distribution only becomes a function of thermal conductivity if a boundary condition is specified as a heat flux.

GDLs are comprised of several materials of varying thermal conductivities due to their porous and heterogeneous structure, including graphite fibres, carbon binder, a hydrophobic polymer, and a fluid that occupies the pore voids. The fluid may consist of hydrogen gas, the gas constituents of atmospheric air, water vapour, and liquid water. As a result, many different in-series and parallel heat conduction pathways form a complex network of heat flows. Thus, it is convenient to define an effective thermal conductivity, k_{eff}, that considers all of the varying thermal resistances as one weighted average. The heat flux $\vec{q}$ through a porous material such as a GDL can be written as,

$$\vec{q} = -k_{\text{eff}} \nabla T \tag{2.11}$$

Despite being comprised of highly conductive graphitized carbon fibres, the GDL has a relatively low effective thermal conductivity due to the thermal contact resistance between fibres and the high porosity of the material. The MPL also has a low effective thermal conductivity due to the high PTFE %-wt. content used to hold the carbon powder together.

2.3.1 Thermal Contact Resistance

A special case of heat conduction called thermal contact resistance occurs at the interface between two solids in contact. Due to the surface roughness of real materials, physical contact is only achieved at a finite number of locations in Figure 2.2. In a PEMFC, thermal contact resistance is present where a GDL contacts an adjacent catalyst layer or bipolar plate, as well as fibre-to-fibre contact within a GDL.
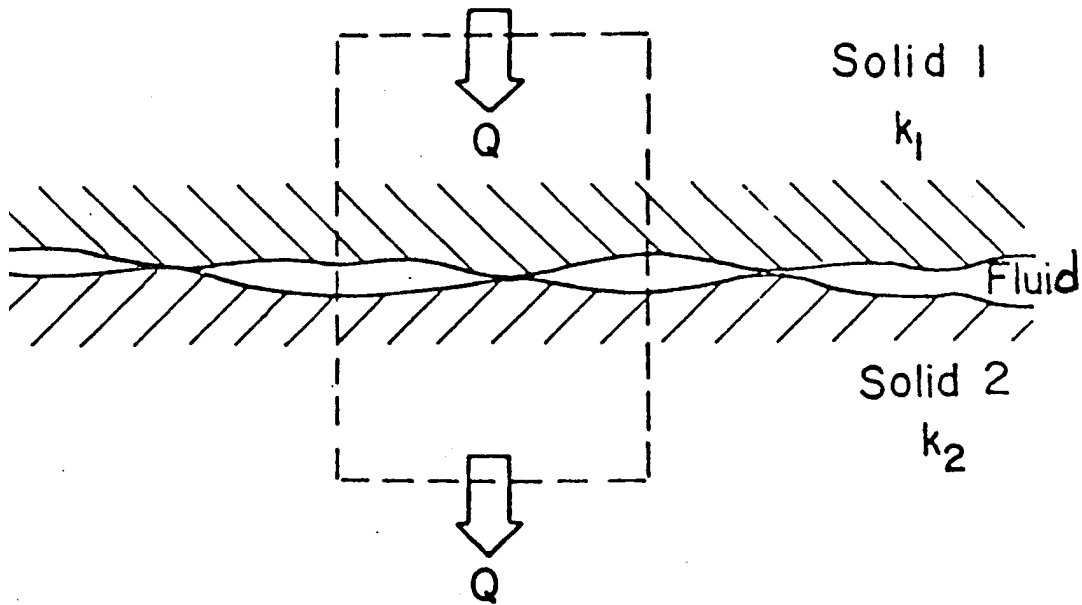
Figure 2.2: Thermal contact resistance between two materials caused by the imperfect nature of real surfaces. A finite number of contact points exist between two solids pressed together, separated by stagnant gas voids [3].

Considering the rectangular control volume in Figure 2.2, heat must conduct from Solid 1 to Solid 2 through a stagnant gas layer of thickness, L. The rate of conduction is determined by the distance between the solids, which can be described by three regimes of decreasing pore size: continuum, slip flow, and free molecule flow.

In the continuum regime, molecule-to-molecule collisions in the gas phase are the rate controlling mechanism. As such, thermal resistance of the gas layer is determined by the macroscopic thermal resistance, R,

$$R = \frac{L}{kA} \tag{2.12}$$

where k is the thermal conductivity of the gas, depending only on the temperature and type of gas, and A is the surface area perpendicular to the heat flow [26].

When the Knudsen number, Kn, defined in Section 2.2 is very large ($Kn \geq 10$), molecules are said to be in the free molecule flow regime. Here, each molecule of gas travels directly from one surface to the other without colliding into other molecules. As a result, the thickness, L, between the surfaces has no physical significance.

The slip flow regime is prevalent when the mean free path of the molecules is of the same order of magnitude as the thickness, L, ($Kn \approx 1$). Akin to a transitional regime, heat transfer occurs by both continuum and free molecule flow regimes.

For GDLs, thermal contact resistance can be minimized by reducing L of the stagnant gas layer. THis is achieved in PEMFCs by applying compression force to the cell layers in order to deform adjacent materials and improve surface-to-surface contact. Due to the layered fibrous structure of the GDL, compression force readily deforms the material by bringing fibres into closer contact with one-another. This reduces the thickness of the GDL, which reduces porosity and increases k_{eff}.

2.3.2 Constriction Resistance

Neither the effective heat or gas diffusivity through porous media can be described solely by porosity. For gas diffusion, tortuosity describes the barriers to flow that exist due to the twists and turns of the pore network. For heat conduction, there is no comparable parameter for describing the barriers to flow, since heat can conduct through all materials and all physical states to varying degrees. However, a constriction resistance at the macroscopic and microscopic level can be used to describe the impedance to heat conduction that occurs in a porous solid. Figure 2.3 shows the heat flow lines through these regions, where microscopic constriction resistance is analogous with thermal contact resistance in Section

19

2.3.1. Heat conduction through the stagnant gas layer is negligible at the macroscopic level due to the large distances between solids and low thermal conductivity of gases ($Kn \approx 0$). At the microscopic level, conduction through the gas layer becomes non-negligible as the distance between the solids becomes small ($Kn > 0$).
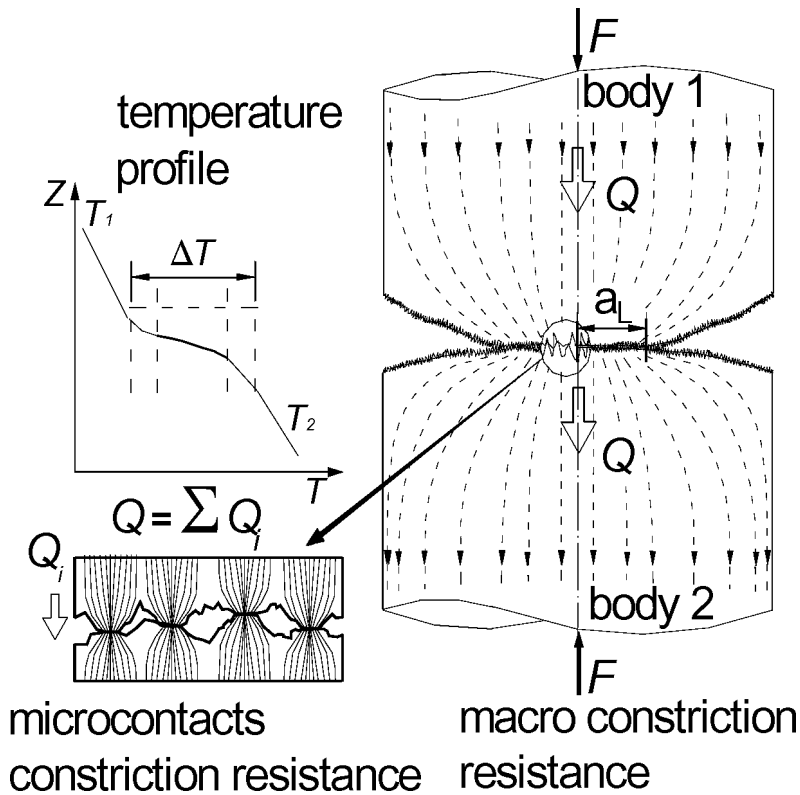
Figure 2.3: Thermal constriction resistance [4].

The constriction resistance within a porous solid, such as the fibrous structure of a GDL, is impractical to calculate due to the difficulties in estimating the effective contact area between two surfaces, and the variability in effective areas at different contact points. As a result, constriction resistance, similar to tortuosity, must be deduced from experiment means using a suitably large sample to provide a representative average of all constriction resistances.

20

2.4 The Combined Study of Heat and Mass Transport

At first glance, the combined study of heat conduction and gas diffusion through porous media may seem disconnected considering their differing roles in the operation of a fuel cell. Gas diffusion occurs in the gas phase voids of porous media to transport reactants and products, while heat conduction occurs primarily in the solid phase of porous media to remove waste heat. However, gas diffusion and heat conduction are intimately related in both their physical mechanisms and how they can be experimentally measured.

2.4.1 Governing Behaviour

Heat conduction and gas diffusion transport processes are dominated by molecule-to-molecule collisions described with kinetic theory. Fick's Law (Section 2.4) for gas diffusion and Fourier's Law (Section 2.8) for heat conduction are based on the general diffusion equation [27],

$$\frac{\partial \rho(\vec{r}, t)}{\partial t} = D \nabla^2 \rho(\vec{r}, t) \tag{2.13}$$

where $\rho(\vec{r}, t)$ is the density of the diffusing species (temperature or molar concentration) that is a function of position, $\vec{r}$, and time, t. D is the diffusion coefficient that determines the rate at which species diffuse and, in its simplest form, is assumed to be a constant.

The heat and mass flux through porous media may also be considered a function of one-another. With heat conducting primarily through solid material and mass conducting through the porous voids, a change in material geometry oppositely affects both parameters. For example, the through-plane compression of a GDL will result in a decrease in porosity that reduces the gas diffusivity while simultaneously increasing the heat conductivity. Similarly, liquid water present increases the number of pathways for heat to travel through the material while reducing the number of gas pathways.

The relationship between heat and mass flux can be further understood by considering a geometric model of a porous structure for predicting transport properties. Das *et al.* [28] proposed using the Hashin coated sphere model [29] for predicting transport properties in PEMFC catalyst and gas diffusion layers, which allows the effective gas diffusivity, D_{eff},

and the effective thermal conductivity, k_{eff}, to be written as,

$$\frac{D_{\text{eff}}}{D_{\text{bulk}}} = 1 - \lambda_g \left(\frac{3(1 - \epsilon)}{3 - \epsilon} \right) \tag{2.14}$$

$$\frac{k_{\text{eff}}}{k_{\text{bulk}}} = 1 - \lambda_g \left(\frac{3\epsilon}{3 - (1 - \epsilon)} \right) \tag{2.15}$$

where only the terms representing void space, ϵ, and solid space, $(1 - \epsilon)$, switch places in each equation. λ_g is a geometric factor that accounts for the unique geometry of a porous media, and must be estimated using an appropriate experimental scheme. Zamel *et al.* [30, 31] used a numerical simulation of the heat conduction and gas diffusion process through a 3D representation of a GDL to generate an expression for the geometric factor in each case. D_{bulk} and k_{bulk} are the diffusion coefficient of the bulk gas and the thermal conductivity of the bulk solid material, respectively.

2.4.2 Experimental Measurement

The flow of heat and gases through PEMFC porous media cannot be directly observed, nor can they be easily measured in-situ due to the minute length scales involved, which is discussed in more detail in Chapter 4. As a result, ex-situ experimental measurements of effective transport properties must be inferred from probes placed adjacent to the material of interest. In both cases, the flux of heat and mass through a material can be determined from the flux entering or exiting the material by means of conservation laws. Then, Eq. (2.13) can be applied with knowledge of the material geometry to evaluate the thermal or mass diffusivity, D. Suitable methods for generating and measuring heat and mass flux are the subject of Chapter 4.

Chapter 3

Literature Review

3.1 Effective Gas Diffusivity

The effective gas diffusion coefficient for porous media, D_{ij}^{eff}, that takes into account the obstruction that the solid has on the flow, is often expressed as,

$$D_{ij}^{\text{eff}} = f(\epsilon, \tau) D_{ij} = \frac{\epsilon}{\tau} D_{ij} \tag{3.1}$$

where $f(\epsilon, \tau)$ is the diffusibility, ϵ is the porosity, and τ is the tortuosity. The adjustable parameter tortuosity is included to account for the shape, orientation, and effective length of the pores. It is defined as the length of a 'tortuous' path divided by the straight-line distance through a porous solid. However, tortuosity cannot be readily measured. Thus, the diffusibility $f(\epsilon, \tau)$ is expressed by many geometric models as a function of only ϵ [32]. The most well known diffusion model in PEMFC literature is by Bruggeman [33],

$$f(\epsilon) = \epsilon^{1.5} \tag{3.2}$$

The shortcoming of the Bruggeman model is that it is based on the porosity between spherical particles, a significant departure from the geometry of a GDL. Das *et al.* [28] acknowledged this limitation when formulating a mathematical model for GDL diffusivity based on the Hashin coated sphere model,

$$f(\epsilon) = \left(1 - \lambda_g \left(\frac{3(1-\epsilon)}{3-\epsilon}\right)\right) \tag{3.3}$$

23

where λ_g is a geometric factor that accounts for the fibrous geometry of GDLs, and must be estimated using an appropriate experimental scheme. Zamel *et al.* [30] used a numerical simulation of the diffusion process through a 3D representation of a GDL to generate an expression for the geometric factor, of the form,

$$\lambda_g = \epsilon A \cosh(B\epsilon - C) \tag{3.4}$$

where A, B, and C are fitting parameters. More recently, Tomadakis and Sotirchos [34, 35] proposed the following model using random cylindrical fibres,

$$f(\epsilon) = \frac{0.9126}{\epsilon(\epsilon - 0.11)^{0.785}} \tag{3.5}$$

Unfortunately, experimental measurements [36–39] have shown that many of these correlations for porous media significantly over predict D_{ij}^{eff} in GDL. This is a considerable issue for numerical studies that model PEM fuel cell performance using these correlations, especially at high current density conditions where reaction rate is limited by mass transport.

In order to formulate a more appropriate correlation, a number of studies have focused on experimentally measuring the diffusion coefficient of commercially available GDLs. Baker *et al.* [40, 41] and others [42, 43] made in-situ limiting current measurements to characterize gas transport resistance in an operating PEM fuel cell. They were able to separate the effect of the GDL on the overall gas transport resistance in the cell, however it was not possible to distinguish between in-plane and through-plane diffusion, variations in compression by the bipolar plates, and mass transfer due to convection. In another study, Baker *et al.* [40] was able to isolate these parameters by measuring water vapour diffusion with an ex-situ apparatus. The simple technique involved measuring the evaporation rate of water through a GDL, which is a function of the diffusibility of the GDL. However, this method required at least 24 hours to perform one measurement, limiting the practical number of operating conditions and materials that could be evaluated. Kramer *et al.* [36] and others [38, 44, 45] used electrochemical diffusimetry, a novel analogy between electrical resistance and gas diffusion, to determine ϵ/τ in a GDL. Their results compared well with Baker *et al.* [40] at compressions of less than 25%. However, the primary limitation of this method is that diffusibility of the GDL is inferred rather than directly measured. Furthermore, electrochemical diffusimetry may not be appropriate for quantifying diffusion in the pores

of the microporous and catalyst layers of the PEMFC, regions where Knudsen diffusion dominates and the relation between Fick's law and Ohm's law is no longer valid. This limits the usefulness of this technique beyond GDL. LaManna *et al.* [39] used a parallel flow mass exchanger, otherwise referred to as the Wicke-Kallenbach technique, to measure vapour diffusion rates across various GDLs with a stated uncertainty of 22%. While the sources of the uncertainty are not discussed, operating the inlet gas stream at 95% relative humidity and 25°C can lead to large errors in relative humidity measurements from temperature variations on the order of (10^{-1})°C. More accurate measurements could be achieved by operating the apparatus at 80°C, a temperature where the air holds significantly more water vapour and small temperature changes have less effect on relative humidity. Zamel *et al.* [37] and a similar study by Chan *et al.* [46] modified a Loschmidt cell, normally used to evaluate binary gas diffusion coefficients, to measure the diffusive flux through a GDL. The Loschmidt cell directly measures gas concentration and is simple by design, requiring only limited assumptions. The measurement system has the potential to provide more accurate measurements than other discussed techniques, and has already been well demonstrated for binary gas systems [13]. However, the experimental uncertainty in the GDL diffusivity measurements conducted by Zamel *et al.* [37] is large, as will be shown in Chapter 4, and grows exponentially large for the measurement of thinner materials pertinent to the development of PEMFCs such as the microporous layer [46] and catalyst layer [47].

3.2 Effective Thermal Conductivity and Contact Resistance

The effective thermal conductivity, k_{eff}, considers the relative influence of the various solid and fluid phases on conductivity within a porous media. It is a function of porosity and thermal conductivity, such that,

$$k_{\mathrm{eff}} = f(\epsilon, k_s, k_f) \tag{3.6}$$

where ϵ is the porosity, and, k_s and k_f are the average thermal conductivities of the solid and fluid phases (pore voids) within a porous media, respectively. For example, depending

on the composition of a GDL, k_s is a function of the thermal conductivity and orientation of the graphite fibres (due to anisotropy), carbon binder, PTFE, and the inter-fibre contact resistance. Depending on the operating conditions of a particular fuel cell, k_f is a function of the thermal conductivity of hydrogen, oxygen and nitrogen gases, water vapour, and any liquid water present. Considering the complex nature of the effective thermal conductivity of PEMFC porous media, a wide range of values have been quoted in literature. For the GDL, k_{eff} between 0.15 and $65 W/mK$ have been used in PEMFC models, e.g. [48–51], among many others.

Both theoretical and experimental methods have been applied in literature to determine the effective thermal conductivity of PEMFC porous media. Baschuk and Li [48] and later Wu *et al.* [52] used an arithmetic mean correlation to estimate k_{eff} of GDL as a function of ϵ, k_s, and k_f. Due to the difficulties in determining the composition and arrangement of the various species in a PEMFC porous media, Pharoah *et al.* [53] calculated a maximum and minimum bound that the effective thermal conductivity of a GDL must lie within based on a mixing-law model. However, these models neglect the structural effects such as contact and constriction resistance described in Section 2.3.2. Sadeghi *et al.* [54] created an analytical model for fibrous GDLs that accounts for conduction in both the solid and gas phases, constriction and contact resistance from overlapping fibres, and geometric features such as fibre orientation and compression from cell clamping. Similar to the correlation developed for effective gas diffusivity, Das *et al.* [28] used the Hashin coated sphere model to estimate effective thermal conductivity, that is

$$\frac{k_{\mathrm{eff}}}{k_{\mathrm{bulk}}} = 1 - \lambda_g \left(\frac{3\epsilon}{3 - (1 - \epsilon)} \right) \tag{3.7}$$

where λ_g is a geometric factor that accounts for the fibrous geometry of GDLs, and must be estimated using an appropriate experimental scheme. Zamel *et al.* [31] used a numerical simulation of the heat conduction process through a 3D representation of a GDL to generate an expression for the geometric factor for both in-plane and through-plane conduction, of the form,

$$\lambda_g = A(1 - \epsilon)^B \exp[C(1 - \epsilon)] \tag{3.8}$$

where A, B, and C are fitting parameters. Similarly, Veyret *et al.* [55] developed a 3D numerical model of two GDL structures and estimated their effective thermal conductiv-

ity. The limitations of theoretically estimating thermal conductivity is that the model's assumptions must still be validated with experimental data. Another concern is that the thermal conductivity of materials with an inhomogeneous and random structure, such as the GDL, may be impossible to predict from a measure of porosity alone. There are significant variations in microstructure between GDLs from different manufacturers as will be shown in Section 5.1.4. Ramousse *et al.* [56] concluded that many of the theoretical values for k_{eff} of GDLs are highly overestimated in literature. Basing correlations on experimental data is a way to alleviate the discrepancies between experimental data and theoretical models.

The first experimental studies to measure the thermal properties of GDL were carried out by inserting thermocouples into an operating fuel cell to measure through-plane temperature gradients [57, 58]. However, temperature gradients, pressure from the bipolar plates, and mass transport and phase changes of water vary over the in-plane area of an operating PEMFC. Without uniformity of these parameters, their effect on the measured thermal conductivity cannot be isolated. More fundamentally, large sources of error arise from the intrusive nature of thermocouples placed in the cell due to the minute length scales of the cell components.

Subsequent studies have focused on ex-situ experimental techniques that allow for precise control of operating conditions, namely compression pressure and temperature. Ihonen *et al.* [59] was first to create such an apparatus and measure the effective through-plane and contact resistances for compressed GDL. However, the authors noted large sources of error owing to the design of the apparatus. Specifically, the material used to insulate the GDL from heat loss had a thermal conductivity of the same order of magnitude. The ex-situ technique of a guarded heat flux meter was first used to measure the thermal conductivity of the GDL by Khandelwal and Mench [60] who reported on the effects of temperature, PTFE content, and compression pressure. The through-plane effective thermal conductivity was shown to decrease with increasing temperature due to a change in thermal resistance of the binder material at elevated temperatures. PTFE coatings decreased the effective thermal conductivity of the GDL due to the low thermal conductivity of PTFE. This decrease reached an asymptotic minimum with increasing PTFE content. Thermal contact resistance was shown to decrease with increasing compression pressure, whereas

previous modelling studies had excluded the effects between GDL and adjacent materials [56, 61, 62]. Their findings, however, failed to account for the in-situ GDL thickness during measurement. Nitta *et al.* [63] used a similar technique, but found that effective thermal conductivity was independent of compression pressure. This result has not been corroborated in literature. Burheim *et al.* [64] measured the in-situ thickness, thus providing the most accurate results to date. They reported that the through-plane effective thermal conductivity increased with increasing compression pressure. Other studies have since arrived at a similar conclusion [65, 66]. Sadeghi *et al.* [67] investigated the effect of cyclic compressive loading on GDL and found that a thickness hysteresis existed. Zamel, *et al.* [68] conducted pore-scale modelling to show that the presence of water in the GDL structure increases the through-plane effective thermal conductivity of the GDL. Burheim *et al.* [69] experimentally measured an increase in through-plane effective thermal conductivity when liquid water was present in the GDL. The effective thermal conductivity was improved by the presence of water more than what could be predicted by replacing air with water in a volume averaged estimate. This is attributed to water being preferentially located at the intersection of individual fibres, thereby reducing fibre-to-fibre contact resistance. Zamel *et al.* [70] used the thermal capacitance slug calorimeter technique to measure GDL thermal conductivity over a temperature range of 50 to 120 °C. These temperatures may be experienced during start-up of an automotive fuel cell depending on the climate. They observed a distinct change in effective thermal conductivity below 35°C.

Although much effort has been focused on the measurement of the through-plane effective thermal conductivity of the carbon paper GDL, few experimental measurements can be found for a GDL containing a microporous layer (MPL) [64, 65] and no published results have isolated the thermal properties of the MPL from the GDL substrate. Despite the focus of the MPL being water management, transport properties in a PEM fuel cell are highly interdependent and a thorough understanding of the heat transfer properties of the MPL is crucial for accurate modelling of all transport properties. Due to the isotropic structure of the MPL, it is expected that through-plane properties will closely resemble in-plane properties as well.

Chapter 4

Characterization Methods

The thermophysical properties of PEMFC porous media are particularly challenging to characterize due to their thickness and complex microstructure. The thickness of these materials is on the order of micrometers, which can introduce large errors by measurement probes that do not have a fine enough spatial resolution. For example, even the smallest diameter thermocouple available is of the same order of magnitude as the thickness of the catalyst layer. As a result, a temperature measurement at a spatially precise location relative to the catalyst layer cannot be determined without introducing enormous error. Another challenge is the complex and inhomogeneous microstructure of the PEMFC materials. For example, the gas diffusion layer (GDL) can be deformed to an extent that the thermophyiscal properties will be changed by simply contacting the surface with a measurement probe.

In this chapter, three measurement techniques are discussed for characterizing the thermophysical properties of porous media, the method of standard contact porosimetry, the closed tube (Loschmidt) method, and the guarded heat flow method. In this work, the later two methods are modified to provide highly accurate measurements for the small thickness and complex microstructures found in PEMFC porous media.

4.1 Porosimetry

The microstructure and surface properties of porous materials may be quantified using porosimetry techniques to determine parameters such as pore diameter, total pore volume, surface area, and bulk density, among others. Of the numerous techniques in use [71–76], the method of standard contact porosimetry (MSP) and the method of mercury porosimetry (MMP) have the widest spectrum of measurable pore radii (from $2 - 10^5 nm$), necessary for the diverse range of pore sizes encountered in PEMFC materials. However, mercury porosimetry requires the sample to be subjected to mercury at high pressures that can damage the sample and distort results [74]. In addition, the toxicity of mercury is always of concern for operator and environmental safety. As a result, the MSP was chosen as the most suitable technique. A MSP apparatus purchased from Porotech Inc. (Toronto, Ontario) was used for this investigation.

4.1.1 Apparatus and Measurement Principle

The MSP technique relies on the laws of capillary equilibrium to infer characteristics about the structure and surface properties of an unknown porous sample from that of a known standard. For two or more porous media in capillary equilibrium and partially filled with a wetting liquid, the capillary potentials are equal, such that,

$$\psi_1 = \psi_2 = \ldots = \psi_i \tag{4.1}$$

where ψ is the capillary potential of material i.

Porous media reach capillary equilibrium by being in direct contact. Liquid and vapour flows distribute the wetting fluid through capillary pressure gradients so that capillary pressure, p_c can be related to the maximum radius of pores filled with a liquid, r_m, according to the Laplace equation,

$$p_c = -2\sigma \cos \frac{\theta}{r_m} \tag{4.2}$$

where σ is the surface tension and θ is the wetting angle.

The accuracy of the MSP technique is strongly dependent on the calibrated standard samples, whose properties are determined from independent measurements conducted by Porotech Inc. (Toronto, Ontario). The data that accompanies each standard sample is a function, f_s, that relates the capillary potential, ψ, to the volume of the liquid in the standard sample, V_s,

$$V_s = f_s(\psi) \tag{4.3}$$

The ratio of liquid volume in the standard sample, V_s, to that of the unknown porous sample, V_u, is found by weighing each sample individually over a range of liquid saturations to produce a function, f_v,

$$f_v = \frac{V_u}{V_s} \tag{4.4}$$

where saturation is varied by allowing the liquid in the samples to evapourate over time.

Using octane as the wetting liquid ($\theta \sim 0°$), and Eqs. (4.2), (4.3), and (4.4), it can be shown [73] that the pore size distribution, $F(r)$, can be expressed as the function,

$$F(r) \equiv f_v \left[f_s \left(-\frac{2\sigma}{r_m} \right) \right] \tag{4.5}$$

where r is the characteristic length, or radii, of the pore.

4.1.2 Experimental Procedure

The procedure to determine the shape of the pore size distribution curve of an unknown sample using the MSP technique is best described graphically in Figure 4.1. For a specific measurement point on the curve, the mass of the liquid in the sample, V_u is determined with a weigh-scale and plotted at (1). Subsequent measurements of the standard sample liquid mass, V_s, and overall liquid mass, $(V_u + V_s)$, give the relation (2). The volume of liquid in the standard sample (3), V_s, is used to located (4) on the standard sample curve, which gives the maximum pore radius filled with liquid (5) for both the standard and unknown sample (6). The point on the unknown sample curve is determined from the amount of liquid in the unknown sample, V_u, at (7), which is the same point from (1).

31
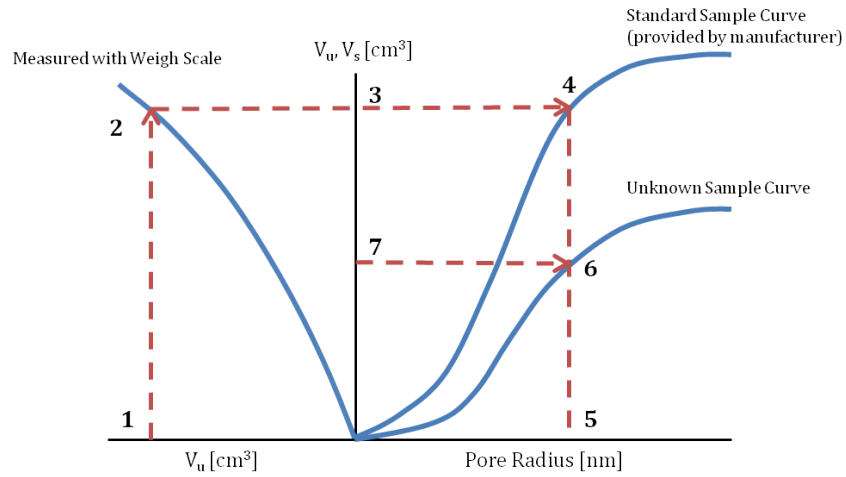
Figure 4.1: Graphical method of determining pore size distribution of an unknown sample using the Method of Standard Contact Porosimetry.

4.2 Gas Diffusivity

Mass transport within PEMFC porous media may be characterized by the diffusivity and the permeability of the material. The permeability of a material may be obtained with relative ease by measuring pressure drop as a function of flow rate. However, measuring the gas diffusivity of a material is considerably more difficult. A number of methods exist for determining the gas diffusion coefficient of binary gas systems, but only a limited number of these methods can be adapted to measure the diffusivity of a porous sample. The principal experimental methods for measuring gaseous diffusion coefficients are the closed-tube and the two-bulb methods, both extensively used in literature. Based on comparisons between various investigators, these methods are generally regarded to have uncertainties of about $\pm 2\%$ and reproducibility better than $\pm 1\%$ [13]. The Wicke-Kallenbach technique is often used for the measurement of porous media [77], however the reported uncertainty has been found to be at least twice that of the closed-tube and two-bulb methods. Other techniques designed principally for measuring diffusion across a porous medium require a large amount of time or are experimentally complex, and thus difficult to control uncertainty. These include the accumulation into a volume method and the steady-state diffusion across a

32

membrane method [78, 79].

In order to measure diffusion rates through porous media, the experimental techniques and data analysis methods developed for the measurement of pure binary gas diffusion must be modified. This topic is thoroughly discussed in this chapter. The closed-tube method was chosen over the two-bulb method for this investigation due to the drawbacks of using the two-bulb method. Namely, high accuracy is only achieved after sufficient optimization of the geometry, and several correction factors are required to account for non-ideal conditions that may arise such as Knudsen flow. These complications indicate a long development time, and difficulty diagnosing whether a systematic error is due to the measurement equipment or an incorrectly applied correction factor.

4.2.1 Apparatus and Measurement Principle

Loschmidt developed the closed-tube method in 1870 [80]. As a result, an experimental apparatus employing the closed tube method is commonly referred to as a Loschmidt cell. Diffusive flux is determined through mixture composition measurements in the Loschmidt cell, which are a function of both time and position in a long tube that is closed at both ends. Primary assumptions for this method are that diffusion occurs in one-dimension, the cell has a uniform cross section, and it is symmetrical about its mid-plane. It is also assumed that the diffusion coefficient is independent of concentration, which varies with time due to the transient nature of the method. For gases, this is generally true [22].

The Loschmidt cell must be modified to measure gas diffusion through porous media by allowing a sample to be placed near the midpoint of the long chamber. A schematic of the apparatus used in the present study is provided in Figure 4.2, whose design is an evolution of the modified Loschmidt cell in literature [37, 46, 47, 81–84]. Different gas species are contained in the upper and lower chambers of the cell separated by a sliding gate (5a), in this study nitrogen and oxygen, respectively. When the sliding gate is opened (5b), the gas species diffuse together through a sample placed at the interface between the two chambers. The oxygen concentration at a known point in the cell is measured as a function of elapsed time using an Ocean Optics FOXY-AL300 oxygen sensor.
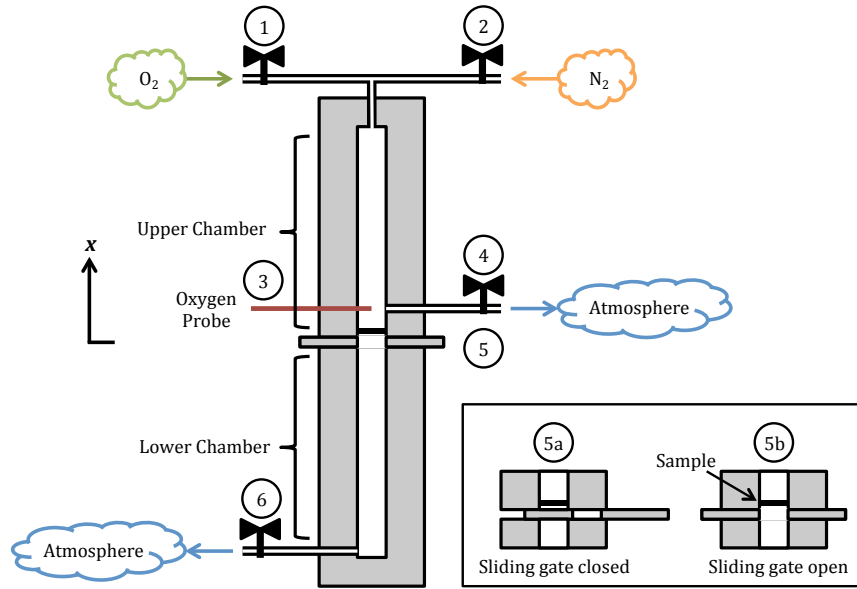
Figure 4.2: Modified Loschmidt cell used in the present study.

Performing a diffusion measurement begins by purging the cell with oxygen from inlet (1) and venting it to atmosphere at outlet (6) until the oxygen probe (3) stabilizes at 100% oxygen for a prolonged period of time. The sliding gate (5) is then closed to seal off the bottom chamber. Next, the upper chamber is purged with nitrogen from inlet (2) while venting it to atmosphere at outlet (4) until the oxygen concentration stabilizes at 0% for a prolonged period of time. Failure to achieve the exact 100% and 0% oxygen concentration set points at the oxygen probe (3) indicates a problem with the apparatus that could be related to mechanical sealing, oxygen probe calibration, or a software logic error. This provides a level of automated fault checking that is an improvement from the purging method described in previous studies [37, 81, 83]. The diffusion measurement proceeds by opening the sliding gate (5b) and monitoring oxygen concentration over a set period of time. The length of time required is discussed by Dong *et al.* [85] with the goal of maintaining a particular Fourier number to minimize error. A typical set of data collected by the oxygen probe at 0.5 sec intervals is provided in Figure 4.3 for an experiment involving a Toray TGP-H-120 GDL at 50 °C.
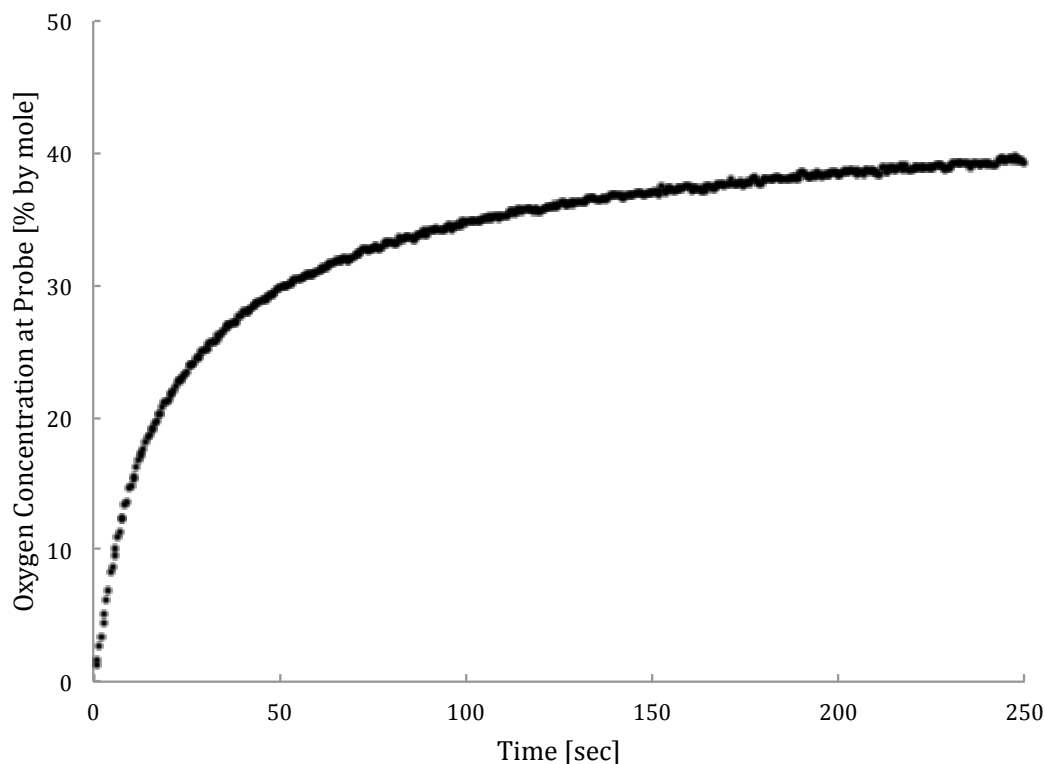
Figure 4.3: Oxygen concentration vs. time measured by the oxygen sensor for an experiment involving a Toray TGP-H-120 gas diffusion layer at 50 °C.

4.2.2 Oxygen Sensor and Phase Fluorometry

The diffusive flux through the Loschmidt cell is calculated from the oxygen concentration measurements of a single oxygen sensor probe. Thus, its calibration and measurement accuracy are paramount to achieving precise results. Through a measurement technique known as phase fluorometry, the oxygen sensor measures fluorescence quenching by oxygen molecules and correlates it to the partial pressure of an oxygen mixture. A luminophore (in this case ruthenium) tipped probe fluoresces when it is excited by a blue (470nm) LED source [86]. The florescence is quenched through a transfer of energy when a molecule of oxygen physically collides with a fluorophore in its excited state. Unlike nitrogen and

35

other molecules found in air, oxygen is uniquely able to quench the fluorescence of certain luminophores because it is a triplet molecule [87]. The remaining light energy is passed through the probe along an optical fibre to a spectrometer. Lifetime, κ , is calculated from the measured phase shift, ϕ, between the excitation LED and the fluorescence emission, and the frequency of the light, f, using the following formula,

$$\kappa = \frac{1}{2\pi f} \tan(\phi) \qquad (4.6)$$

The amount of fluorescence quenching depends on the rate of collisions, and therefore the concentration (or partial pressure) of oxygen in the cell. By extension, the measurements are sensitive to the absolute pressure and temperature of the gas mixture. Thus, regular calibration is necessary to account for daily fluctuations in atmospheric pressure and design temperature set points.

Exposing the oxygen sensor to a series of known oxygen concentrations allows the sensor to be calibrated. The nitrogen-oxygen gas composition is controlled by two Omega FMA-series mass flow controllers that feed the correct ratio of oxygen and nitrogen through inlets (1) and (2), past the oxygen sensor, and out through outlet (4) in Figure 4.2. A 20-point calibration (typical of Figure 4.4) is automatically performed before each set of runs to correlate measured κ values to oxygen concentration. A high order polynomial fit is applied to the data points in order to smooth the data, and to enable interpolation of other κ values.

4.2.3 Sensor Drift

Sensor drift is the largest concern for this type of measurement system. The manufacturer of the oxygen sensor lists the stability of the oxygen measurement as decreasing by 0.01% per hour at continuous operation. The drift is practically eliminated by re-calibrating the probe before each set of measurements using an automated process. However, Figure 4.5 shows the observed decrease in oxygen sensor accuracy over a period of 40 days that experiments were run for calibrations performed at 50 °C. The λ values for 0% and 100% oxygen concentrations (the two measurement extremes) decrease at a differing rate due to the probe being more sensitive to low oxygen levels. This effect decreases the range of κ

36
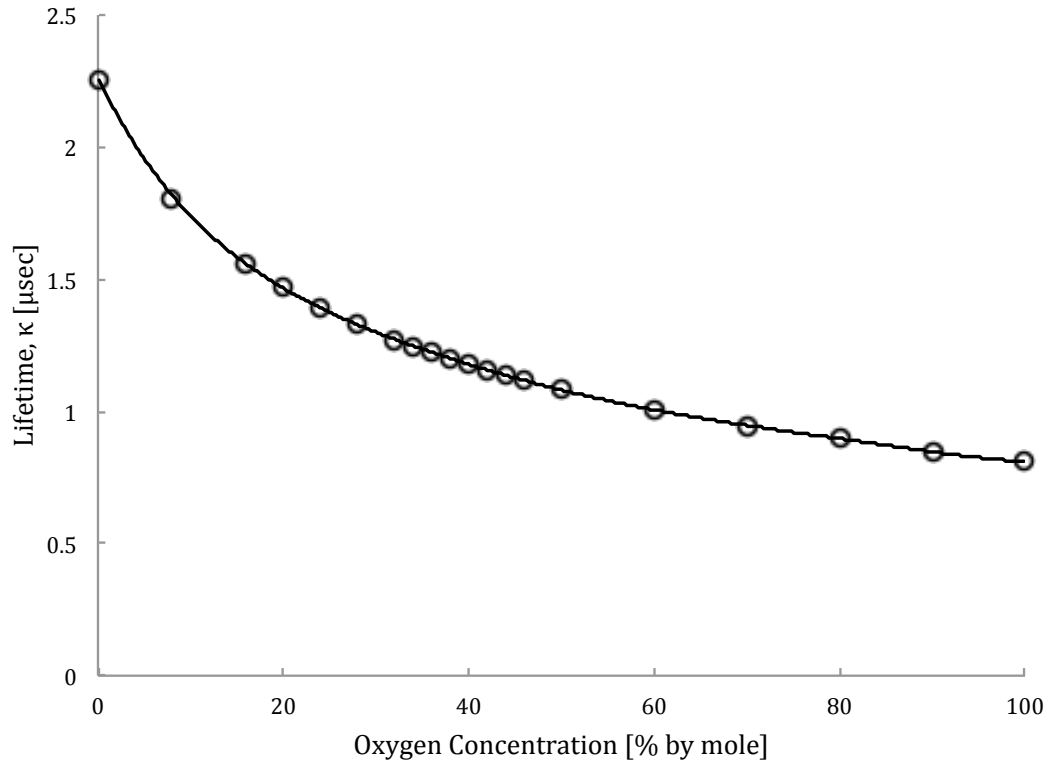
Figure 4.4: Typical calibration curve for oxygen sensor relating lifetime to oxygen concentration.

values recorded over time, leading to a decrease in measurement precision. By subtracting the slopes of the two data sets in Figure 4.5, the precision of the probe is found to decrease by $0.0008[\mu sec/day]$ during continuous operation of the oxygen sensor at the set duty cycle. More pragmatically, this corresponds to a decrease in measurement accuracy of 2.2% over the 40 day test period. It should be noted that the observed drift in κ cannot be attributed to drift in the mass flow controllers that feed gases into the cell during calibration. For the calibration points of 0% and 100% oxygen concentration in Figure 4.5, the gases do not require metering by the mass flow controllers since only one gas is flowing, not a mixture. When the 100% oxygen calibration point is being performed, the valve feeding oxygen into the cell is open and the valve feeding nitrogen is closed. The reverse is true for the 0%

oxygen calibration point.
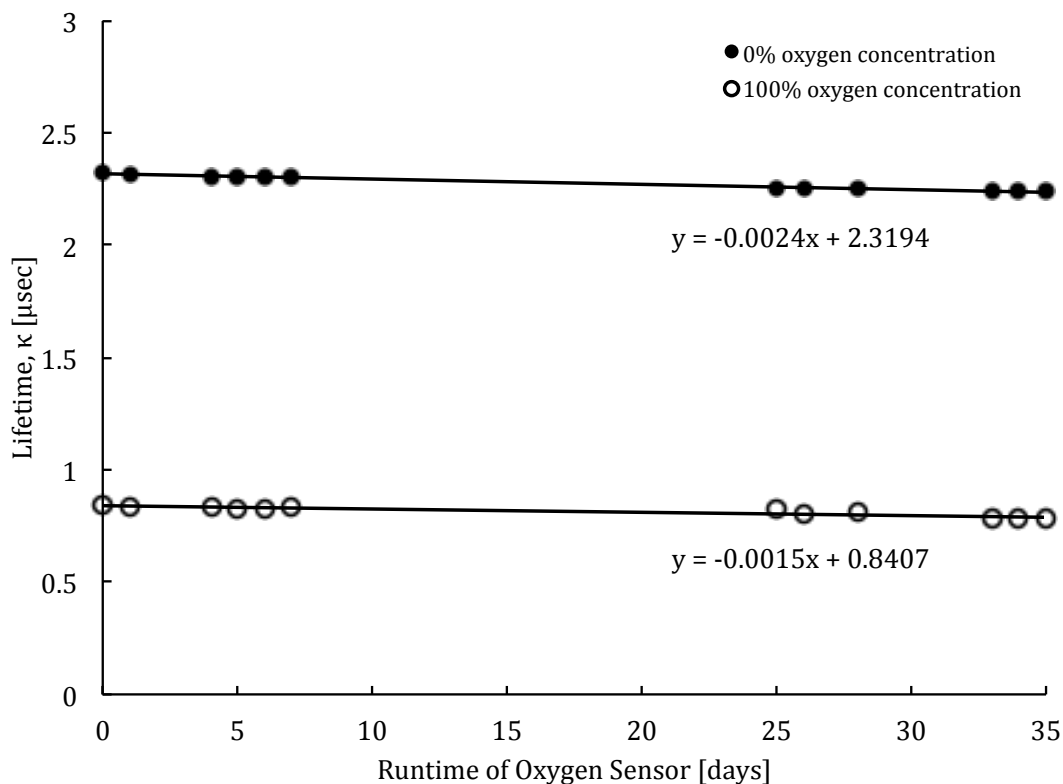
Figure 4.5: Loss of oxygen sensor accuracy due to sensor drift over time based on measured lifetime, κ, for calibrations performed at $50\,°C$.

4.2.4 Temperature

The temperature at which the diffusion experiment takes place is controlled by a temperature controlled water loop that circulates through passages machined adjacent to the gas column in the Loschmidt cell, depicted in Figure 4.6. A Thermo Scientific RTE-7 temperature bath maintains temperature stability to within $0.2\,°C$. Manifolds on the hot and cold side of the loop ensure even flow through each passage in the Loschmidt cell and thus an equal temperature distribution. A new oxygen sensor calibration is required for each

temperature set point, since the oxygen concentration measurement is sensitive to absolute temperature. Thermocouples located in the upper and lower gas chambers confirm gas temperature uniformity throughout the duration of a test. The maximum operating temperature of the probe is rated at $80\,°C$. Measurements were conducted over a range of temperatures (25, 50, and $70\,°C$) designed to simulate conditions that are typical of an operating PEM fuel cell.
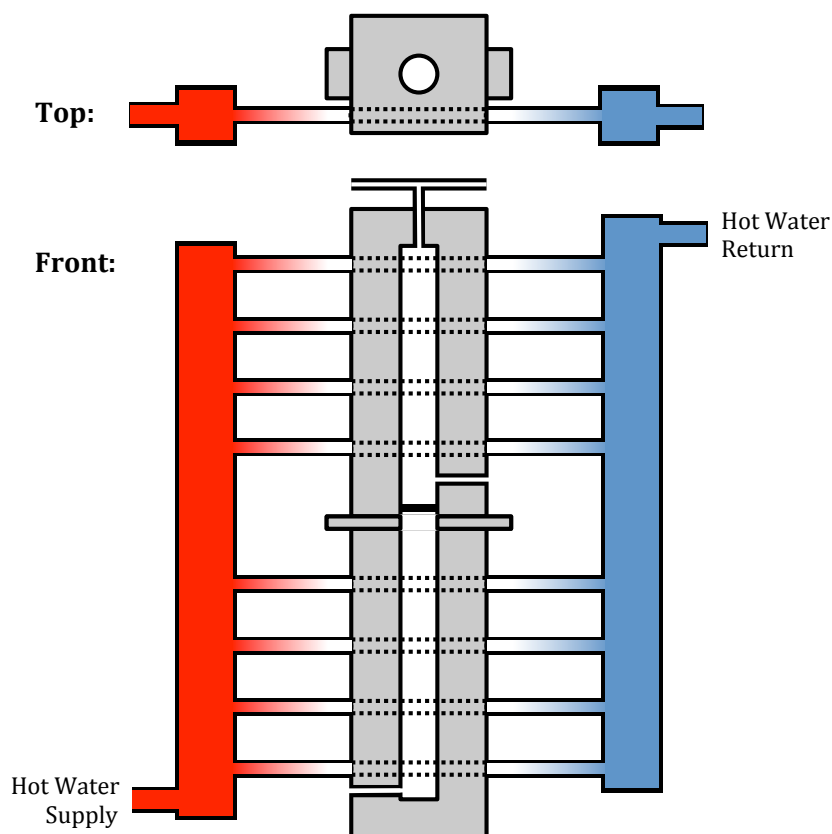
Figure 4.6: Schematic of temperature controlled water loop for the Loschmidt cell used in the present study.

4.2.5 Pressure

While it was originally proposed to operate the diffusion cell over a range of pressures, this proved to be infeasible with the present design. Operating the cell at a pressure differential above $0.5atm$ with the surrounding atmosphere resulted in a detectable leak that became more pronounced with greater pressures. The leak was attributed to the seals on the sliding gate (4.2), especially when they are in motion at the start of an experiment. Baranski et al. [88] addressed this issue by sealing the sliding gate mechanism to the rest of the cell, but encountered leakage between the top and bottom chambers instead. This design was not deemed to be of any significant improvement over the current apparatus. Instead, it was decided to operate the Loschmidt cell at atmospheric pressure to mitigate the impact of any leaks. Due to the sensitivity of the oxygen sensor to daily fluctuations in laboratory atmospheric pressure, the sensor was calibrated before each set of experiments. The resulting diffusion coefficient is a function of pressure and was normalized, in this case, to $1atm$. The relationship of the diffusion coefficient to pressure for an ideal gas is,

$$\frac{D_{ij\,P1}}{D_{ij\,P2}} = \frac{P_2}{P_1} \tag{4.7}$$

where $D_{ij\,P1}$ and $D_{ij\,P2}$ are the gaseous diffusion coefficients at pressures P_1 and P_2, respectively.

4.2.6 Data Analysis

Fick's Second Law for one-dimensional gas diffusion with constant diffusivity, as given in Eq. (2.4), can be solved for the Loschmidt cell using separation of variables and applying the following initial and boundary conditions:

$$\frac{\partial C}{\partial x}\bigg|_{\pm L/2} = 0 \tag{4.8}$$

$$C(-L/2 \leq x < 0, t = 0) = C_{o,b} \tag{4.9}$$

$$C(0 < x \leq L/2, t = 0) = C_{o,t} \tag{4.10}$$

40

where L is the total length of the Loschmidt cell, $C_{o,b}$ is the initial concentration in the bottom chamber, and $C_{o,t}$ is the initial concentration in the top chamber. An analytical solution for gas diffusion in the Loschmidt cell is obtained as follows [89],

$$C(x,t) = \frac{C_{o,b} + C_{o,t}}{2} - (C_{o,b} - C_{o,t})\frac{2}{\pi}\sum_{m=0}^{\infty}\frac{e^{-\left(\frac{\pi}{L}\right)^2(2m+1)^2 D_{ij}t}}{2m+1}\sin\frac{\pi x}{L}(2m+1) \qquad (4.11)$$

where C is the concentration at any location x and time t and D_{ij} is an estimate of the diffusion coefficient. The curve generated by the analytical solution, Eq. (4.11), using an initially assumed diffusivity is compared to the measured oxygen concentration as a function of time, such as the one shown in Figure 4.4. The difference is measured in terms of a root-mean-squared (RMS) error defined as,

$$RMS(D_{ij}) = \left(\frac{1}{p}\sum_{n=1}^{p}[\eta(x_p, t_n) - \eta_n]^2\right)^{1/2} \qquad (4.12)$$

where p is the total number of points considered (typically 500 in the present study), x_p is the location of the oxygen probe, t_n is the time of measurement n, and η_n is the concentration of measurement n. This expresses how well the assumed diffusion coefficient fits the data. An accurate estimate of the diffusion coefficient is found by applying the Newton-Raphson method to find successively better approximations for D_{ij}. Since the derivatives for RMS are not easily found, finite difference approximations for the first and second derivatives can be expressed as,

$$RMS'(D_{ij}) \approx \frac{RMS(D_{ij} + rD_{ij}) - RMS(D_{ij} - rD_{ij})}{2rD_{ij}} \qquad (4.13)$$

$$RMS''(D_{ij}) \approx \frac{RMS(D_{ij} + rD_{ij}) - 2RMS(D_{ij}) + RMS(D_{ij} - rD_{ij})}{(rD_{ij})^2} \qquad (4.14)$$

The ratio r is used rather than a constant ΔD so that the magnitude of the change for each step is related to the magnitude of D_{ij}. This ensures stability even with significant changes in order of magnitude. From Eqs. (4.13) and (4.14), the Newton-Raphson iteration $k+1$ with a relaxation term, ω, can be written as a function of the previous iteration k, such that,

$$D_{ij}^{k+1} \approx D_{ij}^k - (1 - \omega)\left[\frac{RMS'(D_{ij}^k)}{RMS''(D_{ij}^k)}\right] \qquad (4.15)$$

This process is executed in Matlab until solution convergence for the binary gas diffusion coefficient, D_{ij}, where the criterion for convergence is,

$$D_{ij}^{k+1} - D_{ij}^k \leq (0.1\%)D_{ij}^k \tag{4.16}$$

The error generated from Eq. (4.16) is deemed to have a negligible effect on D_{ij}, considering the experimental error that is discussed in the following section is one order of magnitude larger.

When a porous sample is inserted into the Loschmidt cell, Eq. (4.15) produces an equivalent diffusion coefficient, D_{ij}^{eq}, that represents the heterogeneous diffusion through the bulk gas and the sample. Following the procedure used in previous studies [37, 46, 47, 82, 84], the resistance network method may be applied between the oxygen probe (3) and sliding gate interface (5) in Figure 4.2 in order to solve for the effective diffusion coefficient of the porous sample. The equivalent diffusive resistance, R_{eq}, is the sum of the diffusive resistance through the binary gas, R_{binary}, and the sample, R_{eff},

$$R_{\mathrm{eq}} = R_{\mathrm{binary}} + R_{\mathrm{eff}} \tag{4.17}$$

or,

$$\frac{x_p}{D_{ij}^{\mathrm{eq}}} = \frac{x_p - l}{D_{ij}^{\mathrm{binary}}} + \frac{l}{D_{ij}^{\mathrm{eff}}} \tag{4.18}$$

where l is the thickness of the porous sample. The validity of solving for R_{eff} with the resistance network method has not been discussed in previous studies [37, 46, 47, 82, 84]. Dong *et al.* [85] demonstrates that the method is only accurate within a specific range of Fourier numbers,

$$Fo = \frac{D_{ij}t}{x_p{}^2} \tag{4.19}$$

where t is the characteristic time, or the length of time the experiment is run for (see Figure 4.3). The Fourier number can be controlled for a specific experiment by adjusting t.

4.2.7 Uncertainty Analysis

The diffusion coefficient, D_{ij}, is not measured directly by the experimental apparatus. Rather, D_{ij} is calculated from a set of measurements, X_N, as described earlier, such that,

$$D_{ij} = D_{ij}(X_1, X_2, \ldots, X_N) \tag{4.20}$$

A traditional method of calculating the uncertainty of D_{ij} is through a root-sum-square (RSS) method where each term is the partial derivative of D_{ij} with respect to X_n multiplied by the known uncertainty interval of X_n, or,

$$\delta D_{ij} = \left[\sum_{n=1}^{N} \left(\frac{\partial D_{ij}}{\partial X_n} \delta X_n \right)^2 \right]^{1/2} \tag{4.21}$$

However, D_{ij} is not easily differentiable considering the iterative nature of the solution described in Section 3. For such a case, Moffat [90] recommends a computerized uncertainty analysis where input variables are sequentially perturbed to generate an uncertainty contribution in D_{ij} for each variable. The overall uncertainty in the result is the RSS of these individual contributions.

Sources of uncertainty in the measurement apparatus that have a significant impact on the measured diffusion coefficient include the oxygen sensor and the oxygen and nitrogen mass flow controllers.

The manufacturer of the oxygen sensor quotes the uncertainty as less than 5% of reading for oxygen concentrations in the range of 0 to 20%. However, calculation of the diffusion coefficient is most sensitive to the measured oxygen concentrations from 20 to 40%. Without a clear measure of uncertainty from the manufacturer, the mass flow controllers feeding oxygen and nitrogen into the cell are used to evaluate the accuracy of the sensor. Based on repeated measurements, the oxygen sensor is found to have an error of less than 1% of full scale when the mass flow controllers supply a gas mixture with a known concentration of oxygen. The uncertainty of the oxygen sensor is taken as $\pm 1\%$ of full scale for the purposes of this analysis.

The performance of the oxygen sensor is dependent on its calibration at a specific temperature and pressure, and is also necessary to compensate for sensor drift over time.

Mass flow controllers flow oxygen and nitrogen past the oxygen sensor to calibrate it to a series of known concentrations. The manufacturer provides an uncertainty of $\pm 1.0\%$ of full scale for each mass flow controller.

Table 4.1 provides the results of a computerized uncertainty analysis that was performed on the two major sources of uncertainty previously described. An overall measurement equipment uncertainty in D_{ij}, or D_{ij}^{eq} when a sample is present in the cell, of 2.30% was found by calculating the RSS of the individual contributions to the uncertainty listed in Table 4.1.

Source of Uncertainty	Measurement Error [% of full scale]	Uncertainty in D_{ij} [%]
Oxygen sensor measurement	1.0	0.69
Mass flow controller measurement	1.0	2.2

Table 4.1: Sources of measurement equipment uncertainty in the experimental apparatus and their impact on the uncertainty of the calculated diffusion coefficient.

When using the resistance network method, the experimental uncertainty of the effective diffusion coefficient, D_{ij}^{eff}, is impacted by two sources of error: the measurement equipment uncertainty calculated above and the error due to the use of the resistance network approximation. Dong *et al.* [85] provides a more detailed analysis of the error associated with the use of a resistance network approximation and how it can be effectively eliminated for a well designed experiment.

The measurement equipment uncertainty in D_{ij}^{eff} due to the uncertainty in D_{ij}^{eq} can be expressed using Eq. (4.21), such that,

$$\delta D_{ij}^{\text{eff}} = \left| \frac{\partial D_{ij}^{\text{eff}}}{\partial D_{ij}^{\text{eq}}} \delta D_{ij}^{\text{eq}} \right| \tag{4.22}$$

where D_{ij}^{eff} is calculated from the resistance network in Eq. (4.18). Thus, measurement

equipment uncertainty in D_{ij}^{eff} is equal to,

$$\delta D_{ij}^{\text{eff}} = \left[l \frac{x_p}{(D_{ij}^{\text{eq}})^2} \left(\frac{x_p}{D_{ij}^{\text{eq}}} - \frac{x_p - l}{D_{ij}^{\text{binary}}} \right)^{-2} \right] \delta D_{ij}^{\text{eq}} \tag{4.23}$$

The effect of the measurement equipment uncertainty in D_{ij}^{eff} is strongly influenced by the geometry of the Loschmidt cell, namely the oxygen probe position, x_p, and thickness of the porous sample, l. The geometric sensitivity can be expressed in terms of a resistance ratio, $R_{\text{eff}}/R_{\text{binary}}$, which is the ratio of the resistance to diffusion between the sample and the binary gas. Figure 4.7 shows how the uncertainty due to the measurement equipment varies with the resistance ratio. For many thin materials used in fuel cells such as the gas diffusion layer, microporous layer, and catalyst layer, the resistance ratio can be controlled for a given experiment by stacking multiple samples on top of one another to change the thickness, l. For most practical experiments dealing with sub-millimetre thick samples, the resistance ratio falls in the range of 0 to 1 due to physical limitations in probe placement within the cell. Figure 4.7 shows that the measurement uncertainty is less than 10% when resistance ratio is maintained in this study above 0.5.

For comparison, the resistance ratio for the GDL diffusivity measurements performed by Zamel *et al.* [37] using a Loschmidt cell is on average 0.075 based on their reported dimensions. Figure 4.7 shows that this corresponds to a measurement uncertainty of about 30%. Using the same apparatus, PEMFC catalyst layer diffusivity measurements performed by Shen *et al.* [47] have a resistance ratio that is also about 0.075. However, the substrate that the catalyst layer is applied to results in an additional uncertainty term, which makes the calculation of overall uncertainty less straight forward. Using Eq. (4.21), the uncertainty was found to be about 60%. These large experimental uncertainties underscore the importance of controlling the resistance ratio in an experiment in order to achieve accurate measurements.

There are sources of error that have no way of being intentionally perturbed, nor their effect easily measured. The magnitude of some of these errors was calculated by Tordai [91] to show their negligible effect on the results. In other cases, the errors may be excluded from the calculation of uncertainty when the terms appearing in Eq. (4.21) are at least 3

45
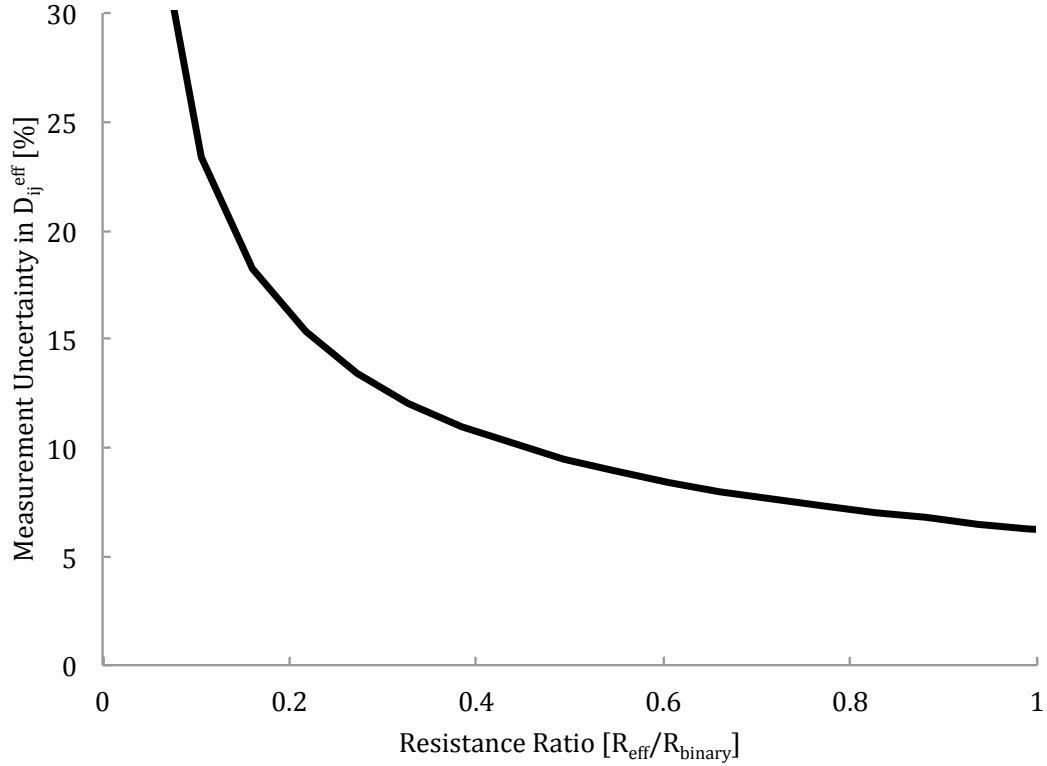
Figure 4.7: Measurement uncertainty for the effective diffusion coefficient, D_{ij}^{eff}, as a function of resistance ratio. In this study, uncertainty is less than 10% for a resistance ratio above 0.5.

times smaller than the largest term [90]. The nil effect of these terms is a result of applying the RSS method, which causes small terms to have very small effects. These sources of error include,

- An unequal volume of gas in the upper and lower chambers due to valve attachments. The number of valve attachments was reduced compared to the similar apparatus used in [37, 47, 81, 83].

- A small initial pressure difference between the gases in the upper and lower chambers can cause an initial mass flux at t = 0 that is not due to diffusion. Operating

the Loschmidt cell at atmospheric pressure and venting the chamber to atmosphere during chamber filling ensured that no pressure difference would be present.

- The oxygen concentration profile in the Loschmidt cell is assumed from an oxygen sensor measurement at a single stationary probe location. The accuracy of the probe location, x_p, is essential for predicting the correct oxygen concentration profile. Once the sensor's probe was mounted in the cell, a micrometer depth gauge was used to measure its location. The uncertainty in the distance from the mid-plane is estimated as $\pm 0.1 mm$. However, this measurement does not influence the overall uncertainty of D_{ij}^{eff} since the systematic error remains constant for both measurements of D_{ij}^{binary} and D_{ij}^{eq}. By applying Eq. (4.18) to solve for D_{ij}^{eff}, the systematic error in x_p is cancelled out.

- At the start of a measurement, the sliding gate spends several seconds in a partially open position during its opening movement. Tordai [91] showed that this event would generate a constant time error. Similarly, the oxygen sensor has a manufacturer reported response time of less than 1 second that generates a time error. These errors do not affect the shape of the oxygen concentration vs. time profile; they only shift it along the time axis. The precise start time of the experiment, t = 0, is found by extrapolating the oxygen concentration measured by the sensor vs. time data to the time when oxygen concentration equals zero in Figure 4.3. The stepper motor controller aids in the repeatability of this event.

- The opening movement of the sliding gate can introduce a perturbation in the fluid. This effect has been investigated and shown to be small [91]. Performing measurements with various gate opening speeds have confirmed this result.

- Errors due to convective mass flux have been minimized through apparatus design. The lighter gas, nitrogen, is placed in the upper chamber to prevent buoyancy effects from driving the flow. Similarly, the Loschmidt cell is mounted vertically, rather than horizontally, to prevent a 'spillage' convective flux where the heavier gas spills into the opposite chamber.

- The Loschmidt cell has been mounted on rubber dampers to minimize the effect of

vibrations on the experiment. High frequency vibrations can increase the rate that gases mix and influence the measurement of diffusive flux.

- Temperature gradients are eliminated through the manifold design discussed in Section 4.2.4. Thermocouples mounted in the upper and lower gas chambers confirm a negligible temperature difference.

- The absorption and desorption of gases in the sliding gate sealing o-rings and lubricant can dilute the concentration gradient. Experiments were performed to quantify the rate of adsorption and desorption, measured with the oxygen sensor. Measurement runtime was chosen to minimize this error, while still collecting enough data points to not compromise measurement accuracy.

4.3   Thermal Conductivity

For the measurement of the gas diffusion coefficient, the primary difficulty in designing an apparatus, and the main source of uncertainty, was the creation of a controlled concentration flux between the two diffusing gas species and measuring that flux. In contrast, it is simple to generate a heat flux in an apparatus that measures thermal conductivity. An electric heater can create a heat flux and two thermocouples can detect the flux, or temperature drop over a distance. The main source of error for thermal conductivity measurement instruments are the loss of heat radially. Insulating materials and placing the apparatus in a vacuum chamber can significantly reduce the radial heat loss, but never eliminate it.

4.3.1   Apparatus and Measurement Principle

The experimental apparatus used in the present study follows the steady-state guarded heat flow technique described in the ASTM standard D 5470-06 [92], and is an evolution of previous designs [93]. A similar experimental setup has been utilized by other researchers to measure effective thermal conductivity of GDLs [60, 63–66], and other materials [94].

The experimental method for this design strives to create a strictly 1-dimensional heat flow through a sample that can be measured with an adjacent heat flux measuring device, herein called a fluxmeter. The choice of fluxmeter material is critical for minimizing uncertainty in the results. It must have a thermal conductivity near that of the unknown material in order to maximize the temperature drop along the fluxmeter, while also having a calibrated thermal conductivity of sufficient accuracy to compute the heat flux [92]. Other requirements for the material are that it is durable, machinable, and can be subjected to high compressive forces during measurement. Electrolytic iron was found to best meet all of these criteria.

The apparatus is illustrated in Figure 4.8, where a sample is compressed between two calibrated electrolytic iron fluxmeters. A Velmex stepper motor attached to a vertical slide controls sample compression up to $15 bar$ and provides feedback of sample thickness at $1.2 \mu m$ per step. A Honeywell Sensotec load cell measures sample compression pressure. A temperature gradient is induced across the sample using an electric heater attached to the lower fluxmeter as a heat source, and a constant temperature bath attached to the upper fluxmeter as a heat sink. Heat transfer is limited to one dimension by insulating the two fluxmeters in the radial direction with the use of a vacuum chamber capable of achieving $10^0[Pa]$ absolute pressure. The low pressure environment practically eliminates convective heat flow, which is the primary source of heat loss at atmospheric pressure. Radiation losses from the hot-side fluxmeter are reduced with the use of a heated radiation shield, shown in Figure 4.8.

The upper and lower fluxmeters are initially set to touch each other without a sample in between, and the joint temperature is raised to the desired level. This warm-up period ensures that minimal thermal expansion in the apparatus components will occur once a sample is in place, which may otherwise affect thickness measurements. When the experiment is ready to begin, the stepper motor compresses the fluxmeters to a set of desired pressures and records position at each. Then, a sample is placed between the fluxmeter surfaces and compressed to the first compression pressure in the set. Once steady state is reached, compression pressure, stepper motor position, and thermocouple temperature data are recorded by the data acquisition system. Sample thickness is determined by subtracting the position of the stepper motor from the previously recorded position without

49
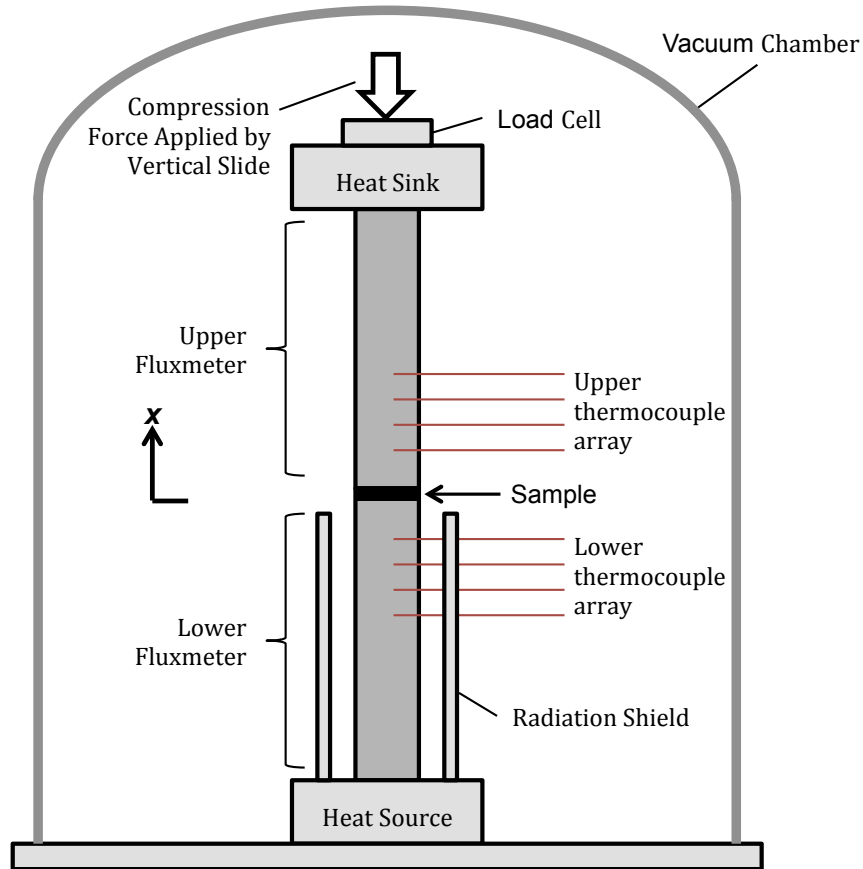
Figure 4.8: Experimental setup for thermal resistance measurement.

the sample in place. Heat flux and temperature drop across the sample are calculated from the thermocouple temperature data, as described in the previous sub-section. The stepper motor then compresses the sample to the next desired pressure and the measurement procedure is repeated.

4.3.2 Data Analysis

Thermocouples imbedded in the fluxmeters at a known spacing measure a linear temperature gradient dT/dx on the upper and lower thermocouple arrays. These values are averaged as a result of a minute amount of heat loss to the surroundings that is still present

50

despite the insulation and that causes a small disparity in readings between the upper and lower fluxmeters. The total heat flow rate through the GDL is determined by,

$$Q = k(T)A\frac{dT}{dx} \tag{4.24}$$

where $k(T)$ is the known thermal conductivity of the flux meters, A is the cross sectional area of the flux meters, and dT/dx is the temperature gradient determined as described earlier. The total thermal resistance of the GDL is,

$$R_t = \frac{\Delta T}{Q} \tag{4.25}$$

where ΔT is the extrapolated temperature drop across the GDL as shown in Figure 4.9, and Q is the total heat flow rate calculated in Eq. (4.24).

The measured thermal resistance R_t is the sum of the effective thermal resistance, R_{eff}, of the sample, and the total surface contact resistance, R_c, with the flux meters, or

$$R_{t,1} = R_{\text{eff}} + R_c \tag{4.26}$$

In order to solve for the effective thermal resistance, a second equation must be generated by rerunning the experiment with two GDL samples stacked together, such that,

$$R_{t,2} = 2R_{\text{eff}} + R_c \tag{4.27}$$

The contact resistance between the two GDL is assumed to be negligible. This assumption is critical in order to separate the contact resistance between the sample and the fluxmeter surface from the effective thermal resistance of the sample and has been proven valid by previous studies [60, 64]. The effective thermal conductivity of the sample can now be determined from the effective thermal resistance of the sample as follows:

$$k_{\text{eff}} = \frac{L}{R_{\text{eff}}A} \tag{4.28}$$
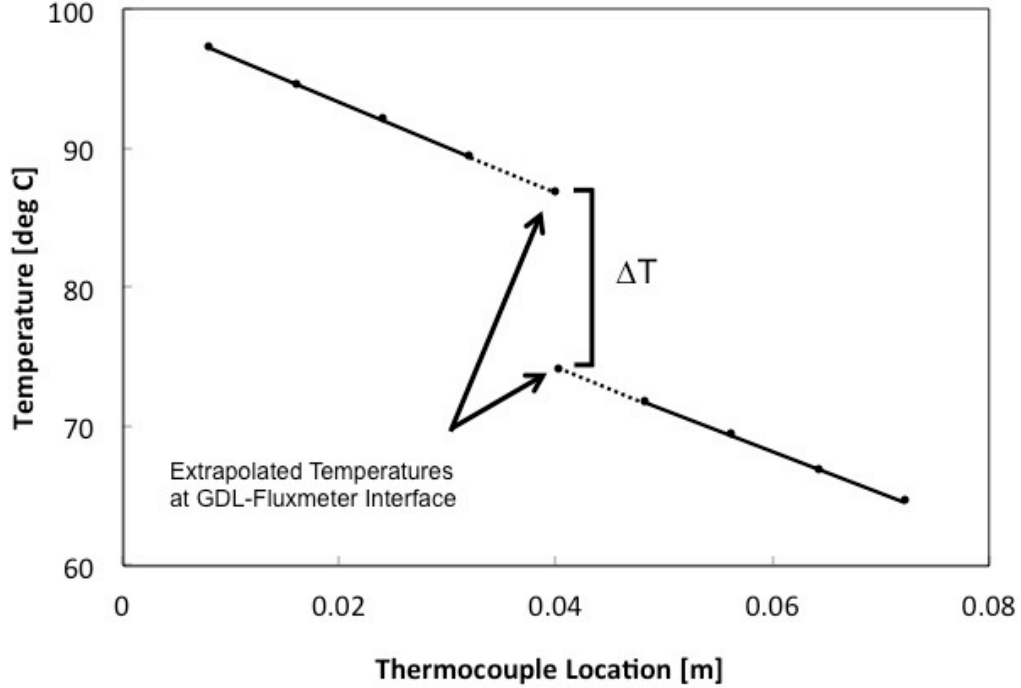
Figure 4.9: Typical temperature distribution within the fluxmeters.

where L is the thickness of the GDL, R_{eff} is the effective thermal resistance of the sample determined from solving Eqs. (4.26) and (4.27), and A is the surface area of the GDL.

The effective thermal conductivity of the MPL may be found by evaluating the thermal resistance network described in Figure 4.10 comprising of a GDL and MPL, such that

$$R_{\text{eff}}^{\text{GDLw/MPL}} = R_{\text{eff}}^{\text{GDL}} + R_{\text{eff}}^{\text{MPL}} \tag{4.29}$$

where $R_{\text{eff}}^{\text{GDLw/MPL}}$ and $R_{\text{eff}}^{\text{GDL}}$ are the effective thermal resistance of the sample with and without MPL, respectively. It also follows that,

$$L_{\text{GDLw/MPL}} = L_{\text{GDL}} + L_{\text{MPL}} \tag{4.30}$$

where $L_{\text{GDLw/MPL}}$ and L_{GDL} are the sample thickness with and without the MPL, respectively. Effective thermal conductivity of the MPL, k_{MPL}, is solved by substituting Eqs. (4.29) and (4.30) into Eq. (4.28), so that,

$$k_{\text{MPL}} = \frac{L_{\text{GDLw/MPL}} - L_{\text{GDL}}}{(R_{\text{eff}}^{\text{GDLw/MPL}} - R_{\text{eff}}^{\text{GDL}})A} \tag{4.31}$$

A fundamental assumption with this method is that both GDL samples with and without the MPL are made from the same carbon substrate.
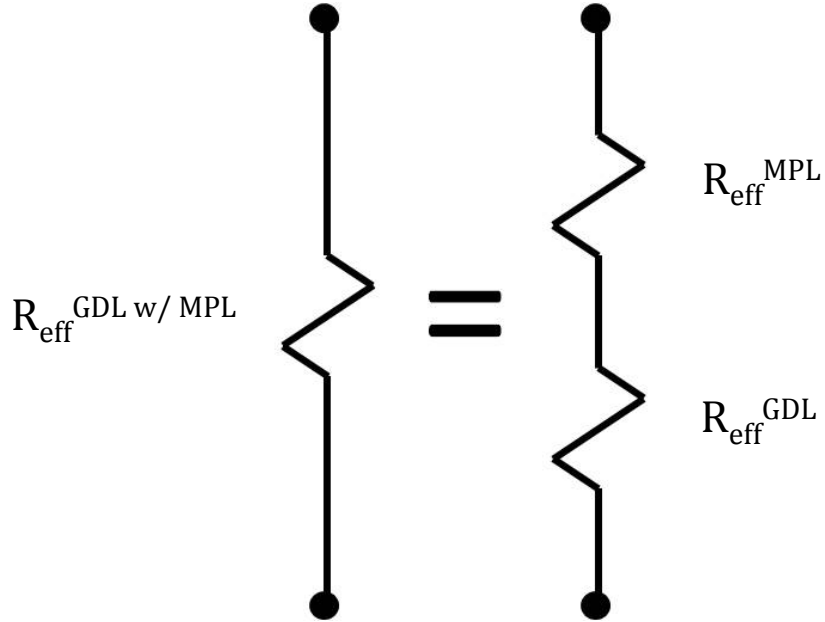
Figure 4.10: Thermal resistance network of a gas diffusion layer containing a microporous layer.

4.3.3 Uncertainty Analysis

An uncertainty analysis is performed similar to that for the Loschmidt method in Section 4.2.7 using the method described by Moffat [90]. By combining Eqs. (4.24) and (4.25), thermal resistance, R_t, is given by,

$$R_t = \frac{\Delta T_\mathrm{s}}{kA\frac{dT}{dx}} \tag{4.32}$$

where the uncertainty in R_t is calculated from the uncertainties of the temperature drop across the sample, ΔT_s, fluxmeter thermal conductivity, k, cross sectional area of the measurement chamber, A, and the temperature gradient of the fluxmeters, dT/dx. The temperature gradient is calculated from the measured values of temperature drop in the fluxmeter, ΔT_f and spacing of the thermocouple probes, x_f, such that,

$$\frac{dT}{dx} = \frac{\Delta T_\mathrm{f}}{x_\mathrm{f}} \tag{4.33}$$

then Eq. (4.32) can be written,

$$R_t = \frac{\Delta T_\mathrm{s}}{kA} \frac{x_\mathrm{f}}{\Delta T_\mathrm{f}} \tag{4.34}$$

The primary source of uncertainty in the calculated thermal resistance, R_t, is due to the radial heat loss from the fluxmeters to the environment, which impacts the measured temperature gradient, dT/dx, and temperature drop across the sample, ΔT. The difference in readings for dT/dx between the upper and lower fluxmeters, which operate at hotter and colder temperatures relative to the sample, provides an indication of the magnitude of this error. Since the mean of these two readings is used to calculate the thermal resistance, the uncertainty may be estimated as half of the percent difference from the mean. For a typical set of operating conditions, the uncertainty is

$$\frac{\delta dT/dx}{dT/dx} = \frac{1}{2}\frac{(dT/dx)_{Hot} - (dT/dx)_{Cold}}{(dT/dx)_{Avg}} = \frac{1}{2}\frac{(336.9 - 307.9)[^\circ K/W]}{322.4[^\circ K/W]} = \pm 0.04 \tag{4.35}$$

The uncertainty of dT/dx is further affected by spacing of the thermocouples, x_f, and the accuracy of the thermocouple readings, ΔT_f, in Eq. (4.34). The radius of the holes in the fluxmeters where the thermocouple junctions are located gives a good indication of the

relative magnitude of the uncertainty in the thermocouple spacing. Each fluxmeter has four evenly placed thermocouples spanning a distance of $24mm$, such that,

$$\frac{\delta x_{\mathrm{f}}}{x_{\mathrm{f}}} = \frac{0.25[mm]}{24[mm]} = \pm 0.01 \tag{4.36}$$

Temperature measurement is performed with K-Type thermocouples connected to a Keithley 2701 data acquisition system with an Omega Ice Point constant temperature reference junction. For a typical thermocouple of precision $\pm 0.02°K$ (note: absolute temperature accuracy is not important for a differential temperature measurement) and a typical fluxmeter temperature differential of $10°K$, the uncertainty will be,

$$\frac{\delta(\Delta T_{\mathrm{f}})}{(\Delta T_{\mathrm{f}})} = \frac{0.02[°K]}{10[°K]} = \pm 0.002 \tag{4.37}$$

The uncertainty in ΔT_s is based on the same uncertainties as dT/dx, since ΔT_s is calculated from the slope of dT/dx. To that extent, it is already accounted for earlier in this discussion. The uncertainty in ΔT_s is also affected by the precision of a thermocouple. For a typical temperature drop across a sample of $10°K$, the uncertainty will be,

$$\frac{\delta(\Delta T_s)}{(\Delta T_s)} = \frac{0.02[°K]}{10[°K]} = \pm 0.002 \tag{4.38}$$

The fluxmeters were machined from electrolytic iron that has been calibrated by the manufacturer to be within a tolerance of $0.1W/m°K$. For a typical location along the fluxmeter bar, the error is,

$$\frac{\delta k}{k} = \frac{0.1[W/m°K]}{67.7[W/m°K]} = \pm 0.001 \tag{4.39}$$

The uncertainty in the cross sectional area, A, does not need to be considered if it remains constant for the fluxmeters and sample, since it will cancel out (see Section 4.3.2). However, the circular samples that are cut with a punch may not have an identical diameter to that of the fluxmeters. Also, the alignment of the sample with the fluxmeters is done by eye to an estimated uncertainty of $\pm 0.25mm$ of the sample diameter, and,

$$\frac{\delta A}{A} = \frac{(19.30^2 - 18.80^2)[mm^2]}{19.05^2[mm^2]} = \pm 0.02 \tag{4.40}$$

These sources of error, summarized in Table 4.2, may be combined into a simplified form of Eq. (4.21), so that,

$$\frac{\delta R_t}{R_t} = \left[\left(\frac{\delta(dT/dx)}{(dT/dx)} \right)^2 + \left(\frac{\delta x_f}{x_f} \right)^2 + \left(\frac{\delta(\Delta T_f)}{(\Delta T_f)} \right)^2 + \left(\frac{\delta(\Delta T_s)}{(\Delta T_s)} \right)^2 + \left(\frac{\delta k}{k} \right)^2 + \left(\frac{\delta S}{S} \right)^2 \right]^{1/2}$$

(4.41)

and the overall uncertainty in the measured thermal resistance is 4.6%.

Location	Source	Symbol	Uncertainty [%]
Fluxmeter	Heat Loss to Environment	dT/dx	4.0
	Thermocouple Spacing	x_f	1.0
	Temperature Differential	T_f	0.2
	Thermal conductivity	k	0.1
Sample	Cross Sectional Area	A	2.0
	Temperature Differential	T_s	0.2

Table 4.2: Sources of measurement uncertainty for a typical guarded heat flow experiment.

The measurement uncertainty in the effective thermal resistance of the sample, R_{eff}, due to the uncertainty in the measured thermal resistance, R_t, can be expressed using Eq. (4.21), such that,

$$\delta R_{\text{eff}} = \left| \frac{\partial R_{\text{eff}}}{\partial R_t} \delta R_t \right|$$

(4.42)

Similar to the Loschmidt method, a resistance ratio equal to R_{eff}/R_c can be used to understand the sensitivity of these two values on the uncertainty in R_{eff}. Figure 4.11 shows how the uncertainty of the effective thermal resistance varies with the resistance ratio using Eq. (4.42). For a typical experiment, the resistance ratio was approximately 2 and the uncertainty in R_{eff} was 6.9%. In general, an experiment should be designed to have a resistance ratio that is greater than 1.5 to avoid excessive error. This can be achieved by stacking multiple samples together, which increases R_{eff} but has no effect on R_c.

For many PEMFC materials being tested under a variety of temperatures and compression pressures, resistance ratio will be greater than 1.5 without needing to stack samples
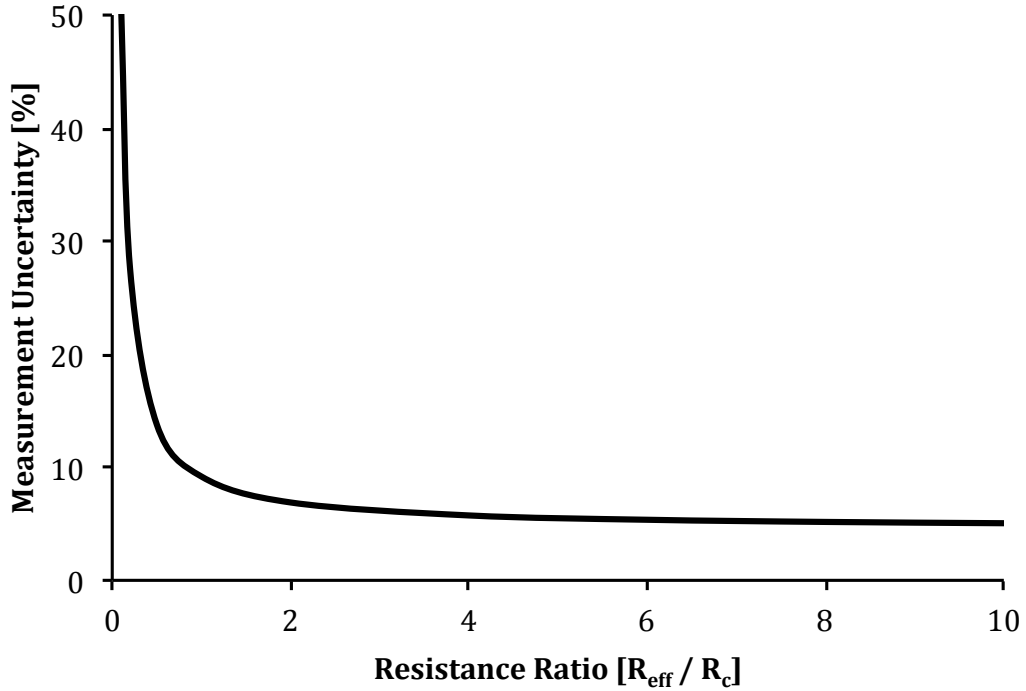
Figure 4.11: Measurement uncertainty for the effective thermal resistance, R_{eff}, as a function of resistance ratio.

together. However, experiments are at risk of having a resistance ratio below 1.5 when the samples are very thin or when the samples are tested at low compression pressures.

The uncertainty in the thermal conductivity, k_{eff} was calculated from the uncertainty in the effective thermal resistance, R_{eff}, and the measured sample thickness, L. A VXM stepper motor attached to a vertical slide has an uncertainty of $\pm 1.5 \mu m$. For a typical sample,

$$\frac{\delta T}{T} = \frac{1.5[\mu m]}{200[\mu m]} = \pm 0.0075 \tag{4.43}$$

which does not have a meaningful impact on the uncertainty when combined with the uncertainty in R_{eff}. As a result, the average uncertainty in the thermal conductivity of the samples tested in this study was calculated to be 6.9%. An uncertainty of 9.4% was

found for the worst case scenario occurring at low compression pressures ($\approx 4bar$) for the set of GDL that were tested in this thesis. The uncertainty is reduced as the compression pressure is increased.

4.4   Reducing Experimental Uncertainty

Sources of experimental uncertainty found in the Loschmidt and guarded heat flow methods that have been discussed in Sections 4.2.7 and 4.3.3, are rooted in similar challenges for controlling and measuring physical phenomena. These sources of uncertainty, and ways to reduce them, are discussed in the following section for both experimental methods.

4.4.1   Stacking Samples

For both measurement apparatuses, a resistance network is applied to solve for the sample resistance, R_{s}, of the form,

$$R_{\mathrm{m}} = R_{\mathrm{s}} + R_{\mathrm{const}} \tag{4.44}$$

where R_{m} is some resistance determined by experimental measurements with inherent uncertainty, $\delta R_{\mathrm{m}}/R_{\mathrm{m}}$, and R_{const} is some constant resistance that does not change within a set of experiments. Uncertainty in R_{s}, $\delta R_{\mathrm{s}}/R_{\mathrm{s}}$, is calculated from the uncertainty of R_{m}, and thus must always be equal to or greater than the uncertainty of R_{m}, or,

$$\frac{\delta R_{\mathrm{m}}}{R_{\mathrm{m}}} \leq \frac{\delta R_{\mathrm{s}}}{R_{\mathrm{s}}} \leq \infty \tag{4.45}$$

Maximizing the magnitude of R_{s} relative to R_{const} ensures that the uncertainty in R_{m} is as small as possible. This can be accomplished by stacking samples to increase the thickness.

The limitation with stacking samples is that the interfacial transport resistance must be negligible between samples, otherwise the additional unknown variable makes the system of equations unsolvable. Sample-to-sample resistance is not a concern for effective gas diffusion measurements since the conducting medium, a gas, is continuous regardless of the type of samples that are stacked. In contrast, the thermal resistance between solids

can be significant, as was discussed in Section 2.3.1. Fortunately, a number of studies have demonstrated that contact resistance between identical samples is negligible due to the compressible nature of GDLs and MPLs [60, 64].

4.4.2   Increasing Characteristic Length

In the Loschmidt method, measurement error caused by gas leaks, diffusion near walls, and uneven upper and lower chamber volumes caused by valve attachments, can be reduced by minimizing the amount of surface area relative to volume of the measurement chamber. Similarly, measurement error in the guarded heat flow method caused by heat loss from the surface of the flux meters to the surroundings can be minimized per unit volume in a similar manner. Thus, the characteristic length, L_c, of an apparatus can be defined as the ratio of volume, V, to surface area, A_s, of the measurement chamber. For both apparatuses, the measurement chamber is cylindrical, so that,

$$L_c = \frac{V}{A_s} = \frac{\pi r^2 h}{2\pi r h} = \frac{r}{2} \tag{4.46}$$

where increasing radius causes the volume to increase at a faster rate than the surface area. As a result, the radius of the measurement chamber should be made as large as is feasible in order to minimize surface area for a given measurement volume. Eq. (4.46) can also be applied to other shapes such as a rectangular cross section of side length, r, where the characteristic length equals $r/4$. A cylindrical chamber has half as much surface area compared to a rectangular chamber per unit volume. This demonstrates that a cylindrical measurement chamber is best for minimizing surface area.

In addition, increasing the radius of the measurement chamber of the guarded heat flow method reduces the uncertainty in the cross sectional area of the sample. The sample is cut using a punch and then manually aligned between the two fluxmeters. The variability in this procedure is estimated as a constant $\pm 0.5 mm$ of the diameter. As a result, increasing the radius of the measurement chamber, and hence the sample, reduces the impact that the sample alignment has on the uncertainty of the cross sectional area.

Although minimizing these sources of uncertainty favours an infinite radius, in practise the radius of a measurement chamber is limited by cost, manufacturability, and the physical

space available within a laboratory. These limitations imply a maximum radius of around $50 - 75mm$ For some experimental apparatuses, there may also be a radius where surface area based losses are not a dominant source of measurement uncertainty. In this case, it would be unnecessary to design an apparatus with a radius that is any larger.

Chapter 5

Characterization Results

5.1   GDL Gas Diffusivity

5.1.1   Test Samples

The properties of the GDL used in this study are summarized in Table 5.1. Thickness was determined by taking the average micrometer readings of 3 samples measured at 5 locations per sample. Porosity was determined from an average of 3 samples each measured once using the Method of Standard Porosimetry (MSP) technique (Porotech, Toronto, ON). Thickness and porosity measurements were found to be within 3% of the manufacturer's specifications for Toray GDL [95]. SolviCore did not provide similar information.

The GDLs were selected so that thickness (Toray TGP-H-60 and TGP-H-120) and manufacturer (Toray and SolviCore) variations could be compared. Although treating GDL with a hydrophobic agent such as PTFE is typical in commercial PEMFCs, raw GDLs were intentionally chosen to simplify the study between pore structure and gaseous diffusion.

Each of the three samples of each type of GDL are measured three times. Each measurement is an average of 20 experimental runs performed consecutively with the same calibration. In order to observe the effects of temperature, these tests were repeated over

	Thickness	Porosity
	[μm]	
Toray TGP-H-060	196	0.785
Toray TGP-H-120	364	0.769
SolviCore Type A	194	0.844

Table 5.1: Properties of Toray and SolviCore gas diffusion layers used in the present study.

three temperatures of 25, 50, and 70°C. Binary gas diffusion measurements were performed in a similar manner.

5.1.2 Effect of Temperature

The effect of temperature on nitrogen-oxygen diffusion has been extensively measured in literature [13, 22]. Figure 5.1 presents the binary gas diffusion measurements from this study with error bars that show the experimental uncertainty calculated in Chapter 4. The measurements agree well with those in literature and fall within the uncertainty limits described in each. This agreement helps to validate the results presented in this study.

The GDL is comprised of graphitized carbon fibres that are dimensionally stable within the temperature range evaluated in this study. Thus, it is expected that diffusibility will not change with temperature. The measured through-plane GDL diffusibility is summarized in Table 5.2 for different temperatures. Diffusibility increases slightly with temperature, however, the increase is within the bounds of experimental error. This is in agreement with the experimental results of Zamel *et al.* [37]. An average diffusibility is provided in Table 5.2 as a best estimate of diffusibility.

5.1.3 Comparison to Existing Literature

Several research groups have measured the diffusibility of untreated Toray GDL using the techniques of limiting current, water evapouration, electrochemical diffusimetry, and the
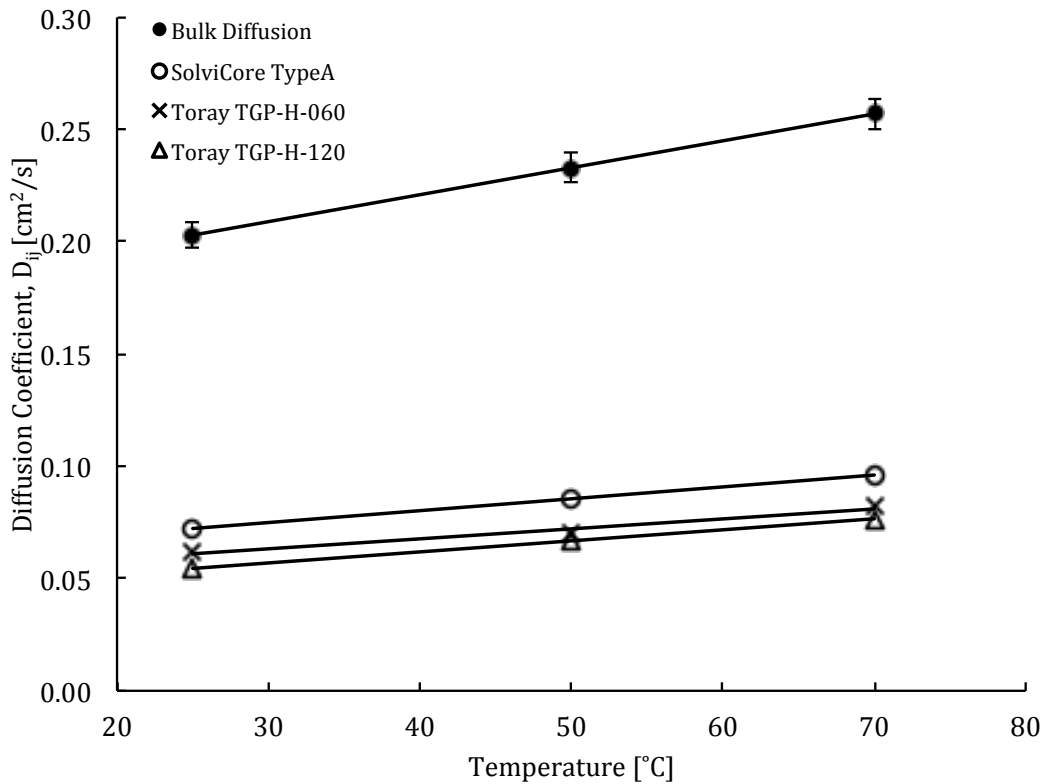
Figure 5.1: Binary gas diffusion coefficient and effective diffusion coefficient of gas diffusion layers measured at various temperatures using the Loschmidt cell developed in this study.

Loschmidt cell [36, 37, 39–41, 44]. It is a useful exercise to compare the results from these studies to determine whether they are in agreement. Figure 5.2 presents the measured diffusibility of various Toray GDL (-030, -060, -090, and -120 series) reported in literature as a function of the temperature they were measured at. Using the average of each research group's measurements, the average diffusibility for Toray GDL in literature is 0.317 at no compression. The results of the present study agree well with others.

Temperature [$°C$]	Diffusibility [$D_{ij}^{\text{eff}}/D_{ij}^{\text{binary}}$]		
	Toray TGP-H-060	Toray TGP-H-120	SolviCore TypeA
25	0.324	0.284	0.377
50	0.317	0.303	0.389
70	0.339	0.316	0.396
Average	0.327	0.301	0.387

Table 5.2: Diffusibility of Toray and SolviCore gas diffusion layers measured at various temperatures.

5.1.4 Effect of GDL Microstructure

GDL Thickness

A common assumption in current literature is that GDLs within the same series (i.e. Toray GDL -030, -060, -090, and -120 series) have a uniform microstructure that is independent of manufactured thickness. In general, this assumption is made so that the thickness of a GDL can be varied within an experiment. The diffusibility of Toray TGP-H-060 and TGP-H-120 have not been measured with the same experimental apparatus. For example, Kramer *et al.* [36] measured the diffusibility of only TGP-H-060 and Zamel *et al.* [37] measured the diffusibility of only TGP-H-120. Between the two experimental techniques, measurement uncertainty is too large to directly compare the diffusibility. This is further evidenced in Figure 5.2, which shows a wide range of measured values for Toray GDL.

The diffusibility of Toray TGP-H-060 and TGP-H-120 differ by 8% in Table 5.2, which suggests that the microstructure of the two Toray GDLs are not the same. This result is supported by differences in porosity recorded in Table 5.1. Fishman *et al.* [96, 97] used high resolution computed tomography to show that TGP-H-060 and TGP-H-120 have a heterogeneous through-plane porosity distribution. TGP-H-060 exhibited a higher porosity in the core region of the GDL, and a lower porosity near the edges. Interestingly, TGP-H-120 had a through-plane porosity distribution that resembles two TGP-H-060 GDL
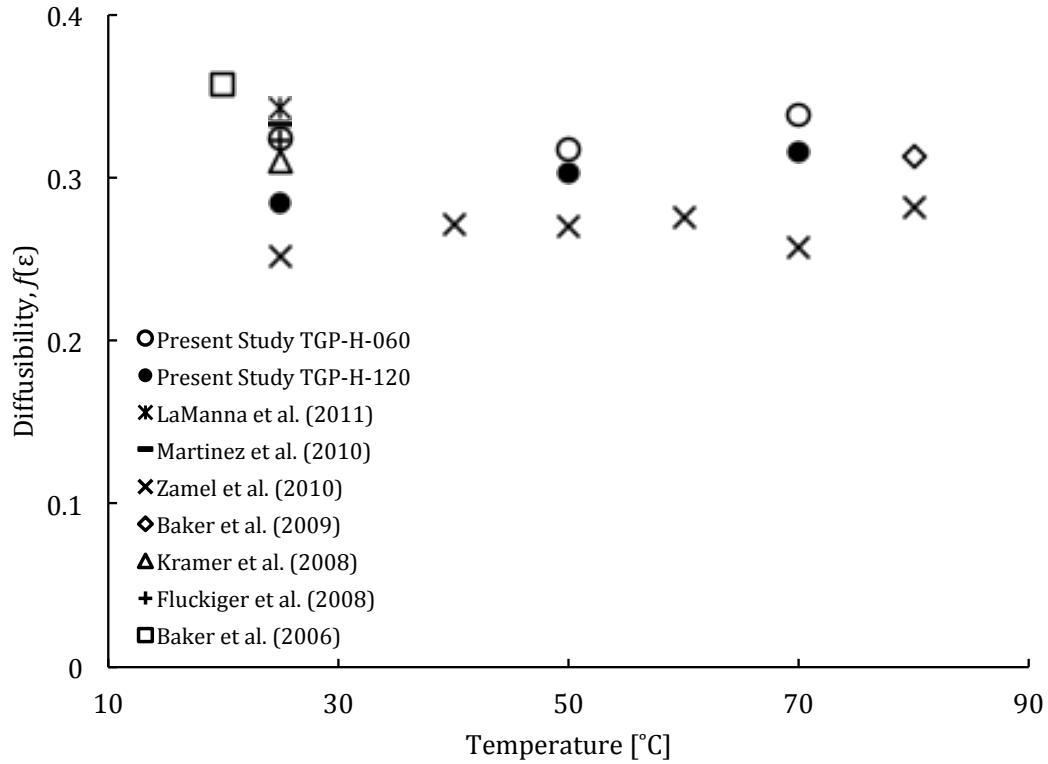
Figure 5.2: Diffusibility of Toray Gas Diffusion Layer experimentally determined by various studies over a range of temperatures with no (or minimum) compression force applied.

stacked together. This suggests that thicker Toray GDLs are manufactured by compressing multiple plies together [20, 98]. Similarly, TGP-H-090 is believed to be comprised of three layers of TGP-H-030 [99].

The heterogeneous porosity distributions of Fishman *et al.* [96, 97] agree well with the pore size distributions in Figure 5.3 for Toray TGP-H-060 and TGP-H-120. Pore size in these GDLs fall into two distinct groups around $12 - 17 \mu m$ and $18 - 24 \mu m$, corresponding to near surface and core regions of the GDL, respectively.

Figure 5.3 and knowledge of the manufacturing differences between Toray TGP-H-060 and TGP-H-120 can help to explain why TGP-H-120 has a lower diffusibility than TGP-H-060. The force applied to the TGP-H-120 in order to mold the plies together reduces the
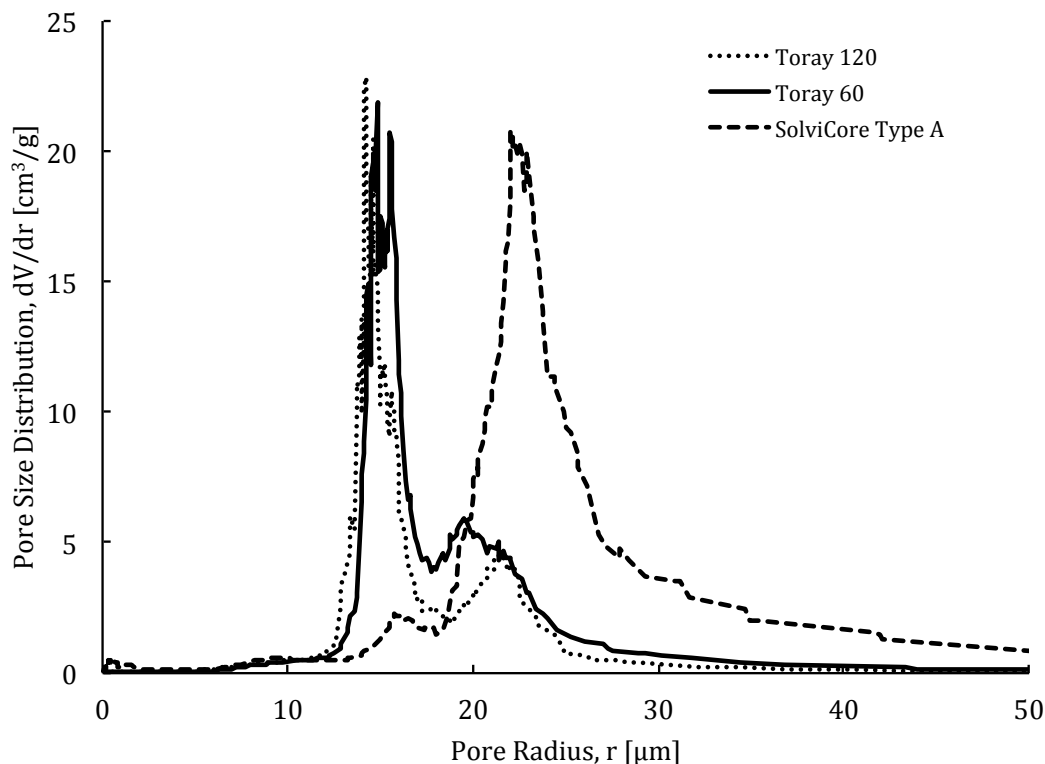
Figure 5.3: Pore size distributions of gas diffusion layers found by method of standard porosimetry.

porosity of the subsequent GDL. Figure 5.3 shows that the TGP-H-120 has fewer pores in the $18 - 24\mu m$ range than the TGP-H-060. Large pores, corresponding to a large distance between fibres, are the mechanically weakest part of the GDL. As a result, compression force will have the largest effect on these large pores as Figure 5.3 demonstrates.

These results are significant for studies that assume uniformity between different manufactured thicknesses in order to infer aspects on how a PEM fuel cell operates. Caution should be used when small property variations, such as an 8% difference in diffusibility, between Toray TGP-H-060 and TGP-H-120 could impact the accuracy of the measurements. In literature, thermophysical property measurements are commonly expressed or implied to have uncertainties of less than 8%.

GDL Manufacturer

This study is the first to the authors' knowledge to measure the diffusibility of SolviCore Type A GDL, provided in Table 5.2. The most appropriate comparison to the diffusibility of SolviCore can be made with Toray TGP-H-060, of which both are near identical thickness. Diffusibility of the SolviCore GDL is approximately 20% greater than Toray TGP-H-060. This result can be attributed to the porosity and pore size distribution of the respective GDL. The porosity of the SolviCore GDL is approximately 8% greater than the TGP-H-060. While pore size ranges from $13 - 30\mu m$ for the TGP-H-060 GDL, pore size for the SolviCore GDL have a much larger range of $13 - 50\mu m$.

In-plane scanning electron microscope (SEM) images of SolviCore and Toray GDLs are presented in Figures 5.4 and 5.5, respectively. The primary microstructure differences between the two GDLs are in the fibre arrangement and the distribution of binder between the fibres.

fibres in the Toray GDL are tightly stacked on top of one another in the through-plane direction. The inlay in Figure 5.5 shows at least 8 fibres stacked above one another. Considering these 8 overlapping fibres are all within the depth of focus of the camera, this suggests that they are in close proximity to one another. In contrast, the fibres of the SolviCore GDL are more spread out in the through-plane direction. The inlay in Figure 5.4 shows only 2 overlapping fibres within the depth of focus of the camera, with a third fibre out of focus in the background. This suggests that there is a mat of fibres in the foreground and another in the distance, separated by a large void space, or pore.

There is significantly more binder per fibre visible in the SolviCore GDL than the Toray GDL in Figures 5.4 and 5.5. The binder in the Toray GDL forms smooth skins between the fibres, distinctly different from the coarse particles of the SolviCore GDL binder. Kramer *et al.* [36] notes that the skins are preferentially oriented in the in-plane direction. The binder distribution of the SolviCore resembles clumps around the fibres without being preferentially oriented in any direction.
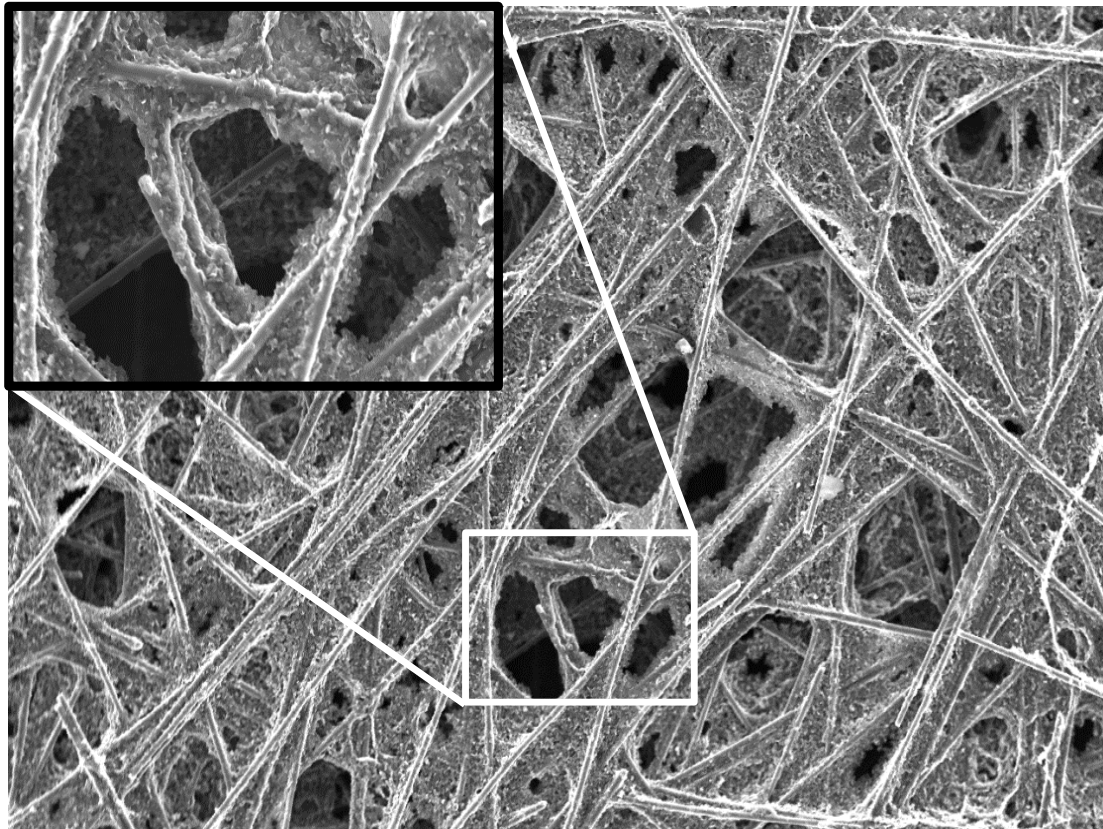
Figure 5.4: In-plane scanning electron microscope image of SolviCore Type A gas diffusion layer at 100x magnification. Inlay shows enlarged region of interest.

5.1.5 Limitations of Current Geometric Models

It has been well demonstrated in current literature that relevant correlations based on porosity significantly over predict the through-plane diffusibility of carbon papers [30, 36–38, 44]. The primary shortfall with these correlations is that they do not take into account the amount and distribution of binder on the fibres. In fact, correlations agree very well with experimental data for carbon cloths [38], which do not contain any binder material.

Including an additional parameter in a geometric model that considers the amount of binder present could provide better agreement between geometric models and experimental data. Figures 5.4 and 5.5 show that binder has a significant impact on the shape, orienta-
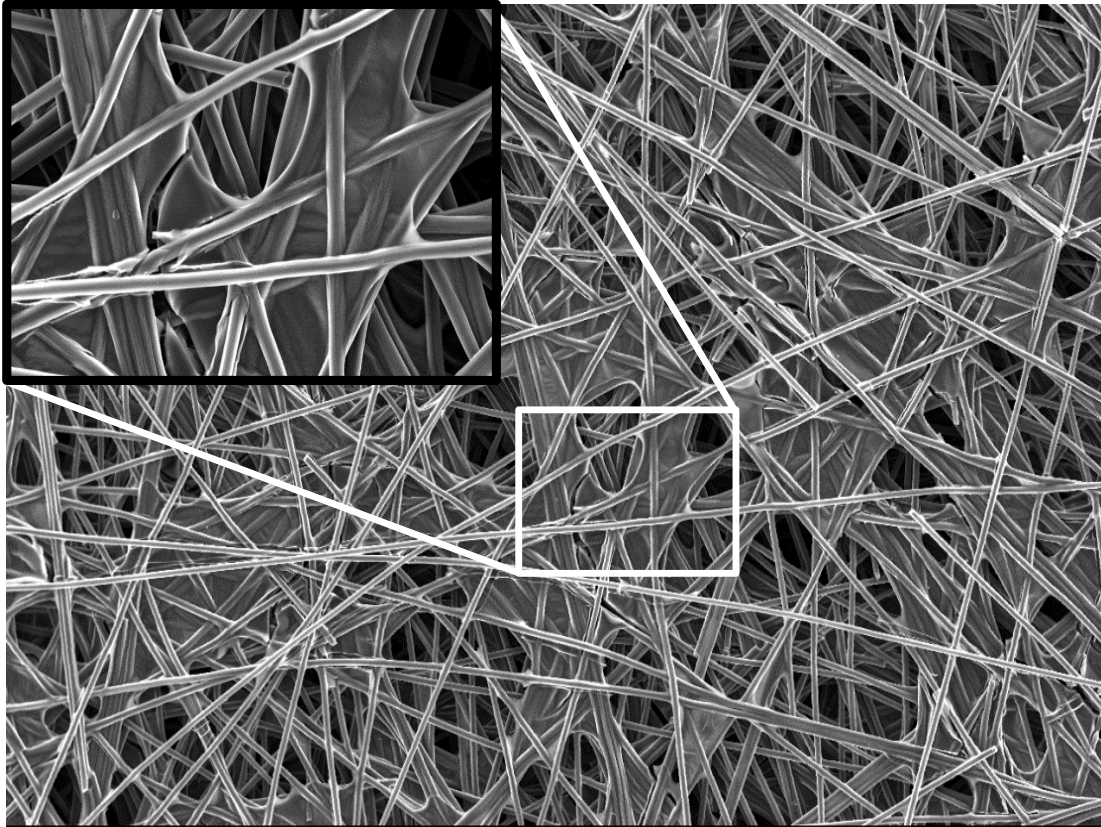
Figure 5.5: In-plane scanning electron microscope image of Toray TGP-H-060 gas diffusion layer at 100x magnification. Inlay shows enlarged region of interest.

tion, and effective length of pores based on the amount and distribution of binder on the fibres. As such, the tortuosity parameter, τ, in a geometric model should be a function of the binder content. However, tortuosity cannot be determined by straight forward means making the influence of the binder difficult to quantify.

Correlations developed from experimental data alleviate the difficulties in quantifying the influence of the binder on diffusibility, since the experimental measurements inherently include them. Zamel *et al.* [30] developed a correlation for the diffusibility of Toray GDL as a function of porosity using a geometric model that was validated using experimental data. However, their model is not necessarily applicable to other brands of GDL since the

distribution of binder varies significantly from one brand of GDL to another (Figures 5.4 and 5.5). At the time of publication, experimental data for other GDL brands was not available.

5.1.6 Modified Correlation Using Experimental Data

Figure 5.6 provides diffusibility measurements for GDL with less than 10% PTFE content from several studies as a function of porosity, presented together for comparison. The inlaid graph provides an enlarged region of the data for clarity. The data shows a distinct trend despite have a relatively large spread, which is attributed to the high measurement uncertainty in the respective studies, and the variations in microstructure amongst GDL manufacturers.

Using the correlation developed by Das *et al.* [28] and the geometric factor developed by Zamel *et al.* [30], a new set of correlation parameters is found using the experimental data in Figure 5.6. Table 5.3 presents the correlation parameters generated from a least-squares fit with an R^2 value of 0.933, compared to the values used by Zamel *et al.* [30] that results in an R^2 value of 0.887 for this set of experimental data. Thus, the modified correlation for the through-plane GDL diffusibility as a function of porosity is,

$$f(\epsilon) = \left(1 - (2.72\epsilon)\cosh(2.53\epsilon - 1.61)\left(\frac{3(1-\epsilon)}{3-\epsilon}\right)\right) \tag{5.1}$$

Eq. (5.1) is shown in Figure 5.6, along with the original correlation proposed by Zamel *et al.* [30]. While the original correlation gives a reasonable estimate of diffusibility for porosities between 0.6 and 0.9, below this range it deviates greatly.

Eq. (5.1) provides the best estimate to date of diffusibility as a function of porosity for all GDLs with less than 10%-wt. PTFE. A precise correlation may not be feasible to describe the through-plane diffusion in all GDL carbon papers due to the diversity in microstructure present amongst different GDL manufacturers. However, future studies may benefit from this work for estimating GDL diffusibility in fuel cell models where precise experimental data does not exist. The experimental methods developed in this work, particularly with regards to measurement uncertainty, should lead to more accurate
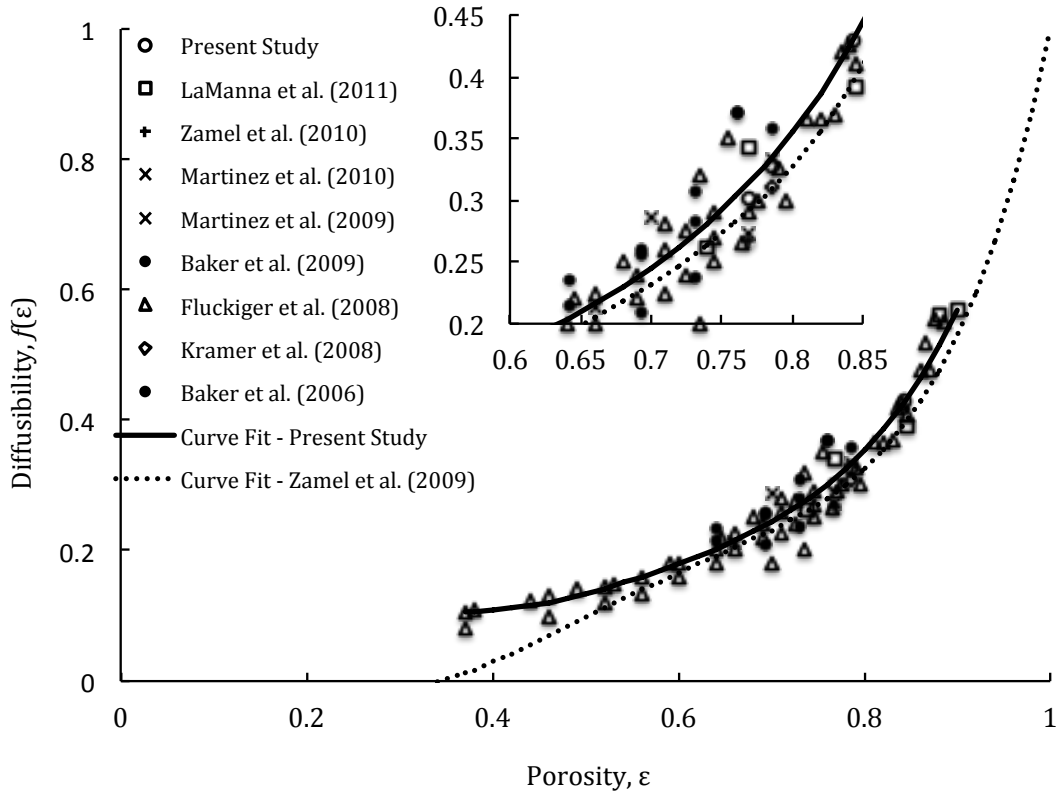
Figure 5.6: Diffusibility of gas diffusion layers with less than 10%-wt. PTFE content as a function of porosity that have been reported in literature.

	A	B	C	validity range	R^2
Zamel et al. (2009)	2.76	3.00	1.92	$0.33 \leq \epsilon \leq 1.0$	0.887
Present Study	2.72	2.53	1.61	$0.37 \leq \epsilon \leq 0.9$	0.933

Table 5.3: Correlation parameters for Eq. (5.1) that predict the through-plane diffusibility of gas diffusion layers with less than 10%-wt. PTFE content.

diffusibility measurements for GDL, as well as measurements on the diffusibility of the microporous layer and catalyst layer of PEMFCs for which there is limited data.

5.2 GDL and MPL Thermal Conductivity

5.2.1 Test Samples

This study considers two SolviCore brand GDL that might be considered for the same fuel cell application. While one contains a MPL and the other does not, both contain 5% PTFE $\% - wt.$ in the GDL substrate, and are of similar thickness. Table 5.4 summarizes the specifications provided by the manufacturer. The samples are measured at a mean temperature of $80\,^{\circ}$C while being subjected to a range of compression pressures from 4 to $15bar$.

	SolviCore Type A	
	without MPL	with MPL
Thickness [μm]	200	240
PTFE Content Substrate [%-wt.]	5	5
PTFE Content MPL [%-wt.]		30

Table 5.4: Manufacturer reported properties of SolviCore gas diffusion layer used in the present study.

For the results presented in this section, the data points are an average of 10 repeated measurements. Since the compression of the sample can introduce hysteresis in the sample thickness as discussed in Chapter 4, similar to the observation reported in [60, 67], a sample can only be used for a single set of measurements of increasing compression. This implies that the results presented in this section were obtained by averaging the measurements from 10 different GDL samples of nominally identical GDL structure and thickness. High repeatability was achieved and the standard deviation from the mean was much less than the calculated measurement uncertainty described in Chapter 4.

5.2.2 Thickness

The thickness of the MPL may at first appear difficult to measure separately from the GDL substrate. Figure 5.7 shows the thickness of SolviCore GDL with and without a MPL for compression pressures up to 15 bar. A least squares fit is applied to the measured data and overlaid on the graph. Both data sets are nearly linear, suggesting that there is a constant rate of change for thickness with increasing compressive load. Further, the two sets of data are almost parallel, indicating that both GDL experience the same rate of change in thickness with increasing compression pressure. Since both GDL are based on the same carbon substrate (i.e. same thickness and structure), this indicates that the MPL does not change thickness for compression pressures up to 15 bar tested in this study. It is believed that the MPL is mechanically stronger due to its fine pore structure. MPL density is nearly 4 times larger than the GDL substrate, calculated in Table 5.5 from uncompressed thickness and volume measurements. The actual MPL thickness is computed in Table 5.5 from the average difference in thickness between GDL with and without MPL over the range of compression pressures tested.

Microporous Layer	
Density of MPL to Substrate [-]	3.8
Thickness, L [μm]	55 ± 2
Thermal Conductivity, k [W/m°K]	0.30 ± 0.03

Table 5.5: Experimentally measured properties of SolviCore microporous layer.

The significance of the MPL maintaining a constant thickness under compression is threefold. First, unlike the GDL substrate porosity that is a function of compressed thickness, the porosity of the MPL remains almost constant. Likewise, it is expected that the effective heat and mass transport properties, which would otherwise vary as a function of compressed thickness, will remain the same for the MPL. Second, experimentally determined heat and mass transport properties are valid over all compression pressures (up to 15*bar* tested). This simplifies the collection of experimental data. Finally, with

73
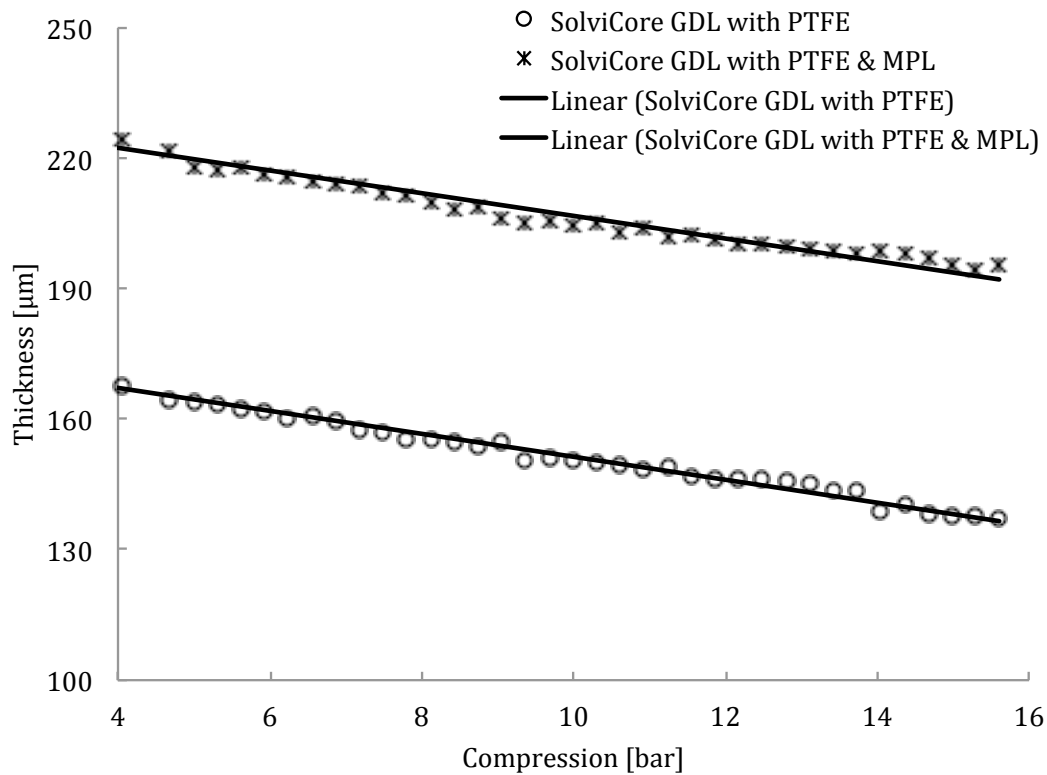
Figure 5.7: Through-plane thickness as a function of compression pressure for SolviCore gas diffusion layer at $80\,^{\circ}\text{C}$.

the knowledge that the MPL does not change thickness appreciably under compression, a computational model of the MPL can be simplified by specifying a single set of effective thermal, electrical, and diffusive properties that are independent of compression pressure. This is particularly important as the compressive force on the MPL varies significantly between regions compressed by the flow channel land and those that are not, in a practical cell environment [100].

Figure 5.8 shows a cross-sectional view of a SolviCore GDL with MPL. The MPL is clearly visible in the top half of the image characterized by a much lower porosity than the substrate, and a highly variable thickness. Although the MPL layer does not appear

uniform in thickness, the repeatability of thickness measurements in Figure 5.7 suggests that the variability exists only at a micrometer length scale. At the macroscale level, thickness appears to be relatively uniform.
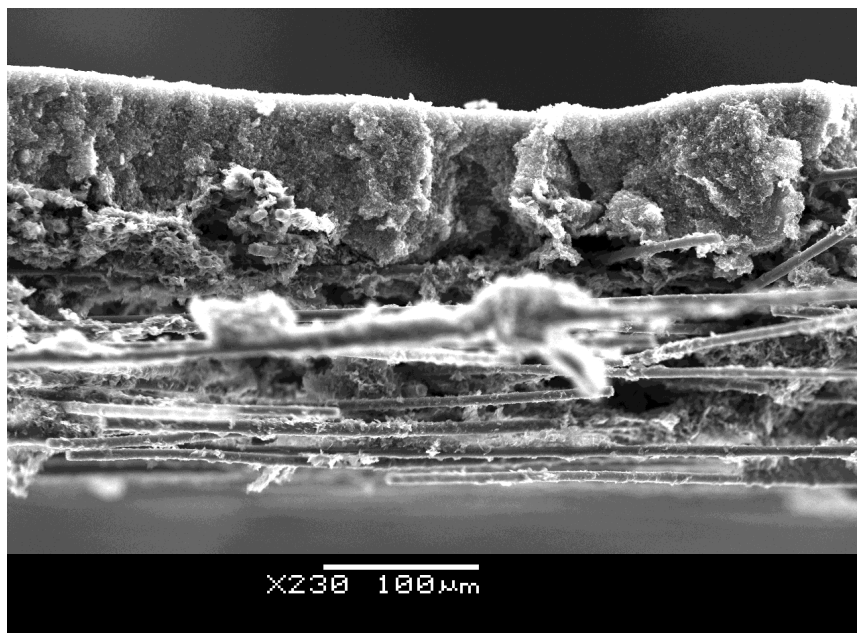
Figure 5.8: Cross-sectional view of SolviCore gas diffusion layer with microporous layer using a Scanning Electron Microscope at 230x magnification.

5.2.3 Thermal Conductivity

The through-plane effective thermal conductivity of the GDL with and without a MPL is investigated as a function of compression pressure, and the results are shown in Figure 5.9. Measurements taken at compression pressures below 4 bar were excluded due to increased uncertainties in the measured results, as mentioned earlier. Burheim *et al.* [64] made similar measurements on SolviCore GDL containing MPL. These results are included in Figure 5.9 and show general agreement within the respective margins of uncertainty. While the effective thermal conductivity for both GDL tested is similar below 6 bar of pressure, above this compression pressure the GDL containing MPL had a lower effective thermal

conductivity than the GDL without MPL. This indicates that the MPL has a lower effective thermal conductivity than the GDL substrate. Further investigation shows that the effective thermal conductivity of the MPL remains relatively constant for the range of the compression pressures tested, as shown in Figure 5.10. The effective thermal conductivity of the MPL layer is determined and given in Table 5.5 as an average for all compression pressures tested. The apparent stabilization of effective thermal conductivity at high compression pressures for the GDL containing MPL can be explained by the low effective thermal conductivity of the MPL. At high compression pressures the MPL dominates the resistance network portrayed in Figure 4.10.
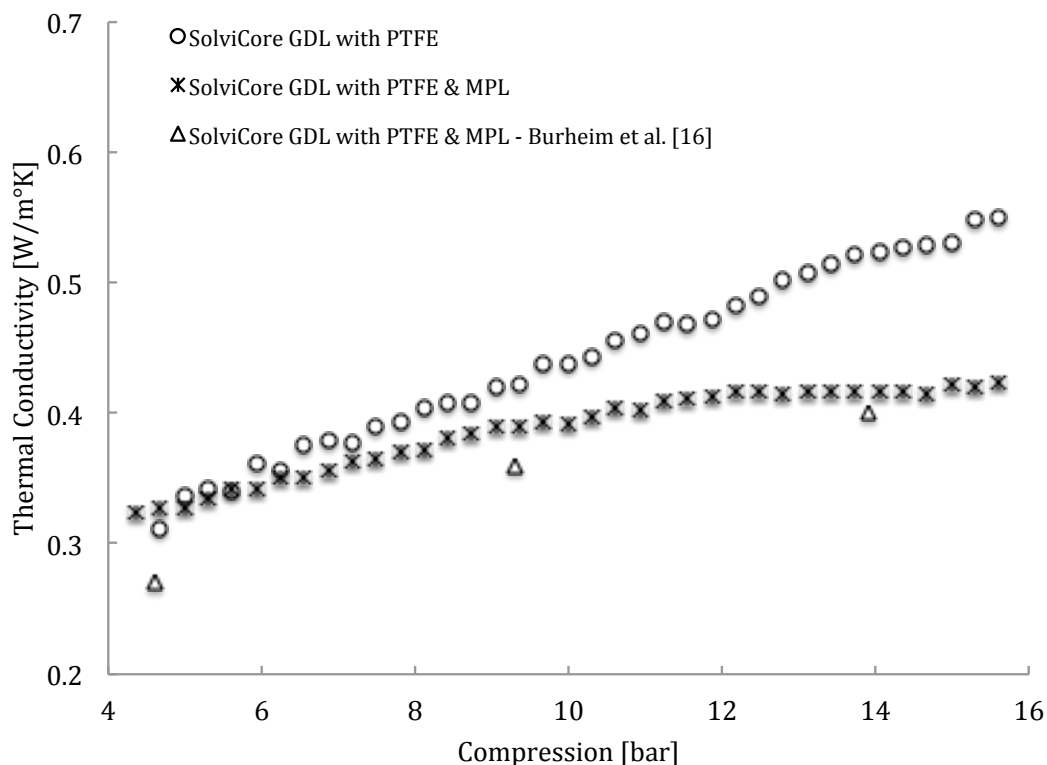
Figure 5.9: Effective thermal conductivity as a function of compression pressure for Solvi-Core gas diffusion layer at 80 °C.

Despite the high density of the MPL (Table 5.5), the relatively low effective thermal

76
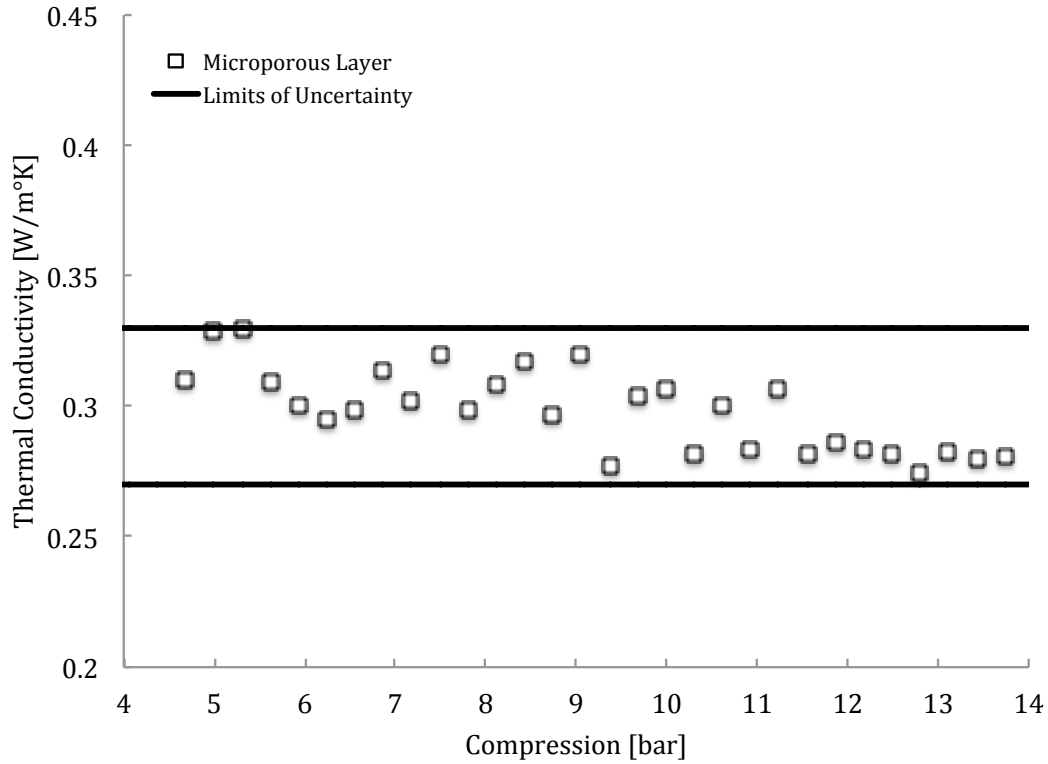
Figure 5.10: Effective thermal conductivity of the microporous layer as a function of compression pressure for SolviCore gas diffusion layer at 80 °C.

conductivity is likely due to the high PTFE content 30 %-wt. that is used as a binder, and the large surface area of the fine black carbon powder. The ability of the PTFE to coat a larger surface area compared to that of the GDL fibres, which have a comparably smaller surface area, might increase the influence of PTFE in the thermal resistance network.

The MPL restricts heat transfer at high compression pressures, yet has a negligible effect at low pressures when the porosity of the GDL substrate is higher. Nitta *et al.* [63] observed that the GDL remained at the uncompressed thickness under the flow channel, regardless of channel width. In these regions, the MPL has a effective thermal conductivity at parity with the GDL substrate.

5.2.4 Thermal Contact Resistance

The thermal contact resistance is predictably lower for the SolviCore sample containing a MPL as shown in Figure 5.11. One of the roles of the MPL is to improve surface contact with the catalyst layer; it is no surprise that a similar effect is observed with the smooth surface of the iron fluxmeters. The considerably smaller pores of the MPL, visible in Figure 5.8, compared with that of the GDL substrate results in a greater contact surface area with the fluxmeters. The GDL containing a MPL had a thermal contact resistance that is about 50% lower than the GDL without the MPL, also shown in Figure 5.11. With one contact face of the GDL containing MPL identical to that of the GDL without MPL, the MPL contact face is solely responsible for the reduction in contact resistance. The contact resistance of the MPL with the fluxmeters is practically negligible. This is an important observation considering that the contact resistance of the GDL without MPL accounts for approximately 40% of the overall thermal resistance in the samples that were tested. Optimally, the overall thermal resistance of the GDL could be reduced by 20% with the application of a MPL to one face of the GDL substrate.

It is expected that the contact resistance with fuel cell materials such as the bipolar plate and the catalyst layer will differ from that observed values with the iron fluxmeters, with a large dependence on surface roughness. Although quantitative data should not be used directly, the trends as a function of compression pressure should remain consistent with these findings.

5.2.5 Cyclic Effects of Compression

Thermal resistance of the GDL as a function of thickness is shown in Figure 5.12. The GDL, comprising of randomly overlapping carbon fibres, becomes thinner with increasing compression as the fibres are pressed into each other and porosity is reduced. A reduction in thickness corresponds to a reduction in thermal resistance because the fibre-to-fibre contact resistance is reduced. This reaches an asymptotic minimum at the point where the fibre-to-fibre contact resistance becomes negligible, and thermal resistance is dominated by the thermal conductivity of the bulk constituents; namely carbon and PTFE.
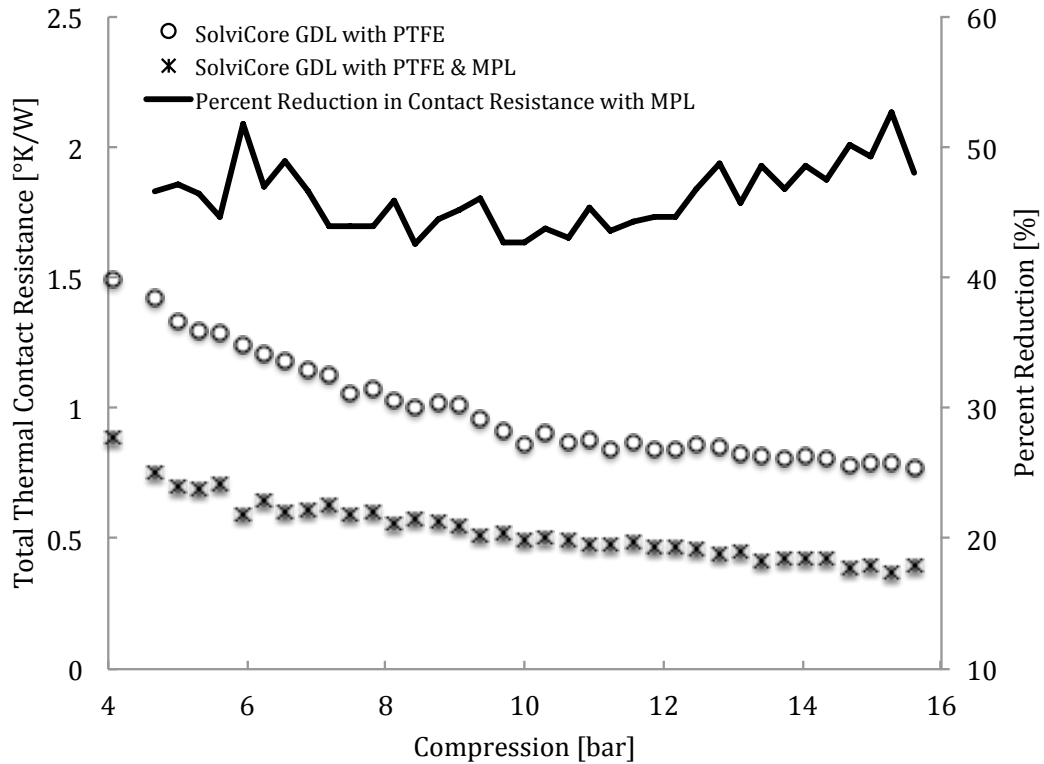
Figure 5.11: Thermal contact resistance as a function of compression pressure for SolviCore gas diffusion layer at 80 °C.

Expressing the thermal resistance of a GDL as a function of thickness, as it is shown in Figure 5.12, is especially important for the life cycle of a fuel cell. After all, an assembled fuel cell stack maintains the GDL at a specific thickness based on the thickness of the sealing gaskets and spacers. During the normal operation of the cell, the GDL will experience small thickness changes due to hygro-thermal stresses, which will be cyclic in nature [67]. Khandelwal and Mench [60] first noticed a hysteresis in thermal contact resistance when a GDL was compressed and then uncompressed. Later, Sadeghi *et al.* [67] investigated the hysteresis effect as a function of compression pressure and showed that thermal contact resistance decreased with repeated cycles. Similarly, Radhakrishnan and Haridoss [101, 102] demonstrated irreversible effects for various GDL properties as a result

79
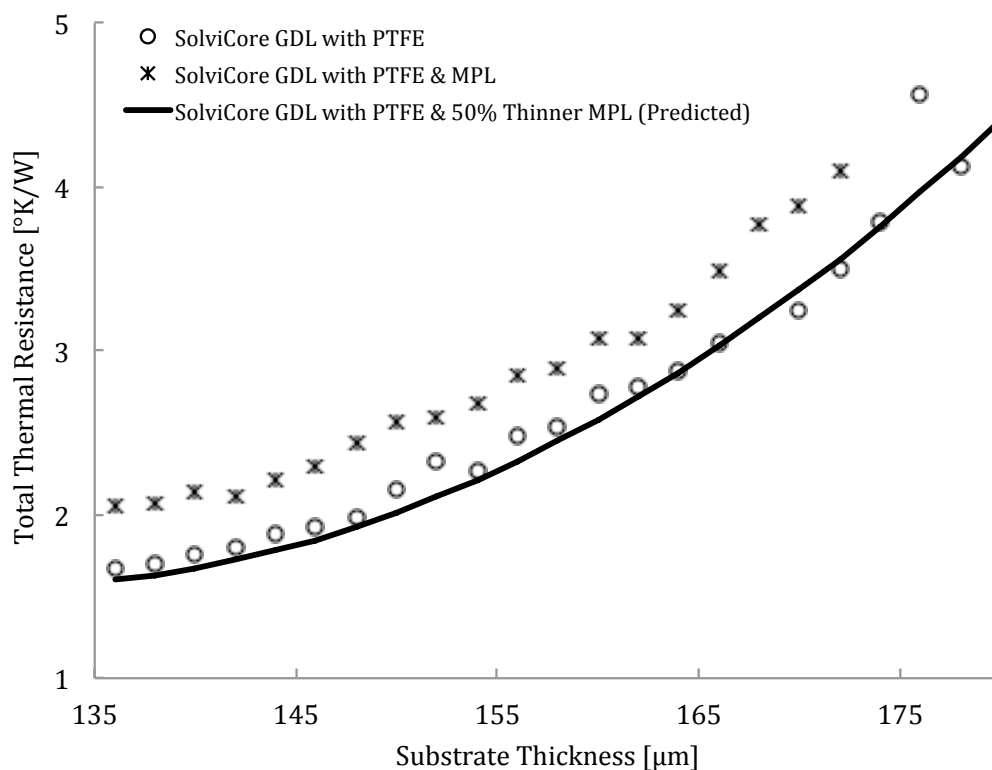
Figure 5.12: Total thermal resistance as a function of substrate thickness for SolviCore gas diffusion layer at 80 °C.

of cyclic compression. These results are significant for PEM fuel cells since cyclic loading on the GDL structure persists throughout the lifetime of the cell.

On the other hand, these observations at first might suggest that the thermal properties of a GDL degrade over the life of an operating fuel cell. However, when the total thermal resistance is expressed in terms of GDL thickness, no hysteresis effect is observed. Figure 5.13 shows the total thermal resistance, measured at 4.6, 9.3, and 13.9bar, for a single sample subjected to 3 repeated compressive loadings as a function of GDL thickness. The trend line passing through the data is a high-order polynomial curve fit of all SolviCore GDL with PTFE samples tested in this study. It is seen that with each successive loading and unloading cycle, the measured thermal resistance maintains the same relationship with

thickness, even though each subsequent loading-unloading cycle makes the GDL slightly thinner. Therefore, cyclic compressive loading encountered in an operating fuel cell might not affect the thermal properties of a GDL since the GDL thickness is maintained constant in the cell or stack assembly in practice via techniques discussed earlier. Similarly, repeated disassembly and reassembly of a fuel cell to a specific GDL thickness ensures repeatable GDL performance, and this is the routine approach practiced in our PEM fuel cell performance and durability tests.

Figure 5.13: Thermal resistance measurements for SolviCore gas diffusion layer over repeated compressive loading cycles at 80 °C.

5.2.6 Thermal Considerations for the Design of an MPL

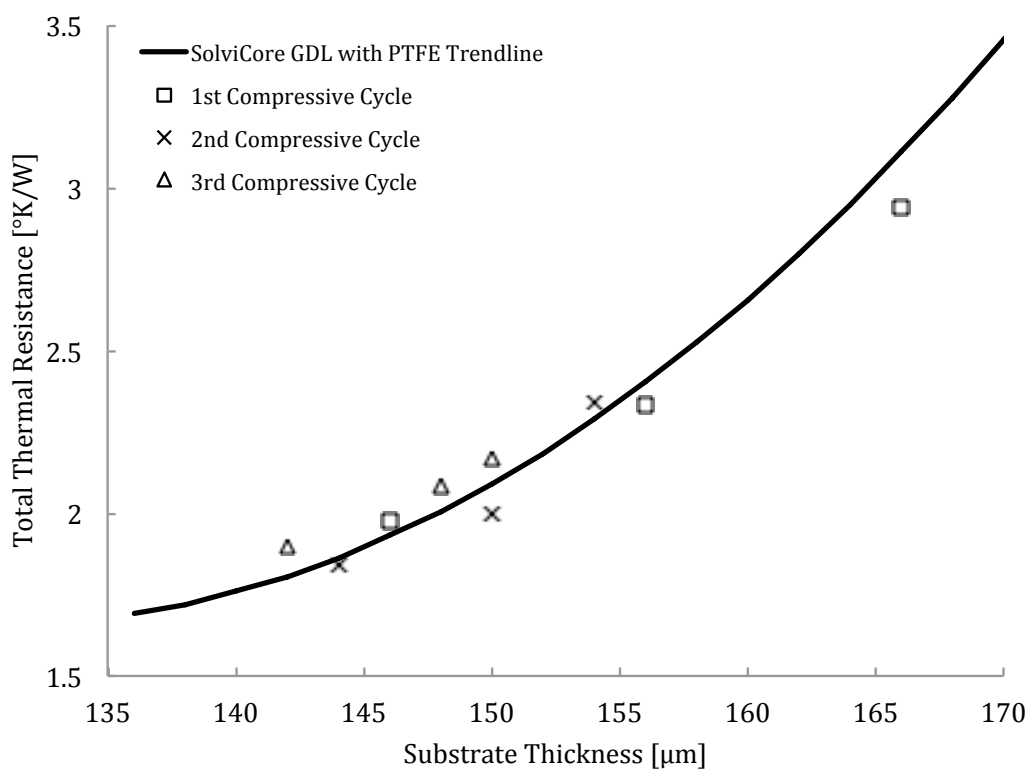The MPL has been shown to improve cell performance even though many of the mechanisms by which it does so are still under debate. Of these mechanisms, this study demonstrates that improving heat transfer is not one of them. In Figure 5.12, the overall thermal resistance, the sum of the through-plane resistance and surface contact resistance, is presented as a function of GDL substrate thickness for both GDL with and without a MPL. The GDL containing the MPL has a higher overall thermal resistance for a given GDL substrate thickness in spite of the fact that the MPL reduces the surface contact resistance substantially as discussed earlier. This also implies that the reduction in the surface contact resistance for the results shown in the figure is not sufficient to offset the increase in the thermal resistance for the presence of MPL due to the low effective thermal conductivity of the MPL. In order for the MPL to have a negligible effect on the overall thermal resistance, the reduction in the surface contact resistance must balance the increase in the thermal resistance of the MPL itself, and in Figure 5.12 that means both the curves for the GDL with and without the MPL should overlap. This could be achieved a number of ways in the design of a new MPL. For example, one approach is to reduce the thickness of the MPL by 50% in order to lower the effective thermal resistance of the MPL. The solid line shown in Figure 5.12 is the predicted thermal resistance of a GDL containing an MPL that is 50% thinner, and the prediction is based on the measured effective thermal conductivity of the MPL given earlier. Another approach could consider reducing the PTFE content because of the low thermal conductivity of the material. However, this could bring complexities for the actual PEM fuel cell operation since changing the PTFE content could affect the water transport abilities of the layers. A further approach might consider devising a method of PTFE coating such that PTFE is deposited into the pores of the MPL without interfering in the heat transfer between particles of carbon black. This would only be possible by applying the PTFE to the MPL after it is formed. At which point, achieving penetration of PTFE into the pores may prove difficult.

Chapter 6

Conclusion

6.1   Summary

In this thesis, the closed tube method, commonly referred to as the Loschmidt cell, and the steady-state guarded heat flow method were modified to measure the effective diffusion coefficient and the effective thermal conductivity of sub-micrometer thick samples to a high degree of accuracy. Improvements over previous experimental designs were achieved by identifying parameters sensitive to measurement error. A resistance ratio was identified as an important parameter that affected uncertainty and stacking multiple samples during measurement allowed this parameter to be controlled.

The effective diffusion coefficient was measured for Toray and SolviCore gas diffusion layers (GDL) and the effect of thickness and microstructure was assessed. Diffusibility varied with thickness for Toray GDL, with a difference of 8% between the samples tested. This breaks the standing assumption that transport coefficients are the same at different thicknesses. The SolviCore GDL had a 20% greater diffusibility than Toray GDL, which was attributed to the substantially larger pores of the SolviCore GDL. Experimental diffusibility results in published literature covering a variety of measurement techniques were presented together as a function of porosity. A modified correlation that relates diffusibility to porosity for carbon paper GDL with less than 10%-wt. PTFE was proposed that

takes into account all of this experimental data. The correlation should prove useful for the estimation of diffusion coefficients in fuel cell models when specific experimental data is not available.

The through-plane effective thermal conductivity and surface contact resistance of a SolviCore Type A microporous layer (MPL) was assessed. In-situ thickness measurements of the gas diffusion layer (GDL) with and without a microporous layer (MPL) revealed that the MPL thickness remained constant for up to $15bar$ of pressure. The significance of this behaviour is that, unlike the GDL, transport properties remain independent of the inhomogeneous compression by the bipolar plates in practical cell and stack assembly. Thermal contact resistance of the MPL with the iron clamping surface was found to be negligible, owing to the high surface contact area. Contact resistance accounted for 40% of the overall thermal resistance of the GDL without MPL, suggesting that heat transfer through the GDL could be significantly improved with the application of a MPL to one face of the GDL. The effective thermal conductivity of the MPL remained constant at $0.30W/m^\circ K$ for compression pressures up to $15bar$ tested in this study. The effective thermal conductivity of the GDL substrate varied from 0.30 to $0.56W/m^\circ K$ as compression was increased from 4 to $15bar$. As a result, GDL containing the MPL had a lower effective thermal conductivity at high compression than the GDL without the MPL. The MPL has the potential to improve heat transfer through the gas diffusion layer by significantly lowering the thermal contact resistance. However, the effective thermal conductivity of the MPL is lower than the GDL substrate at elevated compression pressures. For the MPL to have a positive effect on heat transfer through the GDL, the benefit of reduced contact resistance must be balanced with the drawback of lower effective thermal conductivity. This may be accomplished by controlling the MPL thickness or amount of PTFE.

6.2   Recommendations

In recent years, reduction in catalyst layer platinum loading to below $0.4mg/cm^2$ has placed greater importance on the heat and mass transport processes within the catalyst layer for achieving high current densities. The greatest contribution of this thesis is the

development of experimental methods that are capable of measuring the heat and mass transport properties of increasingly thin porous materials. This is particularly useful for catalyst layer development, where the thickness can be $10\mu m$ or less. Future work in this field of research should include,

1. Effective thermal conductivity and gas diffusivity measurements of the catalyst layer over a range of operating conditions.

   In addition, there are a number of operating conditions that the current experimental equipment could be modified to measure. Specifically,

2. Humidification of the gas feeds to the Loschmidt cell to enable the effect of relative humidity on the effective diffusion coefficient to be determined. Perfluorinated polymer electrolytes such as Nafion, used in the catalyst layer to conduct protons, swells in the presence of water.

3. The ability to compress a porous sample during measurement within the Loschmidt cell would provide experimental data that is representative of the compression force exerted by the bipolar plates in an operating fuel cell.

4. Increasing the diameter of both the Loschmidt apparatus gas chambers and the thermal conductivity apparatus fluxmeters would improve the ratio of cross sectional area to surface area. For the Loschmidt cell, this would minimize the impact that leaks and mechanical connections, e.g. the sliding gate, valves, gaskets, have on the results. For the thermal conductivity apparatus, this would reduce the impact of radial heat loss on axial heat flow; the largest source of measurement error.

   Finally, it is often difficult to compare the results gathered from two different experimental apparatuses due to the high measurement uncertainty in much of PEMFC literature. Therefore,

5. The measurement of a wide range of GDLs, MPLs, and CLs on the same measurement apparatus would be useful for making direct comparisons between samples from different manufacturers and operating conditions.

References

[1] Pfrang A. Fuel cell testing Degradation of fuel cells and its impact on fuel cell applications. *GIT Laboratory Journal Europe*. 2009;13:42–44.

[2] Baker R, Zhang J. Proton exchange membrane or polymer electrolyte membrane (PEM) fuel cells. 2011.
URL `http://electrochem.cwru.edu/encycl/art-f04-fuel-cells-pem.htm`

[3] Yovanovich M. *Advanced Heat Conduction*. University of Waterloo: In preparation. 1993.

[4] Bahrami M, Culham J, Yovanovich M, Schneider G. Thermal Contact Resistance of Nonconforming Rough Surfaces, Part 2 Thermal Model. *Journal of Thermophysics and Heat Transfer*. 2004;18:218–227.

[5] Daimler Ford GM/Opel Honda Hyundai/KIA Renault/Nissan Toyota. Letter of Understanding on the Development and Market Introduction of Fuel Cell Vehicles. 2009.
URL `http://www.hydrogenlink.net/download/LoU-fuelcell-cars.pdf`

[6] Daimler AG. Mercedes-Benz F-CELL World Drive: Around the world in 125 days. 2011.
URL `http://media.daimler.com/dcmedia/`

[7] American Honda Motor Corporation. Honda FCX Clarity. 2012.
URL `http://automobiles.honda.com/fcx-clarity/`

[8] Park Y, Caton J. Monitoring an electrode flooding through the back pressure in a proton exchange membrane (PEM) fuel cell. *International Journal of Green Energy*. 2008;5:347–359.

[9] Jiao K, Li X. Water transport in polymer electrolyte membrane fuel cells. *Progress in Energy and Combustion Science*. 2011;37:221–291.

[10] Zhang J, Li H, Shi Z, Zhang J. Effects of hardware design and operation conditions on PEM fuel cell water flooding. *International Journal of Green Energy*. 2010;7:461–474.

[11] Qi Z, Kaufman A. Improvement of water management by a microporous sublayer for pem fuel cells. *Journal of Power Sources*. 2002;109:38–46.

[12] Li X. *Principles of Fuel Cells*. New York: Taylor and Francis. 2006.

[13] Marrero T, Mason E. Gaseous Diffusion Coefficients. *Physical and Chemical Reference Data*. 1972;1:3–118.

[14] Mukherjee P, Wang C. Polymer electrolyte fuel cell modeling A a pore-scale perspective. *Progress in Green Energy*. 2011;1.

[15] Mathias MF, Roth J, Fleming J, Lehnert W. *Diffusion media materials and characterisation*. John Wiley and Sons Ltd. 2010;.

[16] Wang Y, Wang CY, Chen K. Elucidating differences between carbon paper and carbon cloth in polymer electrolyte fuel cells. *Electrochimica Acta*. 2007;52:3965 – 3975.

[17] Martenez-Rodreguez M, Tong C, Shimpalee S, Van Zee J. Characterization of microporous layer in carbon paper GDL for PEM fuel cell. *The Electrochemical Society*. 2010;33:1133–1141.

[18] Whitaker S. *The Method of Volume Averaging*. Theory and Applications of Transport in Porous Media. Kluwer Academic. 1999.

[19] Choy T. *Effective Medium Theory: Principles and Applications.* International Series of Monographs on Physics. Clarendon Press. 1999.

[20] Vielstich W, Lamm A, Gasteiger H. *Handbook of Fuel Cells - Fundamentals, Technology and Applications.* New York: John Wiley and Sons. 2003.

[21] Ho C, Webb S. *Gas transport in porous media.* Dordrecht, Netherlands: Springer. 2006.

[22] Marrero T, Mason E. Temperature Dependence of Gaseous Diffusion Coefficients. *Chem Eng Commun.* 1980;7:159–168.

[23] Reid R, Prausnitz J, Poling B. *The properties of gases and liquids.* McGraw-Hill. 1987.

[24] Cunningham R, Williams R. *Diffusion in gases and porous media.* Plenum Press. 1980.

[25] Thorstenson D, Pollock D. Gas Transport in Unsaturated Zones: Multicomponent Systems and the Adequacy of Fick's Laws. *Water Resourc Res.* 1989;25:477–507.

[26] Yovanovich M. *Conduction and Thermal Contact Resistances (Conductances),* chap. 3. McGraw-Hill. 1998;.

[27] Incropera F, DeWitt D. *Fundamentals of heat and mass transfer.* John Wiley. 2007.

[28] Das P, Li X, Liu Z. Effective transport coefficients in PEM fuel cell catalyst and gas diffusion layers: Beyond Bruggeman approximation. *Applied Energy.* 2010;87:2785–2796.

[29] Hashin Z, Shtrikman S. A Variational Approach to the Theory of the Effective Magnetic Permeability of Multiphase Materials. *Journal of Applied Physics.* 1962; 33(10):3125–3131.

[30] Zamel N, Li X, Shen J. Correlation of the Effective Gas Diffusion Coefficient in Carbon Paper Diffusion Media. *Energy Fuels.* 2009;23:6070–6078.

[31] Zamel N, Li X, Shen J, Becker J, Wiegmann A. Estimating effective thermal conductivity in carbon paper diffusion media. *Chemical Engineering Science*. 2010; 65:3994–4006.

[32] Bear J. *Dynamics of Fluids in Porous Media*. New York: Dover Publications. 1972.

[33] Bruggeman D. Calculation of various physics constants in heterogenous substances: Dielectricity constants and conductivity of mixed bodies from isotropic substances. *Annalen der Physik*. 1935;24:636–664.

[34] Tomadakis M, Sotirchos V. Ordinary and Transition Regime Diffusion in Random Fiber Structures. *AIChE Journal*. 1993;39:397–412.

[35] Tomadakis M, Robertson T. Viscous Permeability of Random Fiber Structures: Comparison of Electrical and Diffusional Estimates with Experimental and Analytical Results. *Journal of Composite Materials*. 2005;39:163–188.

[36] Kramer D, Freunberger S, Flückiger R, Schneider I, Wokaun A, Büchi F, Scherer G. Electrochemical diffusimetry of fuel cell gas diffusion layers. *Journal of Electroanalytical Chemistry*. 2008;612:63–77.

[37] Zamel N, Astrath N, Li X, Shen J, Zhou J, Astrath F, Wang H, Liu Z. Experimental measurements of effective diffusion coefficient of oxygen-nitrogen mixture in PEM fuel cell diffusion media. *Chemical Engineering Science*. 2010;65:931–937.

[38] Martínez M, Shimpalee S, Van Zee J. Measurement of MacMullin Numbers for PEMFC Gas-Diffusion Media. *Journal of The Electrochemical Society*. 2009;156:B80–B85.

[39] LaManna J, Kandlikar S. Determination of effective water vapor diffusion coefficient in pemfc gas diffusion layers. *International Journal of Hydrogen Energy*. 2011; 36:5021–5029.

[40] Baker D, Wieser C, Neyerlin K, Murphy M. The Use of Limiting Current to Determine Transport Resistance in PEM Fuel Cells. *ECS Transactions*. 2006;3:989–999.

[41] Baker D, Caulk D, Neyerlin K, Murphy M. Measurement of Oxygen Transport Resistance in PEM Fuel Cells by Limiting Current Methods. *Journal of The Electrochemical Society*. 2009;156:B991–B1003.

[42] Beuscher U. Experimental Method to Determine the Mass Transport Resistance of a Polymer Electrolyte Fuel Cell. *Journal of the Electrochemical Society*. 2006; 153:A1788–A1793.

[43] Stumper J, Haas H, Granados A. In Situ Determination of MEA Resistance and Electrode Diffusivity of a Fuel Cell. *Journal of the Electrochemical Society*. 2005; 152:A837–A844.

[44] Flückiger R, Freunberger S, Kramer D, Wokaun A, Scherer F GG Büchi. Anisotropic, effective diffusivity of porous gas diffusion layer materials for PEFC. *Electrochimica Acta*. 2008;54:551–559.

[45] Martínez M, Tong C, Shimpalee S, Van Zee J. Characterization of Microporous Layer in Carbon Paper GDL for PEM Fuel Cell. *ECS Transactions*. 2010;33:1133–1141.

[46] Chan C, Zamel N, Li X, Shen J. Experimental measurement of effective diffusion coefficient of gas diffusion layer/microporous layer in PEM fuel cells. *Electrochimica Acta*. 2012;65:13 – 21.

[47] Shen J, Zhou J, Astrath N, Navessin T, Liu Z, Lei C, Rohling J, Bessarabov D, Knights S, Ye S. Measurement of effective gas diffusion coefcients of catalyst layers of PEM fuel cells with a Loschmidt diffusion cell. *Journal of Power Sources*. 2011; 196:674–678.

[48] Baschuk J, Li X. A general formulation for a mathematical PEM fuel cell model. *Journal of Power Sources*. 2005;142(1-2):134 – 153.

[49] Maggio G, Recupero V, Mantegazza C. Modelling of temperature distribution in a solid polymer electrolyte fuel cell stack. *Journal of Power Sources*. 1996;62(2):167 – 174.

[50] Wohr M, Bolwin K, Schnurnberger W, Fischer M, Neubrand W, Eigenberger G. Dynamic modelling and simulation of a polymer membrane fuel cell including mass transport limitation. *International Journal of Hydrogen Energy.* 1998;23(3):213 – 218.

[51] Shan Y, Choe SY. A high dynamic PEM fuel cell model with temperature effects. *Journal of Power Sources.* 2005;145(1):30 – 39.

[52] Wu H, Berg P, Li X. Non-isothermal transient modeling of water transport in PEM fuel cells. *Journal of Power Sources.* 2007;165(1):232 – 243.

[53] Pharoah J, Karan K, Sun W. On effective transport coefficients in PEM fuel cell electrodes: Anisotropy of the porous transport layers. *Journal of Power Sources.* 2006;161(1):214 – 224.

[54] Sadeghi E, Bahrami M, Djilali N. Analytic determination of the effective thermal conductivity of PEM fuel cell gas diffusion layers. *Journal of Power Sources.* 2008; 179(1):200 – 208.

[55] Veyret D, Tsotridis G. Numerical determination of the effective thermal conductivity of fibrous materials. Application to proton exchange membrane fuel cell gas diffusion layers. *Journal of Power Sources.* 2010;195(5):1302 – 1307.

[56] Ramousse J, Didierjean S, Lottin O, Maillet D. Estimation of the effective thermal conductivity of carbon felts used as PEMFC gas diffusion layers. *International Journal of Thermal Sciences.* 2008;47:1–6.

[57] Burford D, Davis T, Mench M. In Situ temperature distribution measurements in an operating polymer electrolyte fuel cell. In: *Proceedings of the 2003 International Mechanical Engineering Congress and Exposition.* Washington, DC. 2003; .

[58] Vie P, Kjelstrup S. Thermal Conductivities from temperature profiles in the polymer electrolyte fuel cell. *Electrochimica Acta.* 2004;49:1069–1077.

[59] Ihonen J, Mikkola M, Lindbergh G. Flooding of gas diffusion backing in PEFCs. *Journal of the Electrochemical Society.* 2004;151:1152–1161.

91

[60] Khandelwal M, Mench M. Direct Measurement of through-plane thermal conductivity and contact resistance in fuel cell materials. *Journal of Power Sources*. 2006; 161:1106–1115.

[61] Zhou P, Wu C. Numerical study on the compression effect of gas diffusion layer on PEMFC performance. *Journal of Power Sources*. 2007;170:93–100.

[62] Hottinen T, Himanen O, Karvonen S, Nitta I. Inhomogeneous compression of PEMFC gas diffusion layer Part II. Modeling the effect. *Journal of Power Sources*. 2007;171:113–21.

[63] Nitta I, Himanen O, Mikkola M. Thermal Conductivity and contact resistance of compressed gas diffusion layer of PEM fuel cell. *Fuel Cells*. 2008;8:111–19.

[64] Burheim O, Vie P, Pharoah J, Kjelstrup S. Ex Situ measurements of through-plane thermal conductivities in a polymer electrolyte fuel cell. *Journal of Power Sources*. 2010;195:249–56.

[65] Karimi G, Li X, Teertstra P. Measurement of Throughplane effective thermal conductivity and contact resistance in PEM fuel cell diffusion media. *Electrochimica Acta*. 2010;55:161925.

[66] Sadeghi E, Djilali N, Bahrami M. Effective Thermal conductivity and thermal contact resistance of gas diffusion layers in proton exchange membrane fuel cells. Part 1: Effect of compressive load. *Journal of Power Sources*. 2011;196:246–254.

[67] Sadeghi E, Djilali N, Bahrami M. Effective Thermal conductivity and thermal contact resistance of gas diffusion layers in proton exchange membrane fuel cells. Part 2: Hysteresis effect under cyclic compressive load. *Journal of Power Sources*. 2010; 195:8104–09.

[68] Zamel N, Li X, Becker J, Wiegmann A. Effect of liquid water on transport properties of the gas diffusion layer of polymer electrolyte membrane fuel cells. *International Journal of Hydrogen Energy*. 2011;36:5466–5478.

[69] Burheim O, Pharoah J, Lampert H, Vie P, Kjelstrup S. Through-plane thermal conductivity of PEMFC porous transport layers. *Journal of Fuel Cell Science and Technology.* 2011;8:021013–24.

[70] Zamel N, Litovsky E, Li X, Kleiman J. Measurement of the Through-plane thermal conductivity of carbon paper diffusion media for the temperature range from -50 to +120C. *International Journal of Hydrogen Energy.* 2011;36:12618–25.

[71] Volfkovich Y, Bagotzky V. The method of standard porosimetry: 1. Principles and possibilities. *Journal of Power Sources.* 1994;48(3):327 – 338.

[72] Volfkovich Y, Bagotzky V. The method of standard porosimetry 2. Investigation of the formation of porous structures. *Journal of Power Sources.* 1994;48(3):339 – 348.

[73] Volfkovich Y, Bagotzky V, Sosenkin V, Blinov I. The standard contact porosimetry. *Colloids and Surfaces A: Physicochemical and Engineering Aspects.* 2001;187(0):349 – 365.

[74] Drake LC. Pore-Size Distribution in Porous Materials. *Industrial and Engineering Chemistry.* 1949;41(4):780–785.

[75] Dubinin M, Plavnik G. Microporous structures of carbonaceous adsorbents. *Carbon.* 1968;6(2):183 – 192.

[76] Gregg SJ, Sing KSW, Salzberg HW. Adsorption Surface Area and Porosity. *Journal of The Electrochemical Society.* 1967;114(11):279C–279C.

[77] Youngquist GR. Symposium on Flow Through Porous Media - Diffusion and Flow of Gases in Porous Solids. *Industrial and Engineering Chemistry.* 1970;62(8):52–63.

[78] ASTM International. Standard Test Method for Oxygen Transmission Rate Through Dry Packages Using a Coulometric Sensor. *Tech. Rep. F1307*, ASTM International, West Conshohocken, PA. 2007.

[79] ASTM International. Standard Test Method for Oxygen Gas Transmission Rate Through Plastic Film and Sheeting Using a Coulometric Sensor. *Tech. Rep. D3985*, ASTM International, West Conshohocken, PA. 2010.

[80] Loschmidt J. Experimental-Untersuchungen uber die Diffusion vonGasen ohne porose Scheidewande. *Wiener Berichte.* 1870;61:367–380.

[81] Rohling J, Shen J, Wang C, Zhou J, Gu C. Determination of binary diffusion coefficients of gases using photothermal deflection technique. *Applied Physics B: Lasers and Optics.* 2007;87:355–362.

[82] Rohling JH, Shen J, Wang C, Zhou J, Gu CE. Photothermal deflection measurement of effective gas diffusion coefficient of a porous medium. *The European Physical Journal - Special Topics.* 2008;153:111–113.

[83] Astrath N, Shen J, Song D, Rohling J, Astrath F, Zhou J, Navessin T, Liu Z, Gu C, Zhao X. The Effect of Relative Humidity on Binary Gas Diffusion. *The Journal of Physical Chemistry.* 2009;113:8369–8374.

[84] Astrath NGC, Shen J, Astrath FBG, Zhou J, Huang C, Yuan XZ, Wang H, Navessin T, Liu ZS, Vlajnic G, Bessarabov D, Zhao X. Note: Determination of effective gas diffusion coefficients of stainless steel films with differently shaped holes using a Loschmidt diffusion cell. *Review of Scientific Instruments.* 2010;81(4):046104–046104–3.

[85] Dong L, Unsworth G, Li X. Errors and Uncertainty in Diffusion Measurements Through Thin Porous Media. *Preprint.* 2012;.

[86] Ocean Optics Inc. *NeoFox Installation and Operating Manual.* Dunedin, FL: Ocean Optics. 2010.

[87] Kautsky H. Quenching of luminescence by oxygen. *Trans Faraday Soc.* 1939;35:216–219.

[88] Baranski J, Bich E, Vogel E, Lehmann J. Determination of Binary Diffusion Coefficients of Gases Using Holographic Interferometry in a Loschmidt Cell. *International Journal of Thermophysics.* 2003;24:1207–1220.

[89] Crank J. *The Mathematics of Diffusion.* Oxford Science Publications. Clarendon Press. 1979.

94

[90] Moffat R. Describing the Uncertainties in Experimental Results. *Experimental Thermal and Fluid Science*. 1988;1:3–17.

[91] Tordai L. Errors in diffusion measurements by the Loschmidt method. *British Journal of Applied Physics*. 1950;1:329–332.

[92] ASTM International. Standard test method for thermal transmission properties of thermally conductive electrical insulation materials. *Tech. Rep. D5470*, ASTM International, West Conshohocken, PA. 2011.

[93] Culham J, Teertstra P, Savija I, Yovanovich M. Design, assembly and commissioning of a test apparatus for characterizing thermal interface materials. In: *8th Intersociety Conference on Thermal and Thermomechanical Phenomena in Electronic Systems*. San Diego, CA. 2002; .

[94] Lee M, Kim K, Hopkins R, Gawlik K. Thermal conductivity measurements of copper-coated metal hydrides for use in metal hydride hydrogen compression systems. *International Journal of Hydrogen Energy*. 2009;34:3185–3190.

[95] Toray Industries Inc. Carbon Paper Specifications. 2005.
URL `http://www.torayca.com/en/index.html`

[96] Fishman Z, Hinebaugh J, Bazylak A. Microscale Tomography Investigations of Heterogeneous Porosity Distributions of PEMFC GDLs. *Journal of The Electrochemical Society*. 2010;157:B1643–B1650.

[97] Fishman Z, Bazylak A. Heterogeneous Through-Plane Distributions of Tortuosity, Effective Diffusivity, and Permeability for PEMFC GDLs. *Journal of The Electrochemical Society*. 2011;158:B247–B252.

[98] Gao B, Steenhuis T, Zevi Y, Parlange J, Carter R, Trabold T. Visualization of unstable water flow in a fuel cell gas diffusion layer. *Journal of Power Sources*. 2009; 190:493–498.

[99] Maheshwari P, Mathur R, Dhami T. The influence of the pore size and its distribution in a carbon paper electrode on the performance of a PEM Fuel cell. *Electrochimica Acta.* 2008;54:655–659.

[100] Nitta I, Hottinen T, Himanen O, Mikkola M. Inhomogeneous compression of PEMFC gas diffusion layer Part I. Experimental. *Journal of Power Sources.* 2007;171:26–36.

[101] Radhakrishnan V, Haridoss P. Effect of cyclic compression on structure and properties of a gas diffusion layer used in PEM fuel cells. *International Journal of Hydrogen Energy.* 2010;35:11107–11118.

[102] Radhakrishnan V, Haridoss P. Effect of GDL compression on pressure drop and pressure distribution in PEMFC flow field. *International Journal of Hydrogen Energy.* 2011;36:14823–14828.